12-2017

Synthesis, Application and Protein Nanomaterial Interactions of Selected Nanofiber, Nanoparticle and Nanoarray

Yimei Wen
Clemson University

SYNTHESIS, APPLICATION ANDS PROTEIN NANOMATERIAL INTERACTIONS OF SELECTED NANOFIBER, NANOPARTICLE AND NANOARRAY

A Dissertation
Presented to
the Graduate School of
Clemson University

In Partial Fulfillment
of the Requirements for the Degree
Doctor of Philosophy
Chemistry

---

by
Yimei Wen
December 2017

Accepted by:
Dr. George Chumanov, Committee Chair
Dr. R. Kenneth Marcus
Dr. Jeffery N. Anker
Dr. William T. Pennington

ABSTRACT

Nanomaterials have been a hot research topic for past decades due to their unique optical, electronic, catalytic and mechanical properties. This dissertation aims to investigate selected aspects of nanomaterial synthesis, application and protein nanomaterial interactions. We target to improve nanomaterials synthesis, explore their novel applications and study their potential hazardous. Chapter 1 describes new hydrothermal synthesis of carbon nanofibers from cellulose nanocrystals. The described hydrothermal synthesis from cellulose is an environmentally friendly method that has commercial potential for inexpensive production of carbon nanofibers. Chapter 2 describes the application of poly(methyl methacrylate) (PMMA) stabilized 2D AgNP array for measuring changes of bulk refractive index and sensing of selected volatile organic compound (VOC). The PMMA stabilized 2D AgNP array gives linear response to bulk refractive index changes and can be re-used after rinsing with water. Responsive polymer films were spin-coated on PMMA stabilized 2D AgNP array to fabricate the nanocomposite films. These nanocomposite films exhibit sharp coherent plasmon coupling, spectra position of which is affected by the changes of local dielectric environment when interacting with VOC vapors. Chapter 3 describes studies related to the interaction of AgNP and AuNP with cytoskeleton protein (actin and tubulin), immune system protein (complementary component 3) and plasma protein (albumin and fibrinogen). The nanoparticle protein interaction is influenced by both nanoparticle and

protein sizes. The work presented here establishes basic knowledge related to nanomaterial synthesis and their advanced applications.

DEDICATION

This dissertation is dedicated to my aunt and my parents. Without their support and encouragement, I wouldn't be able to get to this stage of my life. Many things happened during my PhD years and my mood swing up and down, they always cheer my up no matter what. I'm very grateful to be their child. Even though we were poor, they never let me down due to money issues. We found happiness in making food together, in travelling together, in watching TV shows together, in exercising together. Without the love from my parents and my aunt, I wouldn't survive my PhD. I wish in a short time I will be able to take my parents and my aunt to a Hawaii or Alaska cruise trip. We will have fun and great memory will stay with us for years.

This dissertation is also dedicated to the friends I have made here at Clemson University who have companied me for years. I like to travel with my friends. We have visited the Great Smoky Mountains, Puerto Rico, Charleston, Montreal in Canada, New York, Boston, Chicago, Universal Studios in Orlando, Florida Keys, San Diego, San Francisco, Los Angeles and Seattle. I enjoyed every moment spent with my friends, the zoos, the museums, the concerts, the theme parks, the shopping centers we have visited together, the food we have tried together, the movies we have watched together are the sparkle stars in my boring daily life. I will never forget those good times. They are the best gifts I have ever had during my life.

ACKNOWLEDGMENTS

First and foremost, I would like to thank my advisor, Dr. George Chumanov for teaching me all the knowledge in science. Also thanks for taking me when my pervious advisor moved to Australia. Dr Chumanov has a passion in science; I see this each time when we discuss about research. He taught me how to design experiments, how to use what I learned in classes to solve the issues I encountered in research, how to correlate the results with conclusion. Without Dr Chumanov's help, I wouldn't be able to finish my PhD. He not only taught me chemistry, but also acted as a mentor in my life. His way of living is going to be a model for me for the rest of my life.

Second, I am grateful to Dr Ke, Dr. Kolis, Dr Anker & Dr Luzinov research groups here at Clemson University for providing me opportunities with collaboration work. I was able to expand my skill into different research topics involving single crystal Raman spectroscopy, atomic force microscopy, electron microscopy, etc. It was my pleasure to collaborate with them and published the results on scientific journals.

Last but not least, I am also grateful to Dr Anker, Dr Marcus, and Dr Pennington, who are willing to serve as my committee members. Dr Anker taught me the in-depth understanding of quantitative analysis while I served as a teaching assistant in Analytical and Instrumental Labs. Dr Marcus showed his support to me whenever we attended same conferences. Dr Pennington encouraged me during symposium competitions. I would like to thanks all professors who have helped me in my PhD years.

TABLE OF CONTENTS

Page

Page

LIST OF TABLES

Page

LIST OF FIGURES

Page

Page

Page

CHAPTER ONE

Conversion of Cellulose Nanocrystals into Carbon Nanofibers

1.1 Introduction

Consumers, industry, and governments are increasingly asking for materials made from sustainable and renewable resources that are plentiful in nature and biodegradable. Natural cellulose based products like wood, cotton and rope have been used for thousands of years.[1] Cellulose is composed of cellulose nanofibers assemblies with 2-20 nm diameter and more than a few micrometers length with 65%-95% crystallinity.[2] The highly crystalline cellulose fibrils provide high strength for hemicellulose, lignin, and plant cell wall. Various approaches have been reported to derive cellulose fibrils from different sources.[2, 3] In controlled sulfuric acid hydrolysis, cellulose chains in less ordered or amorphous domains can be decomposed leaving the highly crystalline domain intact. These highly crystalline cellulose domains are in nanometer range width and 0.1-2 μm length, and are commonly called cellulose nanocrystals (CNC). Derived from the most abundant polymer in nature, CNC are among the most exciting cutting edge materials.[3] Researchers have reported their applications for reinforcing natural and synthetic polymers, paper coating, packaging science as well as antibacterial films, liquid crystals, biomedical implants and many others.[1] Effective methods for transforming cellulose into chemicals have been explored that include gasification, pyrolysis,

liquefaction and solidification.[4] In this chapter, we used a one-step hydrothermal conversion to synthesize 1-2 nm carbon nanofibers from CNC using a low cost, convenient and environmentally benign method. The detailed pyrolysis of cellulose was first studied in 1964 by M. M. Tang and R. Bacon revealing that the major pyrolytic degradation begins at about 240 ℃ and the aromatization takes place above 400 ℃. [5] The hydrothermal conversion of cellulose was performed in subcritical water to produce hydrochar that contained carbon nanoparticles by M. Sevilla and A. B. Fuertes. [6] The hydrochar was further used to generate graphitic nanostructures at 900 ℃ in the presence of nickel catalyst. [7] Laser pyrolysis was also employed to rapidly pyrolyze the cellulose hydrothermal char to produce hollow carbon nanospheres.[8] For the first time hydrothermal conversion was used for the synthesis of carbon nanofibers. Compared with traditional methods of synthesizing carbon nanofibers, subcritical water, the water above boiling point and below critical point (374^{o}C, 22.1MPa) is involved in our hydrothermal conversion. Subcritical water offers high pressure and high temperature with higher diffusivity than liquid phase, [9, 10] meanwhile providing sufficient density to dissolve materials but keeping low viscosity to facilitate mass transport.[11] It is viewed as a green, cheap and nontoxic reagent for converting biomass into valuable chemicals.[12] Hydrothermal conversion has been explored to synthesis multiwall carbon nanotubes from amorphous carbon.[13] The conditions for the formation of coal deposits involve low- or medium-temperature hydrothermal processes at moderate pressures, this work may explain the presence of carbon nanotubes and nanofibesrs in coals, carbonaceous rocks and natural graphite deposits. [14] The direct synthesis of 2 nm carbon nanofibers

can be exploited further to synthesize carbon nanotubes using cellulose by modifying hydrothermal conversion conditions. Ultimate goal of this research is to produce valuable and useful byproducts from cellulosic wastes from agriculture and food industry.[15]

1.2 Materials and Methods

1.2.1 Materials

Deionized water with nominal resistivity of 18 MΩ·cm was obtained from a Millipore Milli-Q water purification system. 29% ammonium hydroxide was purchased from BDH Chemicals, Inc. 27% hydrogen peroxide was purchased from Alfa Aesar. Whatman ashless filter aids were purchased from Sigma Aldrich.

1.2.2 Methods

Atomic force microscopy (AFM) was performed using an AIST-NT Smart SPM in non-contact mode with HQ:NSC14/AL BS cantilevers from Mikro-Masch. The samples were diluted then drop-casted on RCA cleaned silicon wafer. AFM image processing was carried out with AIST-NT SPM Control Software. Silicon wafer (MEMC Electronic Materials, St. Peters, Missouri, USA) was cut into pieces and cleaned with 5:1:1 (volume ratio) H_2O:NH_4OH:H_2O_2 at 70^oC for 10 minutes then cleaned with 5:1:1 (volume ratio) H_2O: HCl: H_2O_2 at 70^oC for 10 minutes followed by rinsing with copious water. The washed silicon wafers were stored in water before use to minimize the surface oxidization caused by air. [16] Samples were also drop cast on formvar coated copper grids cleaned with acetone and air plasma for one minute and imaged with transmission electron microscopy (TEM) Hitachi 9500 after staining with 10 mM uranyl acetate. An

Ar^+ laser (Innova 100, Coherent) was used to excite Raman spectra with 514.5 nm light. Raman spectra were measured using a spectrograph (SPEX, Triplemate 1877) interfaced to a thermoelectrically cooled CCD detector (Andor Technology, Model DU420A-BV) operating at -60 ℃. Raman samples were prepared by drop cast samples on cleaned silicon wafer. The laser power was between 20-25 mW at the samples with a total acquisition time of 10-20 minutes for each measurement. The scattered light was collected in a backscattering geometry, and the instrument was calibrated using an indene/chloroform mixture. All Raman spectra were measured and recorded using Andor Solis. Figures were plotted using Spectra-Solve (Amers Photonics Inc). Powder X-ray (PXRD) were obtained from a Rigaku Ultima IV diffractometer equipped with Cu Kα radiation (λ = 1.5406 Å). The powder diffraction patterns were collected in 0.02° increments over a 2θ range from 5° to 65° at a scan speed of 0.5°/min. PXRD samples were prepared by dropping samples on clean glass slides. Thermogravimetric analysis of CNC was measured using TA Instruments SDT-Q600 under nitrogen flow ramp 10 ℃/min from 20 ℃ to 100 ℃ (isothermal at 100 ℃ for 20 min) then ramp 5 ℃/min from 100 ℃ to 400 ℃ (isothermal at 400 ℃ for 20 min). Gas Chromotography Mass Spectroscopy was measured using Shimazu GC-MS 2010 SE. The chromatographic separation was performed with a SH-Rxi-5ms column. The oven temperature was programmed to flow ramp 20 ℃/min from 50 ℃ (isothermal at 50 ℃ for 3 min) to 330 ℃ (isothermal at 330 ℃ for 3 min). The analyzed mass-to-charge ratio (m/z) was set from 45 to 500. The content of each component is determined by Mass Spectroscopy.

1.2.3 Preparation of CNC

225 mL of 64% H_2SO_4 and 15.08 g of Whatman (Piscataway, NJ) cellulose filter aids (cotton powder) was stirred with a mixer and a Teflon stirrer in a water heating bath at 45 ℃ for 50 minutes. Then 225 mL of cold deionized water was added to quench the reaction. The solution was placed on ice bath for about 5-10 minutes before centrifuging at 10,000g for 10 minutes at 4 ℃. The centrifugation was repeated three times with approximately 30 mL of deionized water. The solution was re-dispersed in water after the third wash. A dialysis of the solution was performed with constant stirring till no change in pH was observed. All CNC solutions were stored in refrigerator in glass containers. Sonication was used to re-disperse CNC into water before further use. The CNC was prepared by our collaborator Dr. Kitchens and his student Mingzhe Jiang. [17]

1.2.4 Hydrothermal conversion of CNC

Hydrothermal conversion was carried out by adding 5 mL of 0.01 mg/L CNC into a 20 mL stainless steel pressure bomb with a Teflon® liner. The reactor was sealed and kept at 240^{o}C for 14 days. After finishing the reaction, top yellowish solution was saved as Sample A (heavy oil), blackish bottom slurry was kept as Sample B (solid residue). Sample B was diluted with water then Sample B started to separate into two layers after couple days. The top clear supernatant layer was named as Sample C.

1.3 Results and Discussion

The acid hydrolysis digested the amorphous cellulose domains leaving the highly crystalline cellulose domain intact. The resultant CNC had the shape of a squeezed

prolate spheroid shape with the average length of 107 ± 55 nm, width of 20 ± 6 nm and height of 9 ± 3 nm (Fig. 1.1 A&B). The CNC have many -OH groups on the surface after acid digestion. These -OH groups favor the formation of hydrogen bonding, causing the CNC to self-assemble into highly ordered structures. [18, 19] The hydrothermal conversion was repeated for different batches of CNC yielding the same results as shown in AFM images (Fig. 1.1 C & D). Flat ribbon-like structures consisting of individual fibers of about 2.5 nm in height were obtained after HTC of CNC. Carbon nanofibers (CNF) with the height as small as 1-2 nm as well as irregular shaped particles in the size range from ten nanometers to a few hundreds of nanometers were also observed. Some CNF appeared broken implying their rigidity (Fig. 1.1 E) whereas others showed flexibility by forming curved shapes (Fig. 1.1 F). The TEM images revealed the presence of three-dimensional entangled fiber bundles (Fig. 1.2 A&B) contrary to the characteristic ribbon structures and individual fibers observed by AFM on Si wafers (Fig. 1.1 C). It is important to point out that structures appearing as 'individual' fibers in TEM images (Fig. 1.2 A&B) are most likely fiber bundles because their apparent ~20 nm width is significantly larger than 2.5 nm height of individual fibers measured by AFM (Fig. 1.1 C). [20]

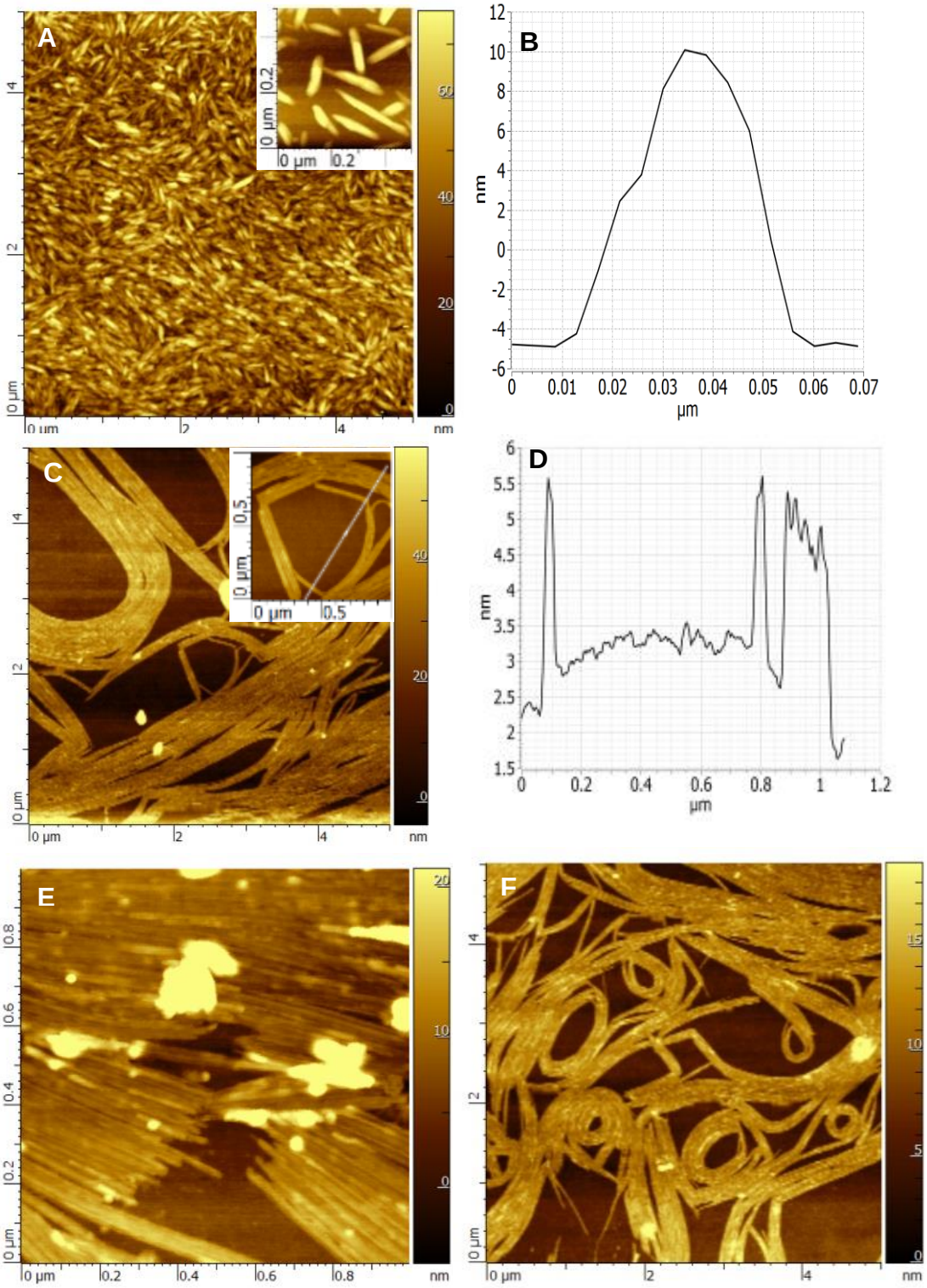

Figure. 1. 1 AFM images of (A) CNC, (B) Height profile of CNC from inset in Image A, (C)CNF, (D)Height profile of CNF from inset in Image C, (E) Rigid CNF, (F) Curvy CNF.

132

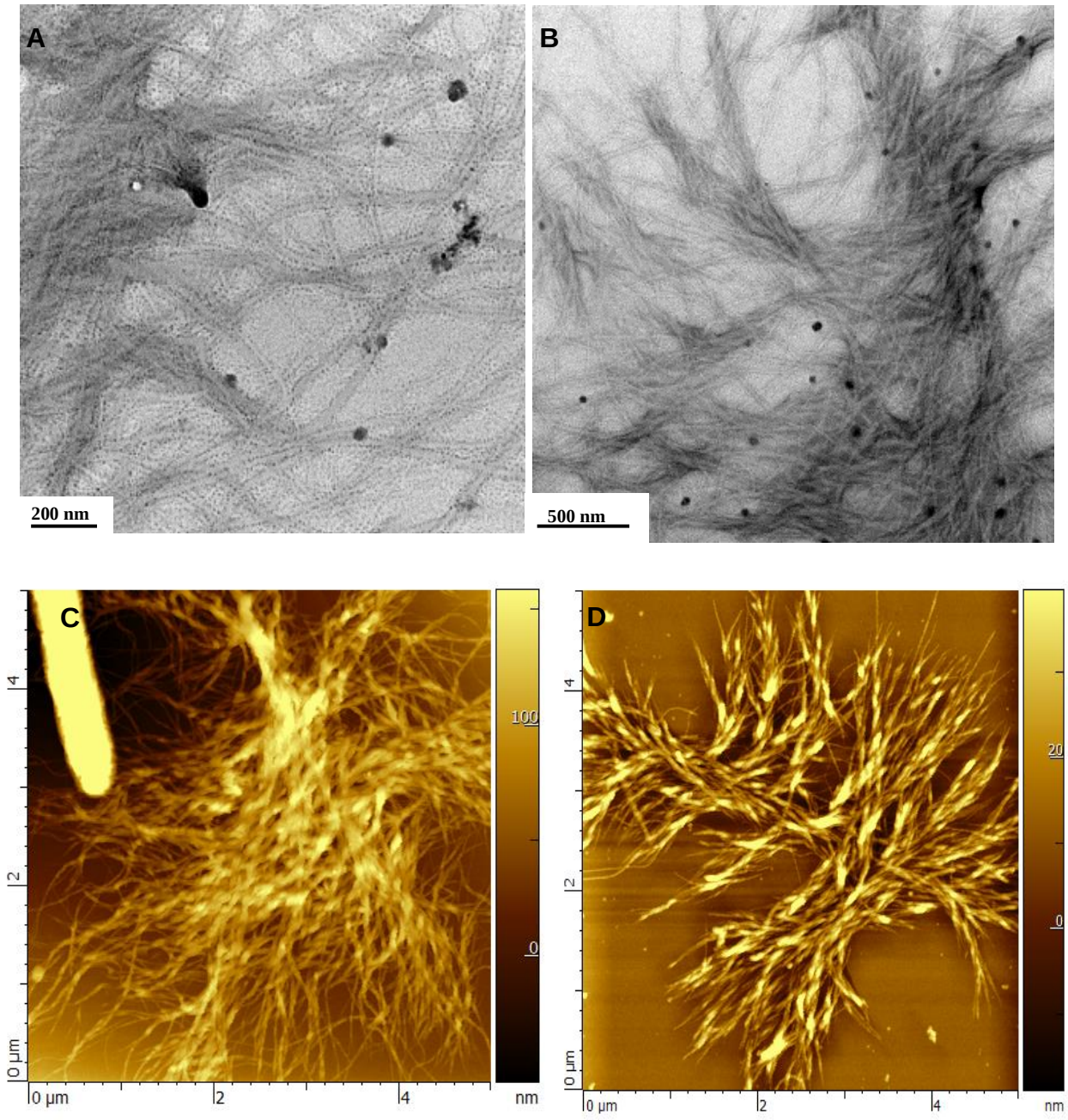

Figure 1. 2 (A) & (B) TEM images of CNF, **(C) & (D)** AFM images of CNF on a formvar coated TEM grid.

133

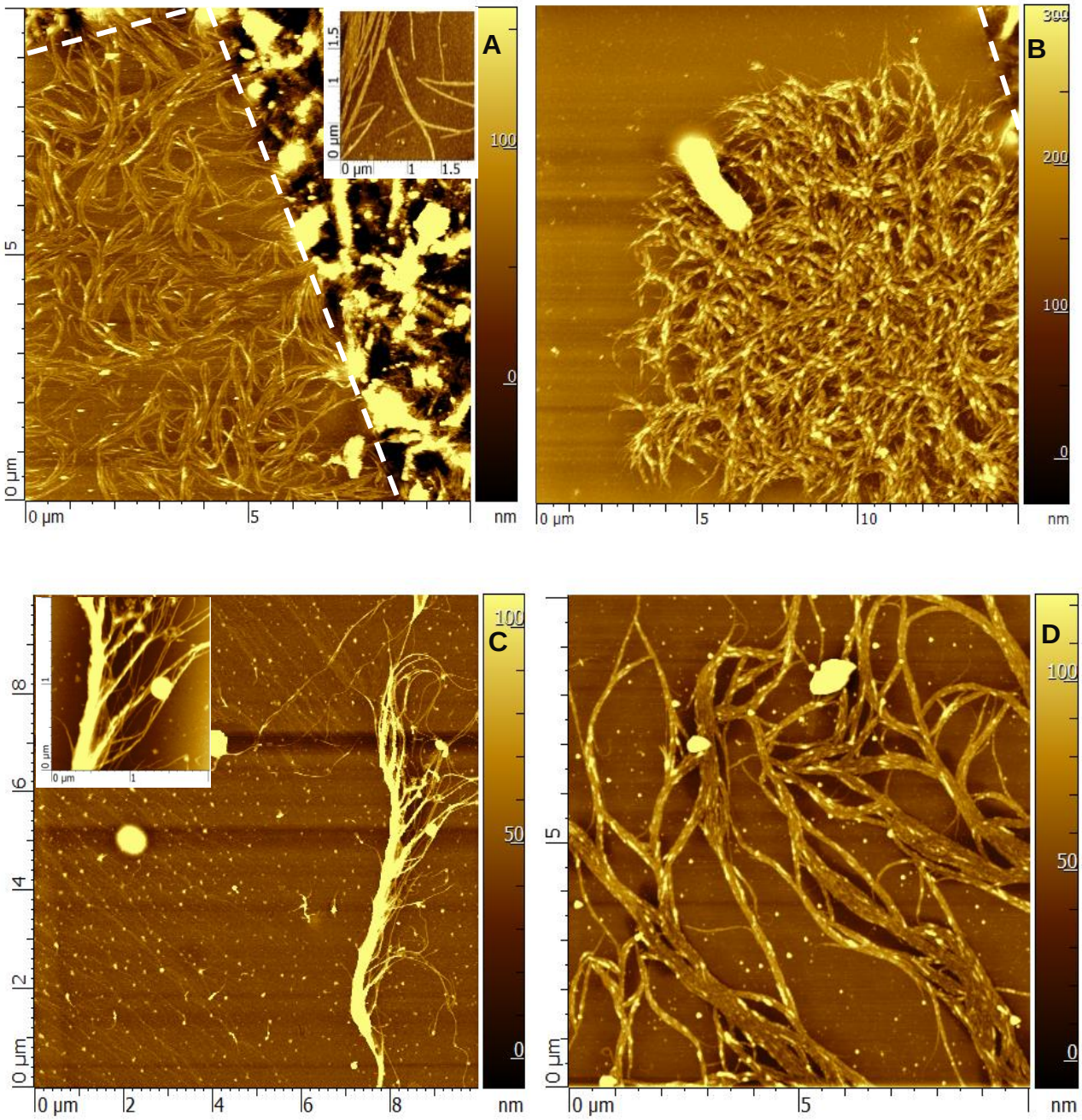

Figure 1. 3 AFM images of CNF **(A)** CNF on plasma treated TEM grid (The white dashed line indicates the boundary between copper and suspended formvar film). **(B)** Tightly entangled CNF on TEM grid. **(C)** Entangled CNF. **(D)** A 48 hour CNC hydrothermal conversion product showing similar CNF structures.

The tendency of CNF to form the bundles on TEM grids suggests strong hydrophobic interactions, most likely the pi-stacking between individual fibers. At the

same time, their partial dispersibility in water as well as the adsorption onto hydrophilic Si wafers indicates the presence of polar surface groups such as -OH, -COOH, and -C=O that are expected after the HTC. [21] It was previously reported that carbon nanoparticles produced via HTC of cellulose were composed of a hydrophobic core with a hydrophilic shell.[6] By making formvar surface less hydrophobic via longer plasma treatment, we were able to observe individual CNF on copper TEM grids using AFM (Fig.1.3 A). Both AFM and TEM images revealed that some structures appeared as particles were actually tightly entangled fibers. (Fig.1.2, Fig. 1.3 B&C). The fiber entanglement can also explain a peculiar observation related to why CNF were observed only after significant dilution of Sample C, 15 times dilution produced some CNF and many particles, whereas dilutions by as much as 1000 times yielded predominantly CNF with a substantially smaller number of particles as was observed in the images. It is known that, when polymers are dispersed in solvents, the individual molecules adapt configurations with a different degree of entanglement depending upon their concentration (Fig.1.3).[22] Higher concentrations favor more coiled structures because of the screening of excluded volume interactions.[23] The presence of negatively charged groups on the surface of the CNF also permitted the negative staining of fibers with uranyl acetate, in which the uranyl salt particles were predominantly concentrated on the surface of CNF bundles (Fig. 1.2 A&B). A 48 hour CNC hydrothermal conversion was also conducted yielding similar CNF structure as shown in Fig. 1.3 D. Potential dissolution states of CNF is shown in Fig. 1.4, showing Sample C has nanorods may be-coiled CNF.

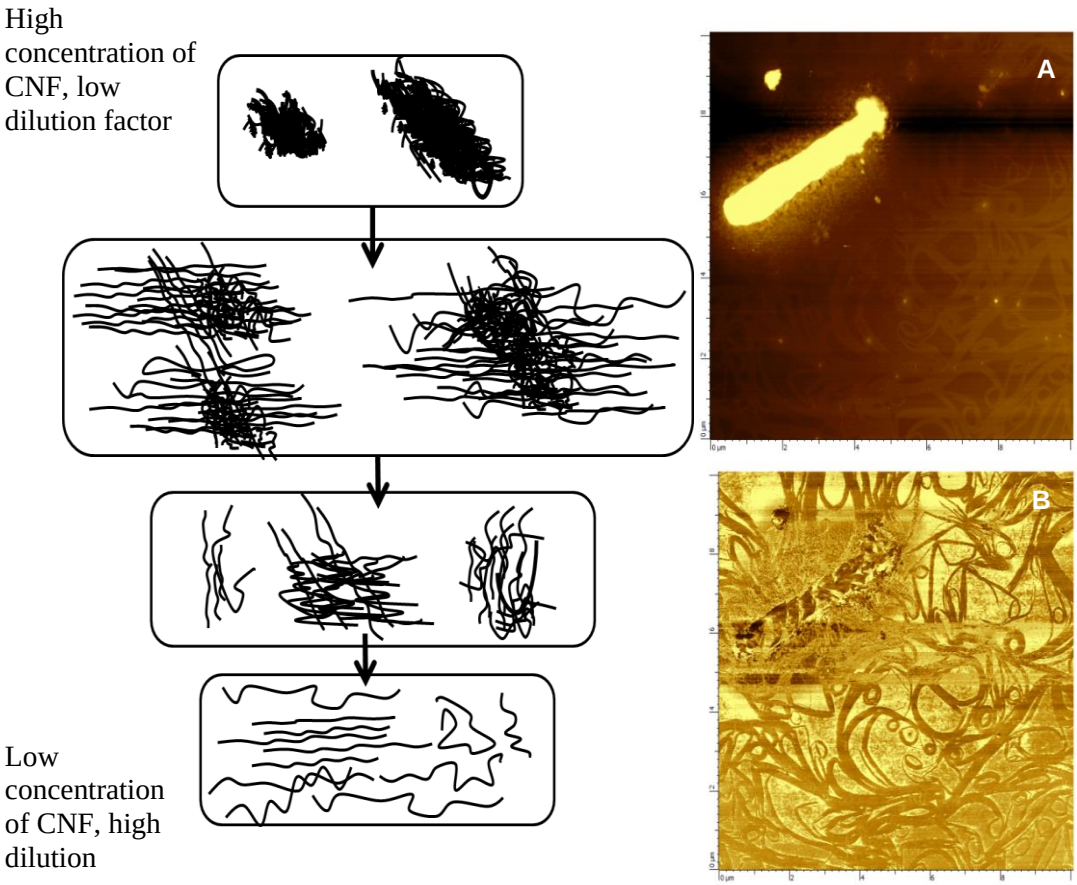

Figure 1. 4 Potential dissolution states of CNF. Images **(A)** & **(B)** showing Sample C has nanorods may be-coiled CNF.

Further characterization of the CNF was carried out using PXRD and Raman spectroscopy of Samples B and the results were compared to those from CNC. Samples B were chosen for PXRD and Raman characterization due to presumably higher concentrations of CNF. The PXRD peaks of CNC were assigned as $(1\bar{1}0)$, (110), (200), and (004) (Fig. 1.5 A).[24-28] Using the PXRD data, the mean size of CNC calculated by Scherrer equation and the crystallinity index were 6.4 nm and 87%, respectively. The crystallinity index was calculated

using the amorphous subtraction method, in which the intensity of the crystalline peak (200) was compared to the total intensity of amorphous peak after the subtraction of the background signal measured without the cellulose. [22] The CNC crystalline index can also be calculated using Raman spectrum by comparing the peak intensities at 380 cm^{-1} and 1096 cm^{-1}.[29, 30] In our case, the crystallinity index calculated using Raman spectrum (Fig. 1.5 A) is 68%.[31]

$$(Crystallinity\ Index) = \frac{\frac{I_{380}}{I_{1096}} - 0.0286}{0.0065}$$

PXRD peaks characteristic of CNC disappeared after the HTC indicating the complete disintegration of CNC.[6] At the same time, no unique PXRD peaks that can be possibly assigned to CNF were observed after the HTC suggesting that the small individual nanofibers may not packed in crystalline domains sufficiently large to produce PXRD patterns. [20, 32, 33]

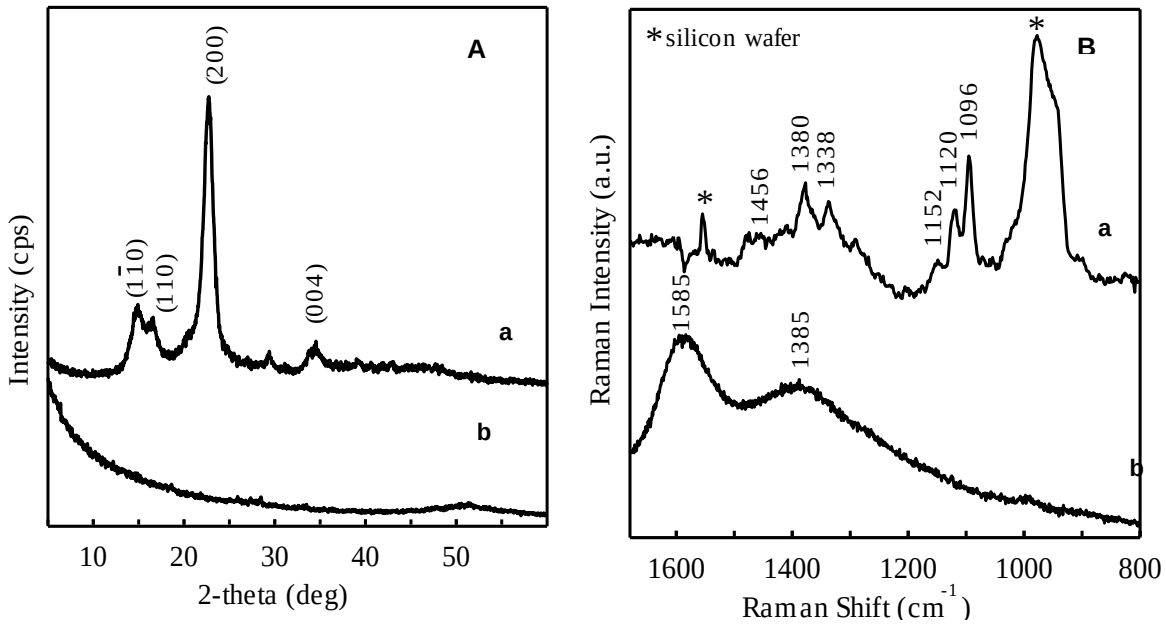

Figure 1. 5 (A) PXRD **(B)** Raman Spectra of CNC (a) and CNF (b).

Raman Peak Position (cm^{-1})	Types of vibrations
380,437,520 cm^{-1}	stretching of COC, CCO, CCC, CO
898 cm^{-1}	bending of HCC and HCO at C_6
1096 cm^{-1}	symmetric ring breathing vibrations of COC groups, stretching of CC and CO
1121 cm^{-1}	CC and CO stretching motions parallel to chain axis
1152 cm^{-1}	asymmetric vibrations of CC & CO stretching (ring breathing)
1338 cm^{-1}	HCC, HCO & HOC bending
1380 cm^{-1}	deformation vibrations of cellulose backbone of HCH, HCC, HCO & COH
1456 cm^{-1}	bending vibrations of HCH & small proportion of COH
1508 cm^{-1}	HCH bending

Table 1. 1 Assignment of CNC Raman spectrum.

Raman spectrum of CNC revealed strong peaks at 380 cm^{-1}, 1096 cm^{-1}, 1120 cm^{-1}, 1152cm^{-1}, 1336 cm^{-1} and 1380 cm^{-1}, detail interpretation of CNC Raman spectra can be found in Table 1.1.[34-36] Raman spectra of Sample B exhibited broad peaks around 1385 cm^{-1} (FWHM 228.95 cm^{-1}) and 1585 cm^{-1} (FWHM 90.43 cm^{-1}) that were assigned to D and G bands of carbon species, respectively. [36-38] The G-band is the primary mode in sp2 carbon representing the vibration in the planar sheet configuration, whereas D-band can be also an open end of carbon nanotubes, edges of graphite sheets or disruptions in the planar sp2 carbon hybridization.[39] The spectrum in Fig. 1.5 B, curve b represents a typical Raman spectrum of carbonaceous products obtained after high temperature pyrolysis of organic compounds. A similar spectrum was also previously

assigned to carbon nanofiber fabricated by electrospinning. [40] No other unique bands that can be assigned to CNF were detected suggesting that the small individual fibers were not packed in crystalline domains sufficiently large to produce PXRD patterns. The CNC disintegration was also confirmed by TGA and DTA (Fig.1.6 A). The TGA and DTA results confirmed that the decomposition of CNC happened around 175 ℃, which is lower than HTC temperature (240 ℃) used in this work. The results are similar to those in reference.[26]

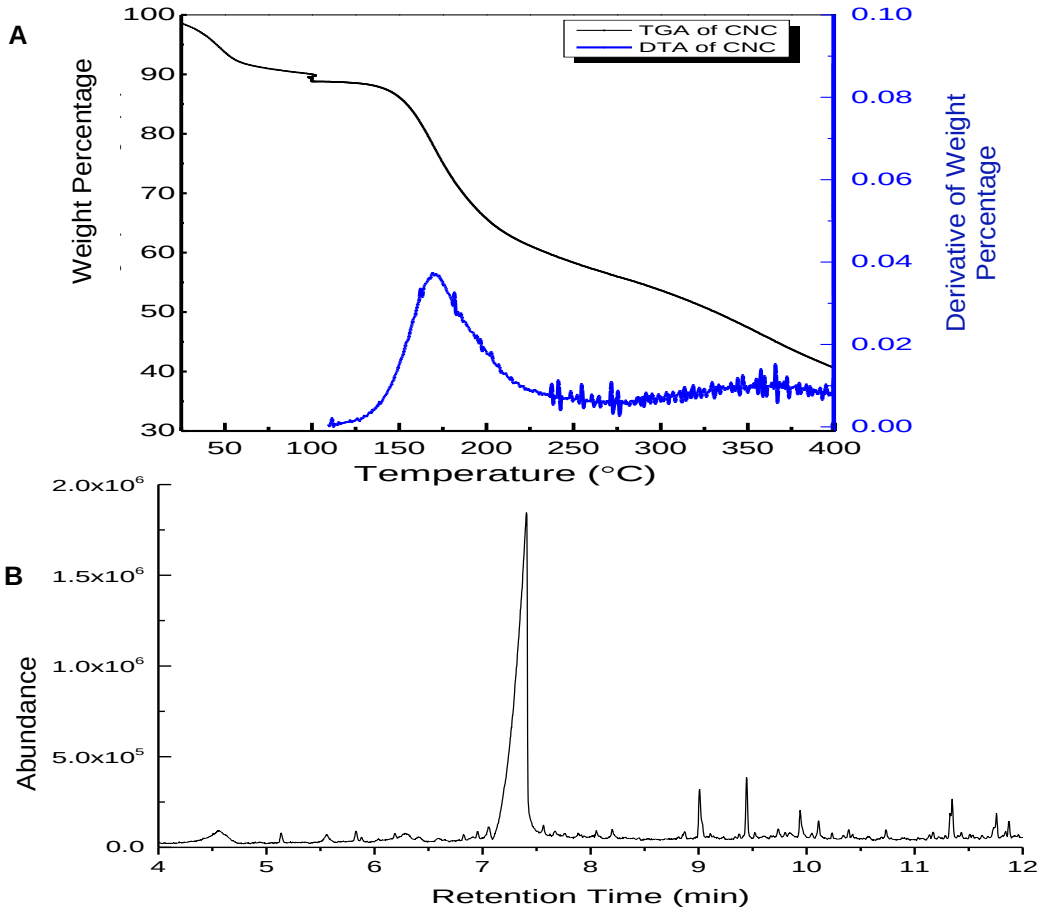

Figure 1. 6 (A) Thermogravimetric analysis (TGA) and differential thermal analysis (DTA) of CNC. **(B)** GC-MS analysis of Sample A from hydrothermal conversion of CNC.

198 Sample A (heavy oil, liquid product) was separated from the precipitate using
199 centrifugation. Gas Chromotography Mass Spectroscopy of Sample A was shown in Fig.
200 1.5 B and Table 1.2. Some small molecular acids, ketones, phenol,[41] levulinic acid,[42]
201 phenol and quinone derivatives were detected. Main components of the Sample A after
202 hydrothermal conversion of CNC was shown in Table 1.2.

Retention Time (min)	Area Percentage (%)	Name	Similarity Index (%)
4.562	1.74	2(3H)-Furanone	93
5.136	0.41	2(3H)-Furanone, 5-methyl-	90
5.554	0.7	2-Cyclopenten-1-one, 2-methyl-	87
5.83	0.48	p-Benzoquinone	86
6.189	0.12	2(3H)-Furanone	91
6.281	0.77	2,4-Dimethylfuran	81
6.956	0.44	2-Cyclopenten-1-one, 2-hydroxy-3-methyl-	73
7.058	1.18	2-Cyclopenten-1-one, 2,3-dimethyl-	84
7.407	75.52	Levulinic acid	95
8.053	0.21	1,3-Cyclohexanedione, 2-methyl-	72
8.056	0.88	2(3H)-Furanone, 5-methyl-	80
8.203	0.59	Octanoic acid	84
9.011	2.46	Hydroquinone	94
9.444	2.52	p-Menth-3-en-2-one	89
9.521	0.44	Tetrahydrocarvone	82
9.843	0.7	1,3-Dioxolane, 2-cyclohexyl-4,5-dimethyl-	75
9.943	1.92	Ethanone, 1-(3-hydroxyphenyl)-	94
10.112	1.14	Phenol, 4-butoxy-	83
10.237	0.41	Acetophenone, 4'-hydroxy-	85
10.39	1.15	4-Hydroxy-3-methylacetophenone	86
10.737	0.7	7a-Methyl-3-methylenehexahydrobenzofuran-2-	80
11.347	2.36	4-Hydroxy-1-indanone	87
11.758	1.59	7H-Indeno[5,6-b]furan-7-one,4,4a,5,6,7a,8-	78
11.874	1.11	Benzeneacetic acid, .alpha.-formyl-, ethyl ester	73
11.923	0.46	5-Hydroxy-3-methyl-1-indanone	72

203 **Table 1. 2** Main components of Sample A analyzed by GC-MS.

1.4 Conclusion

CNC is an important new engineering material in cellulose science due to its unique properties such as low density, biodegradability, high aspect ratio, high strength and stiffness. [11-13] Carbon nanofibers with the diameter of a few nanometers and tens of micrometers length can be synthesized via the hydrothermal conversion of CNC at 240 ℃ without catalyst. This method is environmentally friendly, does not require toxic chemicals and has commercial potential for inexpensive production of carbon nanofiber.[43] Some examples of CNF AFM images were shown in Fig. 1.7.

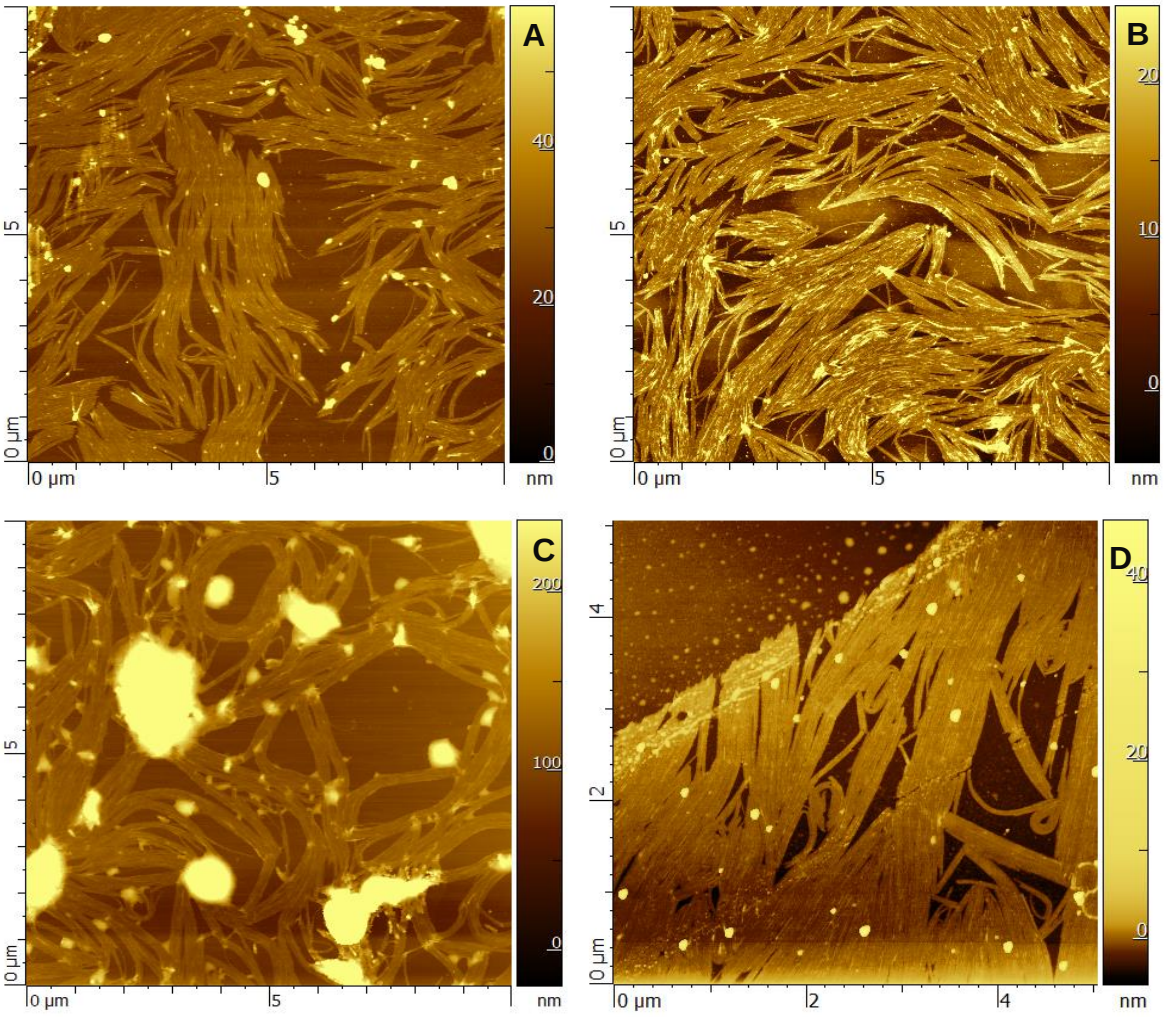

Figure 1. 7 Examples of AFM images of CNF.

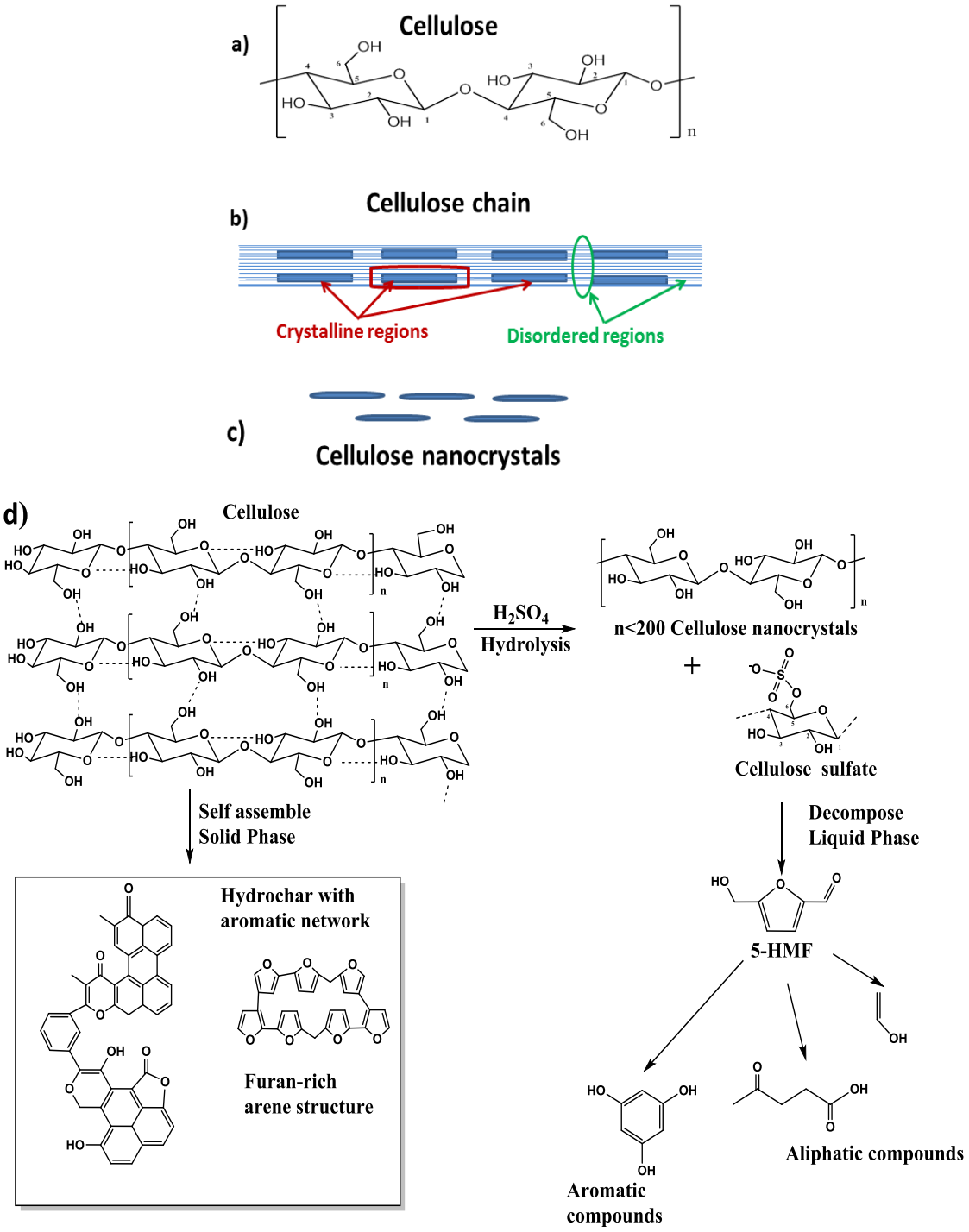

Figure 1. 8 a) Schematics of a single cellulose chain repeat unit showing the directionality of the β (1→4) glycosidic bond and hydrogen bonding. b) Idealized cellulose microfibril showing disordered and crystalline regions. c) Cellulose nanocrystals from acid hydrolysis of cellulose by dissolving the disordered regions.[1] d) Proposed possible reactions of cellulose nanocrystals degradation in hydrothermal conversion.

213

The following mechanism for the formation of CNF observed in these studies was hypothesized and shown in Fig. 1.8. Compared to cellulose, CNC has a higher crystallinity index, which implies more homogenous crystalline domains are present in CNC. The crystallinity degree has been shown playing a very important role in the hydrothermal conversion of cellulose material. [44] Cellulose is known to maintain its fibrous skeleton after carbonisation.[42, 45] Camillo Falco suggested polyaromatic hydrocarbons and furan-rich arene structures as dehydration products. [43] These five/six unsaturated carbon member rings may work as the precursors for carbon nanofiber synthesis. Yury Gogotsi's group reported the hydrothermal synthesis of multiwall carbon nanotubes using polyethylene/water mixtures in the presence of nickel at 700–800 ℃ under 60–100 MPa pressure in 2000.[10] Masahiro Yoshimura's group reported the synthesis of hollow carbon nanotubes by hydrothermal conversion of amorphous carbon at 800 ℃, 100 MPa without metal catalyst in 2001.[13] Mukul Kumar and Yoshinori Ando published on the synthesis of single and multiwall carbon nanotubes from pyrolysis of camphor.[46] It has been a tradition to synthesize carbon nanomaterial from macroscopic carbon resources. However, CNC has nanometer size dimension and higher crystallinity compared with cellulose. CNC show liquid crystal character and tend to self-assemble to form fibrous structures in suspension when temperature or ionic strength increases.[47-49] In this mechanism, the self-assembled CNC provide the initial template for the formation of CNF. The self-assembly takes place at temperatures lower than that of the CNC decomposition (~175 ℃, Fig.1.5 A) and is facilitated by the desulfation process.[48] As the temperature increases during the HTC conversion, the CNC first self-

assemble into fibrous structure and then undergo carbonization. The newly formed aromatic carbon reorganizes into a more stable nanofibrous form appearing as CNF.[50, 51] The individual CNF can stack into larger ribbons and bundles as observed by AFM and TEM (Fig.1.2 & 1.3). The size and shape of the ribbons and bundles are determined by the morphology of the fibrous structures resulted from the self-assembly of CNC prior to the carbonization. Understanding the mechanism of how CNC can be converted into carbon nanofibers may explain the presence of carbon nanofibers/nanotubes in nature. Even though the diameter of the observed CNF is in the same range as that of carbon nanotubes [52, 53], it was not possible to make the positive identification based on the data presented here.

Levulinic acid was produced as the major product for after HTC of CNC, Levulinic acid is considered as a platform chemical with high potential by US Department of Energy in 2004. [54] The production of levulinic acid and CNF allows us to produce valuable and useful byproducts from cellulosic wastes from agriculture and food industry.

1.5 Acknowledgments

I like to acknowledge the Clemson University Center for Optical Materials Science and Engineering Technologies for help in getting electron microscope images. Dr. Christopher L. Kitchens and his student Mingzhe Jiang for providing us CNC for collaboration work.

1.6 References

[1] R.J. Moon, A. Martini, J. Nairn, J. Simonsen, J. Youngblood, Cellulose nanomaterials review: structure, properties and nanocomposites, Chemical Society Reviews, 40(2011) 3941-94.

[2] W. Chen, H. Yu, Y. Liu, P. Chen, M. Zhang, Y. Hai, Individualization of cellulose nanofibers from wood using high-intensity ultrasonication combined with chemical pretreatments, Carbohydrate Polymers, 83(2011) 1804-11.

[3] P. Lu, Y.-L. Hsieh, Preparation and characterization of cellulose nanocrystals from rice straw, Carbohydrate Polymers, 87(2012) 564-73.

[4] Y. Wang, G. Yao, F. Jin, Hydrothermal Conversion of Cellulose into Organic Acids with a CuO Oxidant, in: F. Jin (Ed.) Application of Hydrothermal Reactions to Biomass Conversion, Springer Berlin Heidelberg2014, pp. 31-59.

[5] M.M. Tang, R. Bacon, Carbonization of cellulose fibers—I. Low temperature pyrolysis, Carbon, 2(1964) 211-20.

[6] M. Sevilla, A.B. Fuertes, The production of carbon materials by hydrothermal carbonization of cellulose, Carbon, 47(2009) 2281-9.

[7] M. Sevilla, A.B. Fuertes, Graphitic carbon nanostructures from cellulose, Chemical Physics Letters, 490(2010) 63-8.

[8] A.M. Herring, J.T. McKinnon, B.D. McCloskey, J. Filley, K.W. Gneshin, R.A. Pavelka, et al., A Novel Method for the Templated Synthesis of Homogeneous Samples of Hollow Carbon Nanospheres from Cellulose Chars, Journal of the American Chemical Society, 125(2003) 9916-7.

[9] S.S. Toor, L. Rosendahl, A. Rudolf, Hydrothermal liquefaction of biomass: A review of subcritical water technologies, Energy, 36(2011) 2328-42.

[10] Y. Gogotsi, J.A. Libera, M. Yoshimura, Hydrothermal synthesis of multiwall carbon nanotubes, Journal of Materials Research, 15(2000) 2591-4.

[11] A.R. Siskin M Fau - Katritzky, A.R. Katritzky, Reactivity of organic compounds in hot water: geochemical and technological implications, Science, 254(1991) 231-7.

[12] I. Pavlovic, Z. Knez, M. Skerget, Subcritical Water-a Perspective Reaction Media for Biomass Processing to Chemicals: Study on Cellulose Conversion as a Model for Biomass, Chem BiochemEng, 27(2013) 73-82.

[13] J.M. Calderon Moreno, M. Yoshimura, Hydrothermal Processing of High-Quality Multiwall Nanotubes from Amorphous Carbon, Journal of the American Chemical Society, 123(2001) 741-2.

[14] Y. Gogotsi, J. Libera, M. Yoshimura, Hydrothermal Synthesis of Multiwall Carbon Nanotubes2000.

[15] H. Das, S.K. Singh, Useful Byproducts from Cellulosic Wastes of Agriculture and Food Industry—A Critical Appraisal, Critical Reviews in Food Science and Nutrition, 44(2004) 77-89.

[16] W. Kern, The Evolution of Silicon Wafer Cleaning Technology, Journal of The Electrochemical Society, 137(1990) 1887-92.

[17] E.E. Ureña-Benavides, G. Ao, V.A. Davis, C.L. Kitchens, Rheology and Phase Behavior of Lyotropic Cellulose Nanocrystal Suspensions, Macromolecules, 44(2011) 8990-8.

303 [18] C. Salas, T. Nypelö, C. Rodriguez-Abreu, C. Carrillo, O.J. Rojas, Nanocellulose
304 properties and applications in colloids and interfaces, Current Opinion in Colloid &
305 Interface Science, 19(2014) 383-96.
306 [19] M. Mariano, N. El Kissi, A. Dufresne, Cellulose nanocrystals and related
307 nanocomposites: Review of some properties and challenges, Journal of Polymer Science
308 Part B: Polymer Physics, 52(2014) 791-806.
309 [20] Y. Wen, M. Jiang, C.L. Kitchens, G. Chumanov, Synthesis of carbon nanofibers via
310 hydrothermal conversion of cellulose nanocrystals, Cellulose, 24(2017) 4599-604.
311 [21] S. Beck, J. Bouchard, R. Berry, Dispersibility in Water of Dried Nanocrystalline
312 Cellulose, Biomacromolecules, 13(2012) 1486-94.
313 [22] D. Klemm, B. Heublein, H.-P. Fink, A. Bohn, Cellulose: Fascinating Biopolymer
314 and Sustainable Raw Material, Angewandte Chemie International Edition, 44(2005)
315 3358-93.
316 [23] J.F. Douglas, K.F. Freed, Competition between Hydrodynamic Screening
317 ("Draining") and Excluded Volume Interactions in an Isolated Polymer Chain,
318 Macromolecules, 27(1994) 6088-99.
319 [24] M. Wada, L. Heux, J. Sugiyama, Polymorphism of Cellulose I Family:
320 Reinvestigation of Cellulose IVI, Biomacromolecules, 5(2004) 1385-91.
321 [25] Y. Tang, S. Yang, N. Zhang, J. Zhang, Preparation and characterization of
322 nanocrystalline cellulose via low-intensity ultrasonic-assisted sulfuric acid hydrolysis,
323 Cellulose, 21(2014) 335-46.

[26] A. Kumar, Y.S. Negi, V. Choudhary, N.K. Bhardwaj, Characterization of Cellulose Nanocrystals Produced by Acid-Hydrolysis from Sugarcane Bagasse as Agro-Waste, Journal of Materials Physics and Chemistry, 2(2014) 1-8.

[27] S. Vivekanandhan, L. Christensen, M. Misra, A.K. Mohanty, Green Process for Impregnation of Silver Nanoparticles into Microcrystalline Cellulose and Their Antimicrobial Bionanocomposite Films, Journal of Biomaterials and Nanobiotechnology, Vol.03No.03(2012) 6.

[28] X. Wu, C. Lu, W. Zhang, G. Yuan, R. Xiong, X. Zhang, A novel reagentless approach for synthesizing cellulose nanocrystal-supported palladium nanoparticles with enhanced catalytic performance, Journal of Materials Chemistry A, 1(2013) 8645-52.

[29] U.P. Agarwal, R.H. Atalla, A. Isogai, Nanocelluloses: Their Preparation, Properties, and Applications, ACS Symposium Series, American Chemical Society2017.

[30] U. Agarwal, R. S. Reiner, S. A. Ralph, Cellulose I crystallinity determination using FT-Raman spectroscopy: Univariate and multivariate methods2010.

[31] S. Park, J.O. Baker, M.E. Himmel, P.A. Parilla, D.K. Johnson, Cellulose crystallinity index: measurement techniques and their impact on interpreting cellulase performance, Biotechnology for Biofuels, 3(2010) 10-.

[32] A. Cao, C. Xu, J. Liang, D. Wu, B. Wei, X-ray diffraction characterization on the alignment degree of carbon nanotubes, Chemical Physics Letters, 344(2001) 13-7.

[33] Z.Q. Li, C.J. Lu, Z.P. Xia, Y. Zhou, Z. Luo, X-ray diffraction patterns of graphite and turbostratic carbon, Carbon, 45(2007) 1686-95.

345 [34] U. Agarwal, R. Reiner, S. Ralph, Cellulose I crystallinity determination using FT–
346 Raman spectroscopy: univariate and multivariate methods, Cellulose, 17(2010) 721-33.
347 [35] H.A. Rajai, The Structures of Cellulose: American Chemical Society; 1987.
348 [36] J.H. Wiley, R.H. Atalla, Band assignments in the raman spectra of celluloses, IPST
349 Technical Paper Series, 160(1987) 113-29.
350 [37] U.P. Agarwal, R.S. Reiner, S.A. Ralph, Determination of cellulose I crystallinity by
351 FT-raman spectroscopy, Proceedings of 15th international symposium on wood, fiber and
352 pulping chemistry (2009) P-053, 4
353 [38] S. Osswald, M. Havel, Y. Gogotsi, Monitoring oxidation of multiwalled carbon
354 nanotubes by Raman spectroscopy, Journal of Raman Spectroscopy, 38(2007) 728-36.
355 [39] R. Saito, M. Hofmann, G. Dresselhaus, A. Jorio, M.S. Dresselhaus, Raman
356 spectroscopy of graphene and carbon nanotubes, Advances in Physics, 60(2011) 413-550.
357 [40] Y. Wang, S. Serrano, J.J. Santiago-Avilés, Raman characterization of carbon
358 nanofibers prepared using electrospinning, Synthetic Metals, 138(2003) 423-7.
359 [41] Z. Wang, W. Lin, W. Song, Liquid product from hydrothermal treatment of cellulose
360 by direct GC/MS analysis, Applied Energy, 97(2012) 56-60.
361 [42] Y. Gao, X.-H. Wang, H.-P. Yang, H.-P. Chen, Characterization of products from
362 hydrothermal treatments of cellulose, Energy, 42(2012) 457-65.
363 [43] B. Hu, S.-H. Yu, K. Wang, L. Liu, X.-W. Xu, Functional carbonaceous materials
364 from hydrothermal carbonization of biomass: an effective chemical process, Dalton
365 Transactions, (2008) 5414-23.

366 [44] M. Moller, F. Harnisch, U. Schroder, Hydrothermal liquefaction of cellulose in
367 subcritical water-the role of crystallinity on the cellulose reactivity, RSC Advances,
368 3(2013) 11035-44.
369 [45] S. Kang, X. Li, J. Fan, J. Chang, Characterization of Hydrochars Produced by
370 Hydrothermal Carbonization of Lignin, Cellulose, d-Xylose, and Wood Meal, Industrial
371 & Engineering Chemistry Research, 51(2012) 9023-31.
372 [46] M. Kumar, Y. Ando, Single-wall and multi-wall carbon nanotubes from camphor—a
373 botanical hydrocarbon, Diamond and Related Materials, 12(2003) 1845-50.
374 [47] F. Cherhal, F. Cousin, I. Capron, Influence of charge density and ionic strength on
375 the aggregation process of cellulose nanocrystals in aqueous suspension, as revealed by
376 small-angle neutron scattering, Langmuir, 31(2015) 5596-602.
377 [48] L. Lewis, M. Derakhshandeh, S.G. Hatzikiriakos, W.Y. Hamad, M.J. MacLachlan,
378 Hydrothermal Gelation of Aqueous Cellulose Nanocrystal Suspensions,
379 Biomacromolecules, 17(2016) 2747-54.
380 [49] X.M. Dong, J.F. Revol, D.G. Gray, Effect of microcrystallite preparation conditions
381 on the formation of colloid crystals of cellulose, Cellulose, 5(1998).
382 [50] P.M. Visakh, M. Liang, Poly(Ethylene Terephthalate) Based Blends, Composites
383 and Nanocomposites, Oxford: William Andrew Publishing; 2015.
384 [51] A.F. ISMAIL, P.S. GOH, J.C. TEE, S.M. SANIP, M. AZIZ, A REVIEW OF
385 PURIFICATION TECHNIQUES FOR CARBON NANOTUBES, Nano, 03(2008) 127-
386 43.

[52] O.A. Shenderova, V.V. Zhirnov, D.W. Brenner, Carbon Nanostructures, Critical Reviews in Solid State and Materials Sciences, 27(2002) 227-356.

[53] Y.A. Kim, T. Hayashi, M. Endo, M.S. Dresselhaus, Carbon Nanofibers, in: R. Vajtai (Ed.) Springer Handbook of Nanomaterials, Springer Berlin Heidelberg2013, pp. 233-62.

[54] T. Werpy, G. Petersen, Top Value Added Chemicals from Biomass: Volume I -- Results of Screening for Potential Candidates from Sugars and Synthesis Gas, United States, 2004.

CHAPTER TWO

PMMA Stabilized 2D Silver Nanoparticle Array as a Sensing Scaffold

2.1 Introduction

Michael Faraday (1791-1867) was the first one to recognize the unique properties of gold and other metal nanoparticles in 1856-57.[1] In recent years, noble metal nanoparticles have been the focus of intense research because of their unique potential applications in optical, electrical, chemical and catalysis fields.[2, 3] Silver nanoparticles can interact with visible light with high efficiency via the excitation of plasmon resonances.[4] When the particle size is comparable to the wavelength of visible light, the particle's free electrons participate in the collective oscillations that are termed localized surface plasmon resonance (LSPR). (Fig.2.1) This plasmon effect is highly localized at the nanoparticle surface and decays rapidly with distance from the nanoparticle-dielectric interface.[5] The particle's optical extinction will exhibit a maximum at the plasmon resonance frequency. Excitation of plasmon resonance will produce an enhanced electromagnetic field localized around AgNP. The position and shape of the resonance peak is highly dependent on the refractive index of the surrounding medium.[6] The bulk refractive index changes in the surrounding environment can be easily detected through changes in the position and shape of the LSPR peak. When silver nanoparticles are organized into close proximity (2D array of nanoparticles), the electron oscillations in

individual particles overlap with the localized plasmon resonance, the system undergoes plasmon coupling resulting a sharp LSPR peak in the blue spectral range of the extinction spectra.[7] 2D AgNP arrays developed in our group have been previously used for sucrose sensing based on their LSPR properties. Naked 2D AgNP arrays are unstable when taken out of solution or upon exposure to analytes. They have a tendency to aggregate once the solvent evaporates. In this chapter, we describe the idea of stabilizing 2D AgNP array with PMMA in order to build a robust sensing scaffold. The PMMA stabilized 2D AgNP arrays were used to detect the bulk refractive index (RI) changes and linear responses was obtained between the concentrations of saccharide and the differential optical signals, as described later. To explore the sensing capabilities of these arrays, a responsive layer of polymer was coated on the array surface to sense volatile organic compound (VOC) in the environment. Toluene, chloroform, acetone and ethanol were used to prove the concept for VOC sensing.

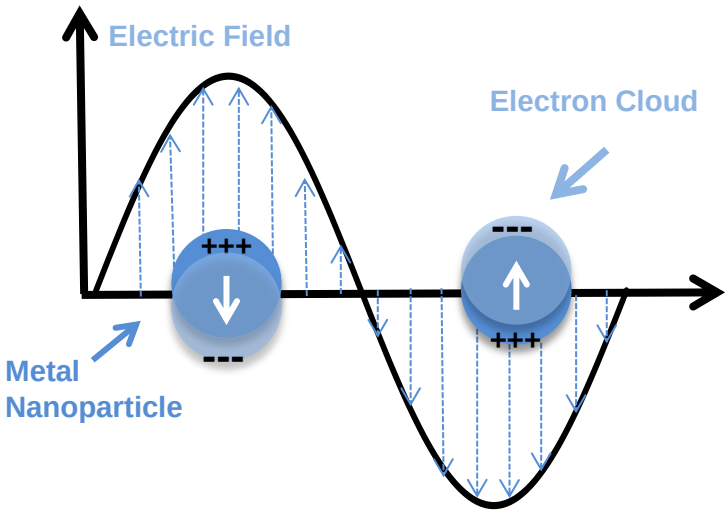

Figure 2. 1 Schematic illustration of a localized surface plasmon resonance.

2.2 Materials and Methods

2.2.1 Materials

Deionized water with a nominal resistivity of 18MΩ·cm was obtained from a Millipore Milli-Q water purification system. Silver (I) oxide (99.99%), anhydrous sodium sulfate (99.99%), polyvinyl acetate (PVAC, MW ~50000) were acquired from Alfa Aesar. Anisole (anhydrous, 99.7%), poly (4-vinylpyridine) (PVP, MW~160000), poly (butyl methacrylate) (PBMA, MW~337000), poly (methyl methacrylate) (PMMA, MW~996000), poly (diallyldimethylammonium chloride) (PDDA) (20%wt) solution were purchased from Sigma-Aldrich. Formvar 15/95 resin powder was purchased from Electron Miscroscopy Sciences. USP grade absolute 200 proof ethanol was obtained from Aaper Alcohol & Chemical Co. Sodium metasilicate (SiO_2 44-47%) and fumed silica (99.8%) were purchased from Sigma-Aldrich and purified by heating at 500 °C for 5 hours under vacuum then used in the synthesis of AgNP. Ultra-high purity hydrogen and ultra-high purity nitrogen were purchased from Air Gas. Unless specified, all reagents and solvents were used as received.

2.2.2 Methods

2.2.2.1. Synthesis of AgNP

The AgNP were synthesized by reducing an aqueous saturated solution of silver (I) oxide with ultra-high purity hydrogen at 73 °C and 10 psi in a round bottom flask, as previously reported.[8] The size of the AgNP can be adjusted by controlling the reaction

time and by monitoring the extinction spectra of the reaction suspension. Colloidal suspensions containing 95 ±19 nm AgNP were used in this study.

2.2.2.2. Fabrication of PMMA stabilized 2D AgNP arrays

Microscope slides were cut into 25 × 12.5 mm pieces, cleaned by sonication in acetone, ethanol, and DI water each for 15 min, dried with nitrogen and finally plasma cleaned for 10 min. Clean substrates were rolled in 0.01% - 0.05% PVP in ethanol or 0.5% aqueous PDDA solution for at least 4 h. After PVP exposure, ethanol and water rinses were used to remove weakly adsorbed PVP before placing the slides into an aqueous AgNP (OD = 3 containing 1-1.5 mM sodium sulfate) suspension and rolled overnight to obtain a self-assembled monolayer of AgNP (2D AgNP arrays). Slides with attached AgNP were dipped into water followed by ethanol and then dipped into a 0.05% PMMA anisole solution for 5 min each. After exposure to the PMMA anisole solution, the slides were spun dry at 7000 rpm for 30 s. PMMA stabilized 2D AgNP arrays can be stored in dry or liquid environment.

2.2.2.3. Deposition of responsive polymer on PMMA stabilized 2D AgNP arrays

200 µL of 10%-12.5% polymer PBMA/PVAC/PMMA or 3.3% Formvar toluene solutions were spin-coated on PMMA stabilized 2D AgNP slides at 500 rpm for 30 s. A fabrication scheme of 2D AgNP-polymer nanocomposite films (2DSPNF) is shown in Fig. 2.2.

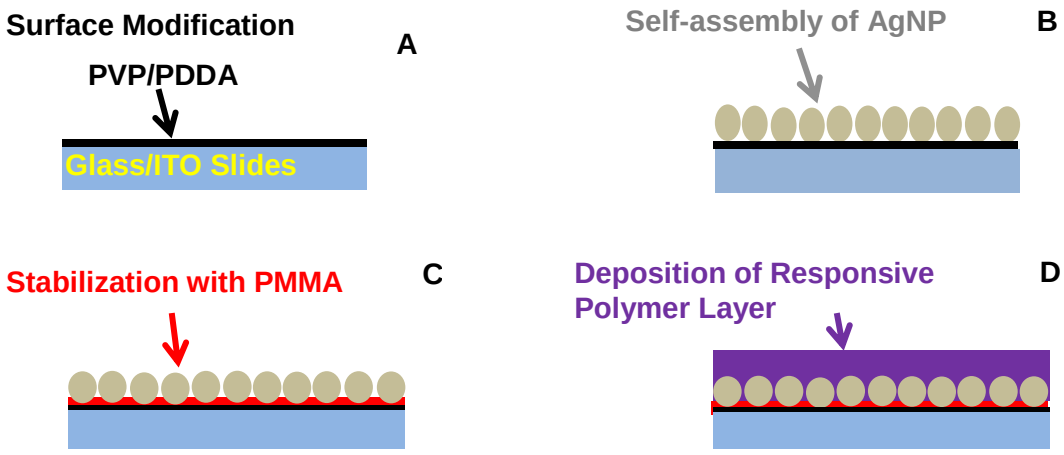

Figure 2. 2 Fabrication of PMMA stabilized 2D AgNP array (A) Modify substrate surface by rolling clean slides in PVP or PDDA solution. **(B).** Self-assemble of AgNP by rolling modified slides in AgNP suspension. **(C).** Stabilize AgNP by spin-coating 0.05% PMMA at 7000 rpm. **(D).** Deposit responsive polymer layer by spin-coating 10-12.5% polymer solution at 500 rpm.

2.3 Instrumentation

UV-2501PC Spectrophotometer (Shimadzu) was used to record UV–Vis spectra. AFM measurements were performed in non-contact mode using AIST-NT SPM Smart system and cantilevers (HQ:NSC14/Al BS-50) from Micromasch. AIST-NT software was used for AFM topography analysis. Home-built LSPR instrumentation consisted of a 150 Watt xenon short arc lamp (Osram), SPEX 500M monochromator equipped with 1800 g/mm grating and a SPEX MSD2 controller. A chopper (SRS) set at 1 kHz was used to modulate the signal. The output slit was replaced with two pinholes permitting the simultaneous selection of two wavelengths. The intensity of light was measured by a pair of Hamamatsu R6094 photomultiplier tubes powered by a McPherson 7640 PMT power supply with two McPherson 671 pre-amplifiers. Signal was processed by SRS 830

DSP lock-in amplifier (Stanford Research Systems). Data was collected using a program written in LabView 2016. [7]

2.4 Results and Discussion

High density 2D AgNP array exhibits coherent plasmon coupling manifested as a sharp LSPR peak in the UV-Vis spectra range.[9] However, un-stabilized 2D AgNP arrays tend to aggregate upon drying which causes the loss of LSPR peaks. The surface aggregation was an irreversible process, and the AgNP remained aggregated upon rewetting. In order to prevent surface aggregation, our group developed the method of physically immobilizing 2D AgNP arrays by casting a layer of PMMA between the particles (Fig. 2.2 C). The thickness of the PMMA layer is governed by the spin-drying speed and the PMMA concentration.[9] The PMMA stabilized 2D AgNP arrays were exposed to sucrose and glucose at different concentrations to see their responses upon bulk refractive index changes in aqueous solution.

A differential optical transmission method previous developed in our lab (Fig. 2.3) was used to provide real time high sensitivity measurements. PMMA stabilized 2D AgNP array exhibit a sharp resonance (typical full width at half maximum (FWHM) around 10-15 nm) due to the coherent plasmon coupling. The sharpness of the resonance presents an opportunity for implementing a differential optical measurement to improve sensitivity and detection limit. The sharper the LSPR peak, the larger the differential signal will be for the differential optical transmission method (Fig. 2.4). When LSPR peak shift due to

the dielectric environment change in the surrounding environment, the extinction at one wavelength increases whereas the extinction at the other wavelength decreases, by monitoring the extinction at two close wavelength, a differential signal can be collected. To implement this, UV-Vis spectra of the PMMA stabilized 2D AgNP array in water were first measured in order to determine the position of the LSPR peak. This information was used to identify the correct position of the monochromator for the differential measurement, so that the two wavelengths excite the sharp peak at both sides from the maximum. The intensity at two wavelengths were then measured by an individual PMT and the signals were processed by the lock-in amplifier displaying the difference between the two PMT signals. After a baseline was measured in DI water, varying concentrations of sucrose from 0.1% to 3.5% were added to change the refractive index from 1.3330 (pure water) to 1.3344 (1% sucrose solution). (Table 2.1).

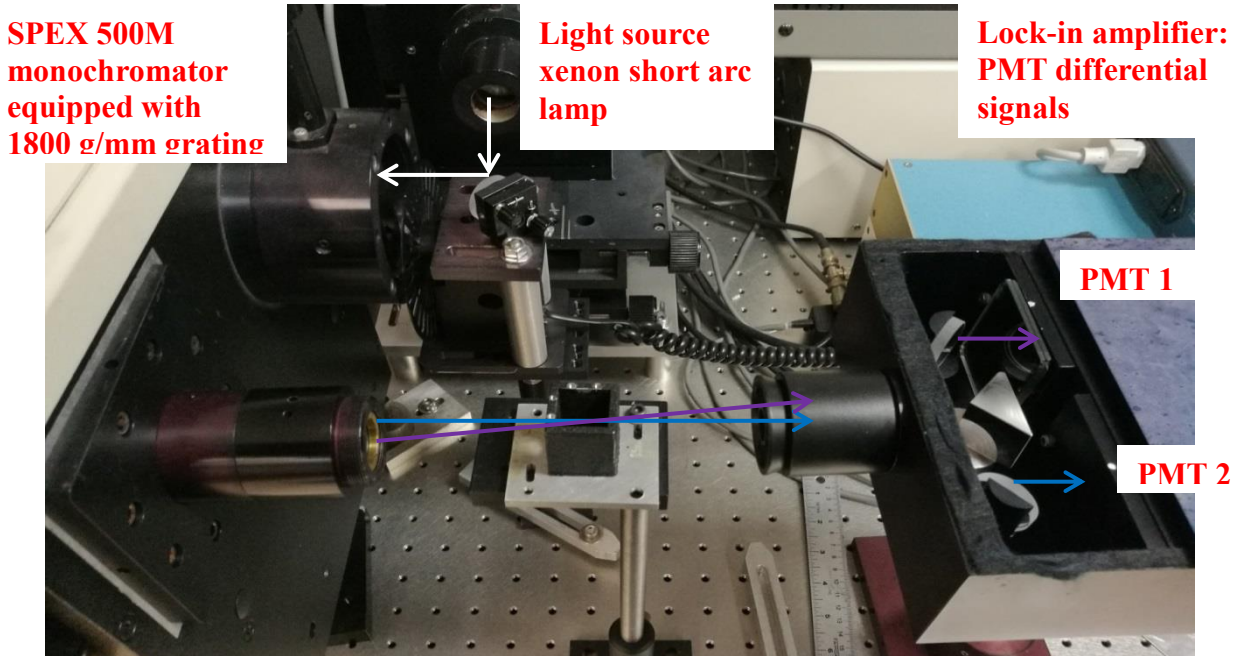

Figure 2. 3 Photo of finished differential optical method instrumentation.

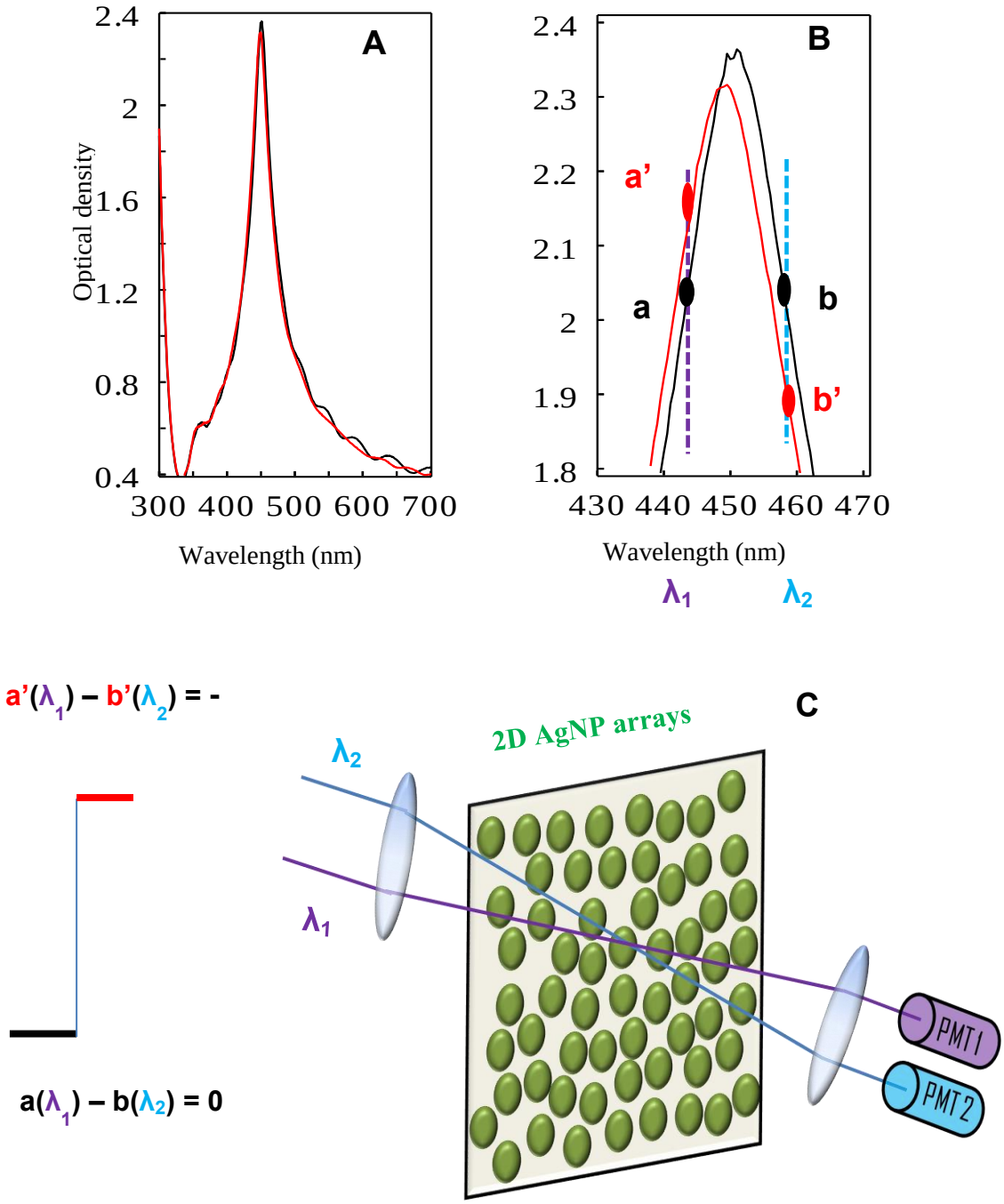

Figure 2. 4 Scheme of how differential optical transmission work. (A). Black curve-UV-Vis spectra of 2D AgNP array, red curve-after expose 2D AgNP array to analyte. **(B).** Enlarge of **Image A** focusing on the differential optical transmission measurement at two close wavelength on each side of LSPR peak, data a/b on the black curve will move to data a'/b' on the red curve, thus the LSPR peak shift caused by analyte can be more accurately measured as differential. **(C)** Schematic illustration of the differential optical transmission method.

524

Density (g/cm^3)	Refractive Index	% by weight (w/v)	Molarity
0.9982	1.3330	0	0
1.0021	1.3344	1	0.029
1.0060	1.3359	2	0.059
1.0099	1.3374	3	0.089

Table 2. 1 Density and refractive indexes of sucrose at different concentration.

Linear relationships between the differential optical transmission measurement signals and the sugar concentrations can be observed in Fig. 2.5 C&D. This is due to the fact that the wavelength of the LSPR peak is dependent on the dielectric function of the medium.[10] This was first discovered by Gustav Mie, who developed the analytical solution to Maxwell's equations that describes the absorption and scattering of light by spherical particles in 1908.[11] The complex dielectric functions of bulk metal nanoparticles were plotted and experimentally determined by Johnson and Christy,[12] which proved the LSPR peak dependence on the surrounding environment's dielectric function. The PMMA stabilized 2D AgNP arrays is an advanced version of our previously developed system comprised of un-protected 2D AgNP arrays that were used for analytical measurements.[7] It was determined that the thin PMMA layer did not have a detrimental effect on the LSPR properties of the nanoarrays when sensing bulk refractive index changes. This PMMA layer also provided stability in dry and aqueous environments. In Fig. 2.5, the detection limit (LOD) was calculated from the signal-to-noise ratio of 3, resulting in LOD of 0.16% for sucrose and 0.17% for glucose. The detection limit of PMMA stabilized 2D AgNP arrays is not as good as naked 2D AgNP arrays due to the fact that a thin PMMA layer was surrounding the AgNP. [7] The

presence of the thin layer of PMMA between the particles was proved by etching away the AgNP. Crater-like structures were observed on glass slides after etching, which implies the polymer filled the space between the particles leaving the nanoparticle surface uncoated.[13] This will make the AgNP in the nanoarrays accessible to various chemical modifications while maintaining its LSPR properties. The purpose of utilizing PMMA stabilized 2D AgNP arrays for sensing saccharide is a prove of concept to show after stabilizing with PMMA, these 2D AgNP arrays are still sensitive to the bulk refractive changes in solution. Our PMMA stabilized 2D AgNP arrays can detect 10^{-4} refractive index unit (RIU) changes, which falls in the reported detection limit for SPR sensors (between 10^{-7} to 10^{-4} RIU).[14, 15]

AFM images showed the average height of AgNP is 95 ± 19 nm on PVP modified glass slides. While after the spin–coating of PMMA, the average height of AgNP was reduced to 78 ± 9 nm, implying the presence of a 13 nm thick PMMA stabilizing layer. The glucose sensing results shown in Fig 2.4 D was tested using the same PMMA stabilized 2D AgNP arrays after removing the sucrose solution and rinsing with DI H_2O. Multiple runs with the same PMMA stabilized 2D AgNP arrays were able to be performed. Once each run was done, the UV-Vis spectra of the PMMA stabilized 2D AgNP arrays were tested. The LSPR peak of the PMMA stabilized 2D AgNP arrays went back to its original position after cleaning. This implies that the PMMA stabilized 2D AgNP arrays is re-usable and can be stored in air or liquid environment without losing their LSPR properties.

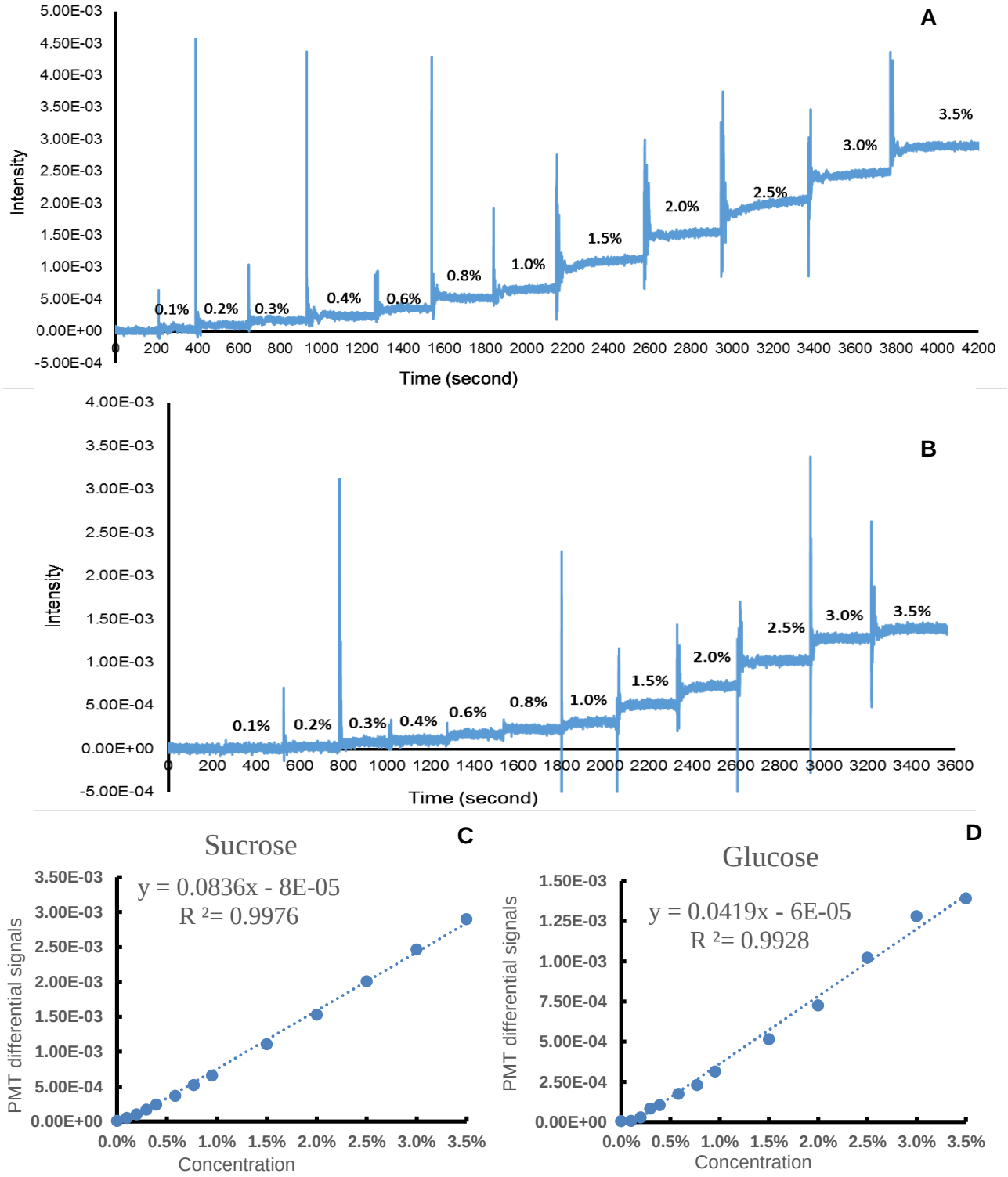

Figure 2. 5 PMMA stabilized 2D AgNP array response to sucrose **(A)** and glucose **(B)** at different concentrations. Each spike is caused by addition of sucrose/glucose. Linear relationship between the differential signals and the concentration changes of sucrose**(C)** and glucose **(D).** In images C & D, X-axis is saccharide concentration, Y-axis is PMT differential signals.

566

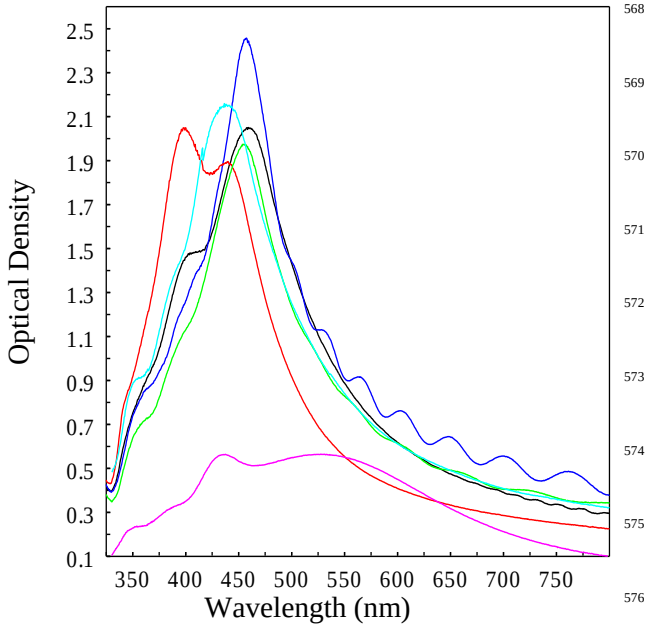

Figure 2. 6 UV-Vis spectra of 2D AgNP-polymer nanocomposite films. Blue-12.5% PBMA on PMMA stabilized 2D AgNP array**,** Black-12.5% PMMA on PMMA stabilized 2D AgNP array, Green-12.5% PVAC on PMMA stabilized 2D AgNP array**,** Red-PMMA stabilized 2D AgNP array in air, Teal-2D AgNP array in H_2O, Pink-AgNP suspension in water.

To further explore the sensing capabilities of these PMMA stabilized 2D AgNP arrays, a responsive layer of a different polymer (~1.5 μm thick) was spin coated on the PMMA stabilized 2D AgNP arrays to make a polymer nanocomposite for VOC sensing. An illustration of such films is shown in Fig. 2.2 D. This system is not only aiming to achieve the sharpest plasmon resonance by providing a higher refractive index environment surrounding AgNP (all polymers used here have higher refractive index than water) but also utilizing the phenomenon that the responsive polymer film will shrink or swell upon exposure to solvent vapor. In general there are two approaches to achieve higher sensitivity of a LSPR sensor: 1. generating the sharpest plasmon resonance, 2. achieving the largest spectral shift of the resonance per unit change of the refractive index. Sherry et al described a figure of merit (FOM) by taking the ratio of these two factors to define the sensitivity of any given sensor allowing easier comparison of different sensors.[16] The LSPR system described here takes advantage of an extremely sharp

plasmon resonance by embedding AgNP within a higher refractive index polymer together with differential optical measurements resulting in real-time VOC sensing with kinetic recording possibility. To achieve this goal, 10-12.5% polymer solutions were spin-coated on top of PMMA stabilized 2D AgNP arrays to fabricate the 2DSPNF. UV-Vis spectra were used to examine the 2DSPNF responses to VOC in real time. Fig. 2.6 is a summary of 2D AgNP array UV-Vis spectra when stabilized with PMMA and deposited with different responsive polymer layers. For example, PBMA coated 2D AgNP arrays (Fig 2.5 blue curve) showed a higher OD with smaller FWHM compared to naked 2D AgNP arrays in water (Fig. 2.6, teal curve). The fringe patterns on 2DSNPF were caused by light propagating between polymer films and interference.

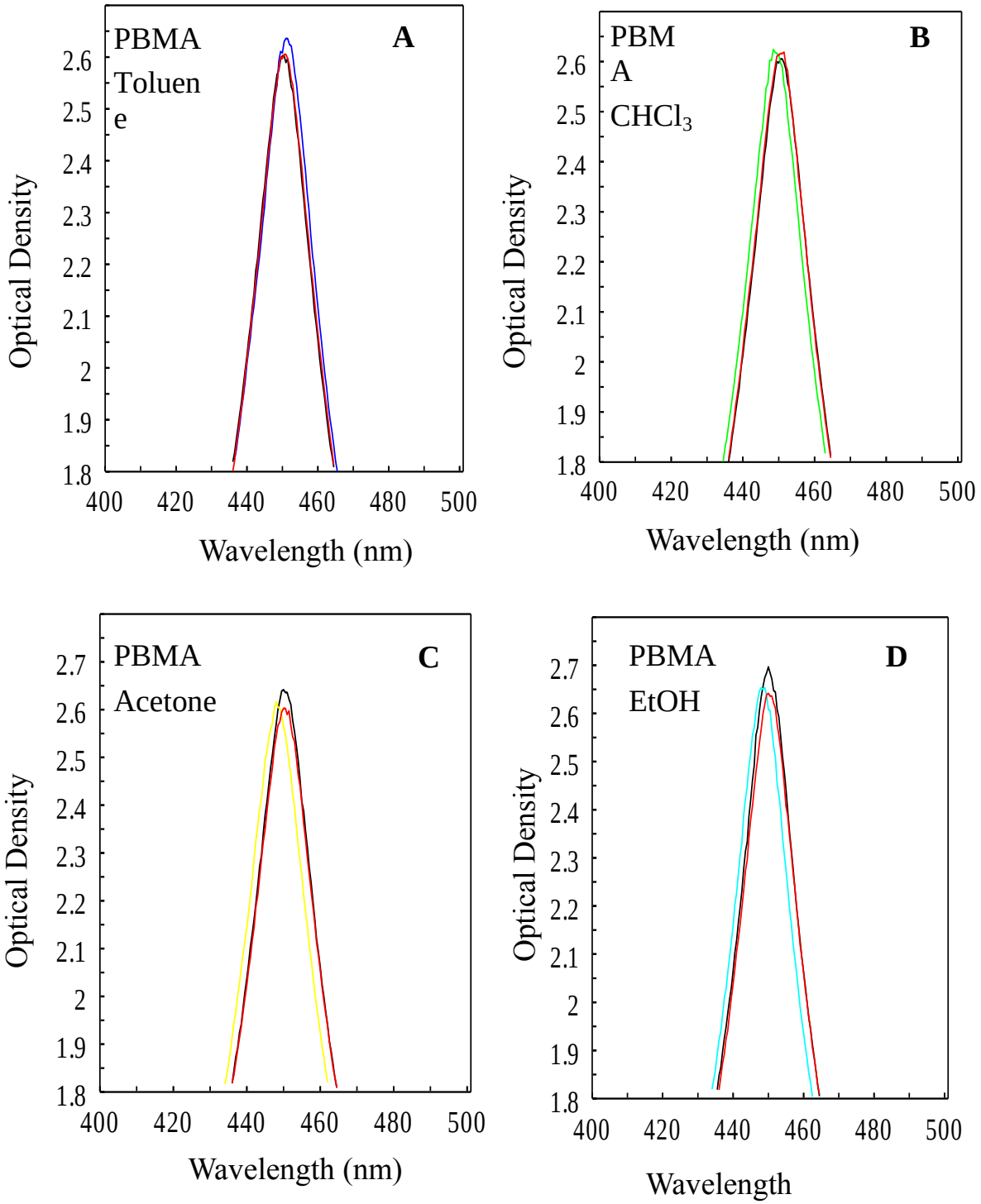

Figure 2. 7 UV-Vis spectra of freshly made PBMA 2DSNPF before exposing to VOC vapors (Black), while exposing (Blue, Yellow, Green, Teal), and after exposing (Red). **(A)**-Toluene vapor; **(B)**-Chloroform vapor; **(C)**-Acetone vapor; **(D)**-EtOH vapor. X-axis: Wavelength (nm), Y-axis: Optical density.

599

Figure 2.7 is a summary of UV-Vis spectra of PBMA 2DSPNF responses to VOC vapors including toluene, chloroform, acetone and ethanol. Experiments were carried out in ambient environment at room temperature by having a PBMA 2DSPNF glass slide standing at one side of the cuvette while 5 μl of each solvent was dropped at the opposite corner of the cuvette. UV-Vis spectra were collected immediately after exposing PBMA 2DSPNF to VOC vapors. Fig 2.7 showed that toluene is causing the LSPR peak shift to the red spectral range, while chloroform, acetone, and ethanol are causing the LSPR peak blue shifted. This might be explained by 1: Upon interacting with toluene, the PBMA film swelled slightly, leading to a greater distance between AgNP, thus causing a red shift. Upon interacting with chloroform, acetone, and ethanol, the PBMA film slightly contracted, leading to less distance between AgNP, thus introducing a blue shift. 2: Once VOC vapors diffuse into the polymer film, the local refractive index will change, causing the LSPR peak shift. There might be a competitive or synergistic effect between these two factors depending on which polymer is used and which VOC vapor is being sensed here. Though the LSPR peak shifts can be observed in UV-Vis spectra, the exact magnitude of the shift was difficult to determine due to its small difference. A fitting procedure can be used to provide better resolution. Table 2.2 summarized the PBMA 2DSPNF LSPR peak shift upon exposing to VOC vapors analyzed by peak fitting in Origin 8 (OriginLab Corporation). As an example, as fabricated PBMA 2DSPNF LSPR peak is at 450.3 ± 0.5 nm, when exposed to ethanol vapor LSPR peak shifted to 446 ± 1 nm. LSPR peak moves back to 450.4 ± 0.5 nm upon removal of VOC. It was concluded that the PBMA 2DSPNF exhibits reversible response upon the removable of VOC and

the LSPR peak shift can be quantified using fitting procedure in Origin 8. However, the LSPR peak shift is in still in small ranges (less than 4.6 nm change), and cannot be monitored in real-time. So, we utilized our differential optical transmission method here to obtain real-time, more sensitive measurement. UV-Vis spectra of the PBMA 2DSPNF films in ambient air was first measured in order to determine the position of the LSPR peak and determine the correct position of the monochromator for the differential measurements, so that the two wavelengths excite at both sides of the resonance peak. Upon exposure PBMA 2DSNPF to VOC vapors, the intensity at each wavelength was then measured by an individual PMT and the lock-in amplifier displaying the difference between the two signals.[7]

	Toluene	$CHCl_3$	Acetone	EtOH
Before	450.5 ±0.6	450.7 ±0.6	450.4 ±0.5	450.3 ±0.5
During	451.5 ±0.5	448.6 ±0.5	447.8 ±0.5	446.0 ±1.0
After	450.7 ±0.6	450.3 ±0.6	450.5 ±0.6	450.4 ±0.5
Δλ(Before-During)	~+0.9 ±0.7	~-2.1 ±0.7	~-2.7 ±0.7	~-4.2 ±1.1

Table 2. 2 Summary of PBMA 2DSNPF LSPR peak shifts to VOC vapors. (Unit: nm. Data was analyzed using Origin 8)

As shown in Fig. 2.8 A, the PBMA 2DSPNF exhibited a reversible response upon the removal of VOC vapors. Toluene vapor caused positive PMT differential signal while $CHCl_3$, acetone, and ethanol caused negative differential signal. This behavior correlates with that observed using UV-Vis spectrometer as shown in Fig. 2.7. Positive PMT differential signals imply red shifts while negative PMT differential signals imply blue shifts. The PMT differential signals can be used to indicate how much LSPR peak has shifted. As shown in Table 2.2, the LSPR peak shift caused by toluene vapor is less than

that of $CHCl_3$ vapor, followed by acetone vapor then ethanol vapor which caused the largest shift. The same behaviour was observed using the differential optical transmission method. The differential optical transmission method not only provides better accuracy, but also provides the possibility for real time kinetic studies. The LSPR peak shifts measured by UV-Vis spectrometer were plotted versus the PMT differential signals as shown in Fig. 2.9. The linear trend is maintained, however with 0.94 regression value. The low regression value might be explained by the limitation of conventional UV-Vis spectrometer when interrogating this system. As a conventional UV-Vis spectrometer acquires one spectrum at a time, the delay between measurements may be long enough that the VOC vapors has started to diffuse out, or too short so that the largest LSPR peak shift has not yet been achieved. In other words, UV-Vis spectra measurements may not reflect the maximum LSPR shifts due to the acquisition time delay thus affecting the linear relationship.

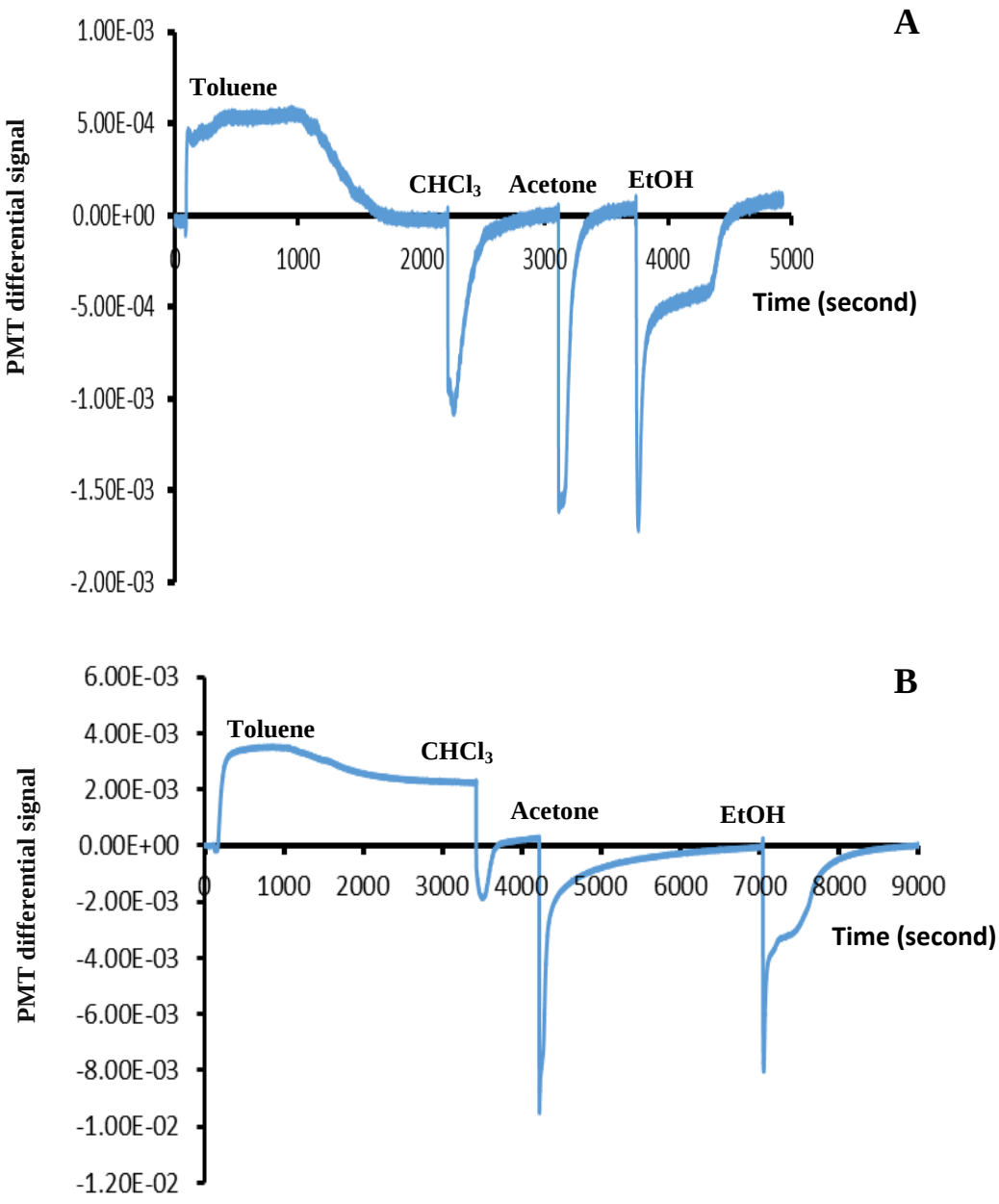

Figure 2. 8 PBMA **(A)** and PVAC **(B)** 2DSNPF response to VOC vapor. X-axis: Time (second). Y-axis: PMT differential signals. Each spike is caused by suddenly exposing 2DSNPF to VOC vapors.

655

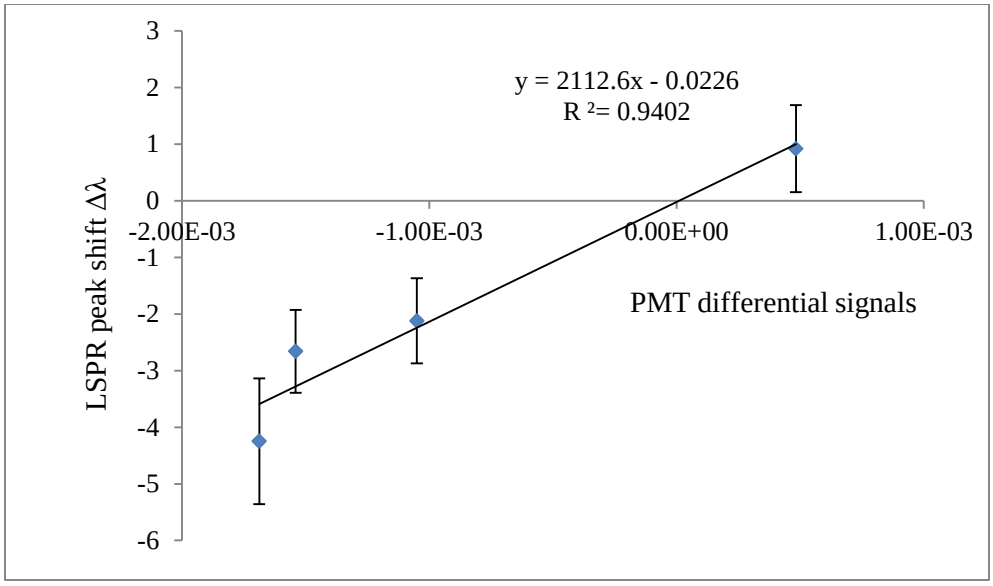

Figure 2. 9 PBMA 2DSNPF responses upon exposing to VOC vapors. LSPR peak shifts measured using UV-Vis spectroscopy versus PMT differential signals.

Fig. 2.8 A shows that it took around 1500 seconds for toluene to diffuse out of the PBMA film, $CHCl_3$ needed around 750 seconds, acetone needed around 350 seconds and ethanol needed around 750 seconds. After all VOC vapors left the PBMA 2DSPNF, the PBMA 2DSPNF can be re-used and giving reversible response. Toluene interacts with the PBMA film for around 1000 seconds, and then starts to diffuse out of the film while $CHCl_3$ and acetone showed shorter interaction time but longer diffusion time, meanwhile ethanol showed a two-step process as shown by the two plateaus of the ethanol curve. The relaxation time and the signal intensity are the two factors that could be used to predict the VOC's sensing thereby providing better accuracy and more information compared to traditional UV-Vis spectrometry.

In order to compare the differences between responsive polymer films, PVAC was spin-coated on PMMA stabilized 2D AgNP array and serve as a VOC sensing platform. The responses of PVAC 2DSNPF to VOC vapors were shown in Fig. 2.8 B as a comparison here to broaden the application of PMMA stabilized 2D AgNP array. It is shown in Fig 2. 8 B that toluene was taking almost 2000 seconds to diffuse out of the PVAC film. Equilibrium was reached around 2500 seconds but the PMT differential signal was still positive. This may imply PVAC 2DSNPF may not be a good sensor for toluene, as it was taking too long to go back to its original state as evident by reaching the original LSPR peak position. Conversely, $CHCl_3$ can bring LSPR peak back to its original position in a relatively short time. $CHCl_3$ took 1000 seconds to diffuse out, acetone took 2500 seconds and ethanol took 2000 seconds. Acetone is causing higher PMT differential signal than ethanol and both $CHCl_3$ and toluene. The diffusion times and PMT differential signals highly depends on the polymer which was chosen and could be used to distinguish different VOC vapors for polymer 2DSNPF.

Polymer	Polydiallyldimethyl ammonium chloride	Poly(4-vinylpyridine)	Polyvinyl acetate	Poly(methyl methacrylate)	Poly(butyl methacrylate)
Structure	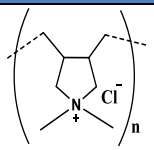	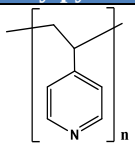	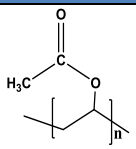	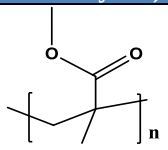	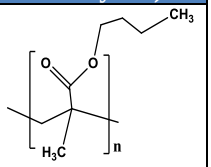
Refractive Index	/	1.549	1.4665	1.4893-1.4899	1.48

Table 2. 3 Summary of polymers used in fabricating the polymer 2DSNPF.

The structural differences between PBMA and PVAC 2DSNPF was tested under AFM imaging to compare their morphologies. 0.5% PDDA aqueous solution was used as

an adhesive polymer instead of PVP ethanol solution. PVP strongly interacts with AgNP and glass slides[17], while PDDA loosely interact with AgNP and glass slides thus allows us to peel off the polymer 2DSNPF and utilize AFM to measure the silver side of the 2DSNPF.[18] Polymer structures and their refractive indices are shown in Table 2.3. PMMA stabilized 2D AgNP array AFM images were shown in Fig. 2.10 A&B, AgNP were closely packed on PVP/PDDA modified glass slides. The average height of the AgNP after PMMA coating (Fig.2.10 B) was 78.36 nm, compared to the original height of AgNP used in this work (92.23 nm), suggesting there is a 13 nm PMMA polymer film. This PMMA film is stabilizing AgNP by offering crater-like structures surrounding the AgNP.[13] Compared with PVAC 2DSNPF (Fig. 2.10 C&D), AgNP in PBMA 2DSNPF (Fig. 2.10 E&F) are more embedded in the responsive polymer film. This may be caused by the intercalation of PMMA into the PBMA layer to a higher degree than PVAC as is expected based on their structural similarity (Table 2.3). AgNP height profile in Fig 2.10 C&D is around 40 nm while AgNP height profile in Fig 2.10 E&F is around 5 nm. The structure difference of PBMA and PVAC is also a key factor for how the responsive film may interact with VOC vapors. According to Fick's laws, the diffusion of VOC vapor is proportional to the negative gradient of vapor concentrations. It goes from regions of higher concentration to regions of lower concentration. [17] When VOC vapor interacts with 2DSNPF, the diffusion also depends on the relative affinity of the vapor phase molecules to the films versus the vapor phase. For example, a polar molecule will have a larger affinity for a polar film while a non-polar molecule will have a larger affinity for a non-polar film. [18] The same rules observed for other separation methods, such as gas

chromatography, also apply for the film coatings of the vapor sensors. In addition, analyte molecules with lower vapor pressure will generally favor the film, or the condensed phase. Many researchers model the response of the sensor as a function of the vapor phase concentration according to the Langmuir adsorption isotherm model.[19] The ambient air vapor sensing using our 2DSNPF utilizes the association and dissociation of vapor molecules with polymer film and the LSPR peak's linear response to local refractive index changes. By using different responsive polymer and analyzing data with chemometric methods, a VOC sensing library could be built to provide higher specificity.

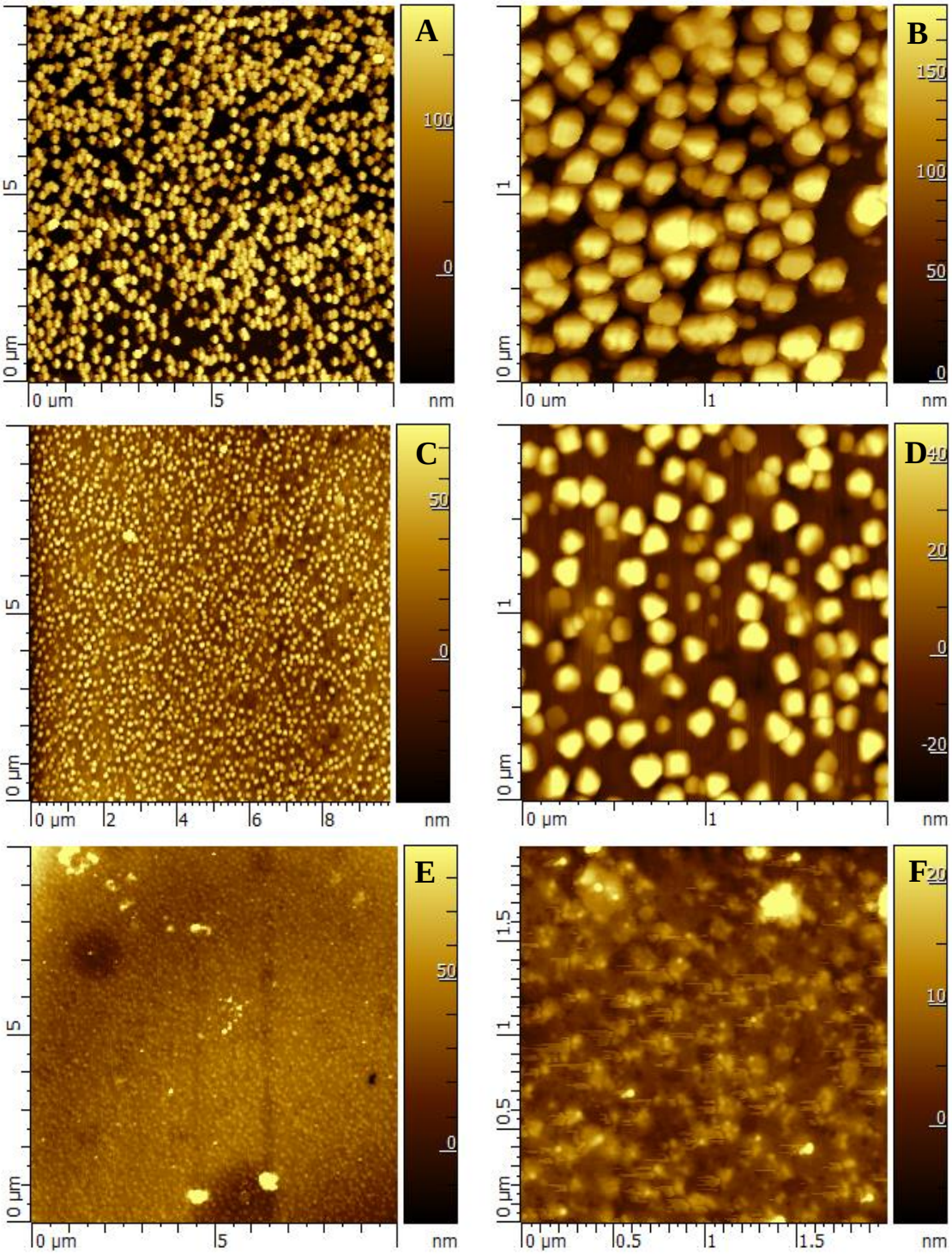

Figure 2. 10. **A&B:** AFM images of 0.05 % PMMA stabilized 2D AgNP array. **C&D:** AFM images of 12.5 % PVAC 2DSNPF. **E&F:** AFM images of 12.5 % PBMA 2DSNPF. Images C, D, E, F were taken on the silver side of the 2DSNPF by peeling off the fabricated film from glass slides.

716

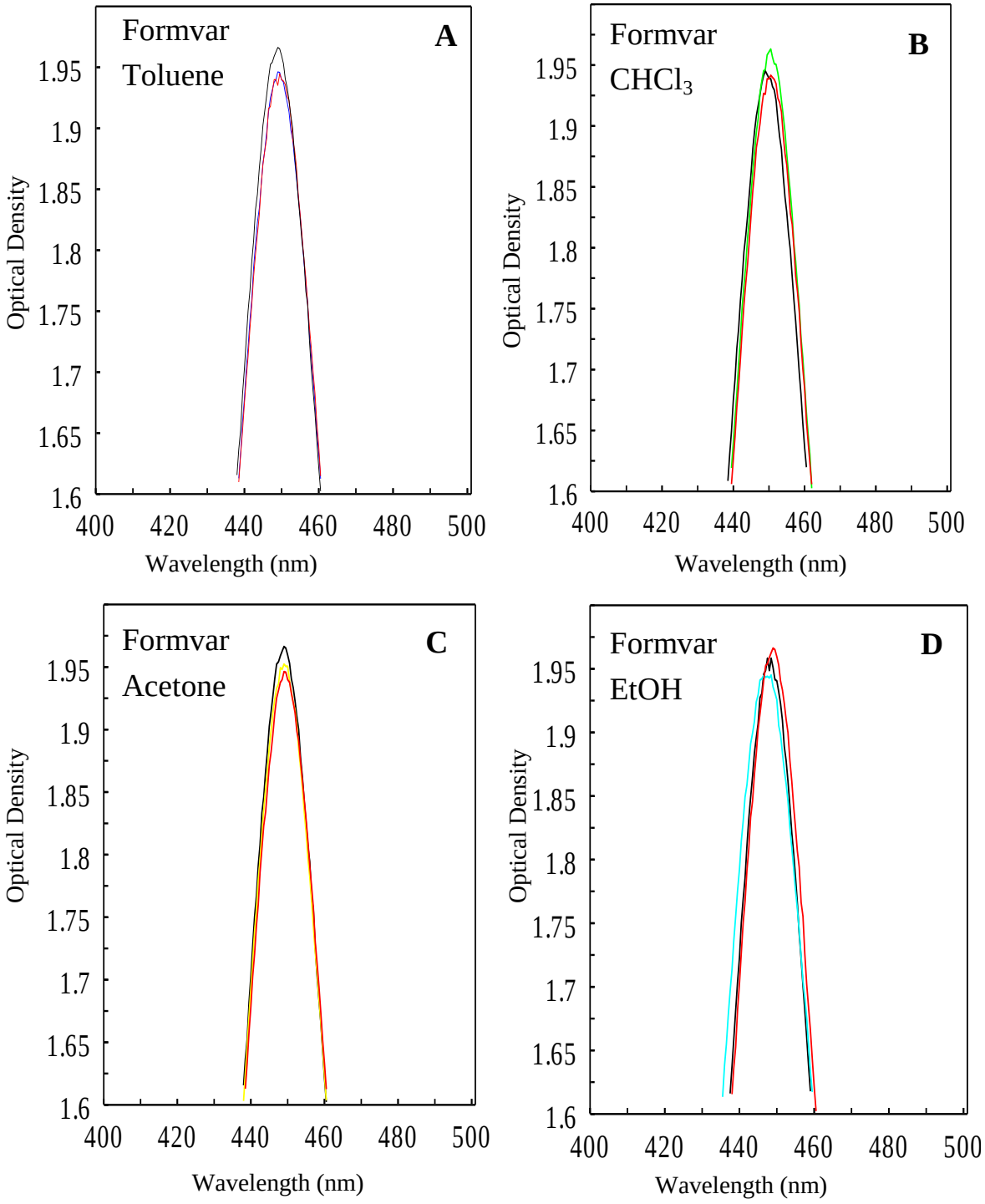

Figure 2. 11 UV-Vis Spectra of Formvar 2DSNPF before exposing to VOC vapors (Black), while exposing (Blue, Yellow, Green, Teal), and after exposing (Red). **(A)**-Toluene vapor; **(B)**-Chloroform vapor; **(C)**-Acetone vapor; **(D)**-EtOH vapor. X-axis: Wavelength (nm), Y-axis: Optical density

717

Different responsive polymers (co-polymer, block polymer or polymer mixture) can be spin coated on PMMA stabilized 2D AgNP array to build a polymer PMMA stabilized 2DSNPF library. Formvar 2DSNPF response to VOC was shown in Fig. 2.10. As a mixture of several polymers (PVA, formaldehyde, PVAC), formvar is very flexible, water-insoluble, and resistant to abrasion.[19]. Toluene and acetone both caused LSPR peak red shift, while $CHCl_3$ and ethanol both caused LSPR peak blue shift (Fig. 2.11). This may be explained by the fact that formvar is a polymer mixture; its response to VOC vapors may vary from other homopolymers. The morphology of formvar film was measured using AFM as shown in Fig. 2.12 A-D. Fig.2.12 C shows the height profile of AgNP in formvar film is 5.47 nm, and the distance between AgNP is approximately 55 nm. The LSPR peak changes of formvar 2DSNPF are smaller compared to both PBMA and PVAC. Fig. 2.12 D-F shows the morphology of the polymer sides of formvar/PBMA/PVAC 2DSNPF which implies the roughness of polymer film is less than 2 nm. The smoothness of responsive polymer layer guarantees the homogeneous diffusion of vapor molecular into the polymer film.

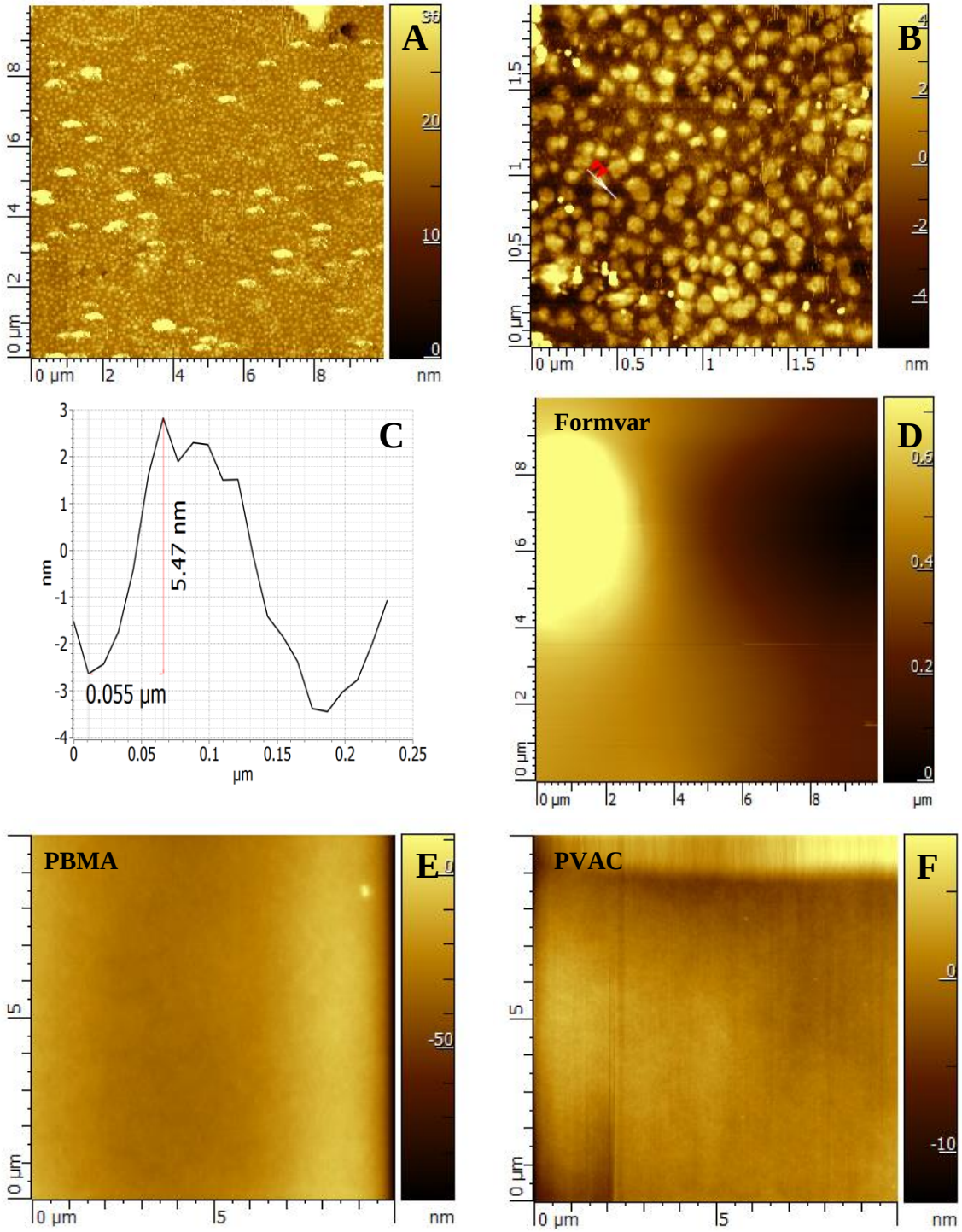

Figure 2. 12. (A), (B) &(C) are AFM images of 3.3 % formvar 2DSNPF. **(C)** is the height profile of formvar 2DSNPF in Image B. **(D), (E) & (F)** are AFM images of 2DSNPF on polymer side. **(D)**-formvar side, **(E)**-PBMA side, **(F)**-PVAC side.

738

2.5 Conclusion

In conclusion, we have stabilized 2D AgNP array with PMMA film between AgNP which maintains the sharp 2D AgNP LSPR peak upon drying and re-wetting. The PMMA stabilized 2D AgNP array gives linear response to bulk refractive index changes and can be re-used after simple cleaning with DI water. [20] Responsive polymer films can be spin-coated on PMMA stabilized 2D AgNP array to fabricate 2DSNPF. These 2DSNPF produce sharper LSPR peaks and can also be used to differentiate between various VOC vapors. By utilizing the differential optical transmission method developed in our lab, the responses of polymer 2DSNPF upon exposing to VOC can be monitored by both diffusion time and PMT differential signals. A linear relationship between PMT differential signals and LSPR peak shifted measured by UV-Vis spectroscopy was maintained with 0.94 regression value. Different responsive polymer (can also be co-polymer, block polymer, polymer mixture) can be spin-coated on the PMMA stabilized 2D AgNP array giving distinguishable different signal when exposing to the same vapor.

2.6 Acknowledgments

I would like to take this opportunity to thank Dr. Daniel Willett in helping revive our differential optical transmission instrument, Dr Yi Jin in advising, Anthony Childress in modifying the Labview program for us to use the lock-in amplifier and Tatiana Estrada-Mendoza in synthesizing AgNP.

2.7 References

[1] M. Faraday, The Bakerian Lecture: Experimental Relations of Gold (and Other Metals) to Light, Philosophical Transactions of the Royal Society of London, 147(1857) 145-81.

[2] H. Nguyen, J. Park, S. Kang, M. Kim, Surface Plasmon Resonance: A Versatile Technique for Biosensor Applications, Sensors, 15(2015) 10481.

[3] J. Zheng, P.E. Constantinou, C. Micheel, A.P. Alivisatos, R.A. Kiehl, N.C. Seeman, Two-Dimensional Nanoparticle Arrays Show the Organizational Power of Robust DNA Motifs, Nano Letters, 6(2006) 1502-4.

[4] U. Kreibig, M. Vollmer, Optical Properties of Metal Clusters: Springer-Verlag Berlin Heidelberg; 1995.

[5] D.D. Evanoff, R.L. White, G. Chumanov, Measuring the Distance Dependence of the Local Electromagnetic Field from Silver Nanoparticles, The Journal of Physical Chemistry B, 108(2004) 1522-4.

[6] K.M. Mayer, J.H. Hafner, Localized Surface Plasmon Resonance Sensors, Chemical Reviews, 111(2011) 3828-57.

[7] D. Willett, G. Chumanov, LSPR Sensor Combining Sharp Resonance and Differential Optical Measurements, Plasmonics, 9(2014) 1391-6.

[8] D. Willett, G. Chumanov, One-step synthesis and applications of highly concentrated silver nanoparticles with an ultra-thin silica shell, RSC Advances, 6(2016) 108136-45.

[9] M.K. Kinnan, S. Kachan, C.K. Simmons, G. Chumanov, Plasmon Coupling in Two-Dimensional Arrays of Silver Nanoparticles: I. Effect of the Dielectric Medium, The Journal of Physical Chemistry C, 113(2009) 7079-84.

[10] T.R. Jensen, M.L. Duval, K.L. Kelly, A.A. Lazarides, G.C. Schatz, R.P. Van Duyne, Nanosphere Lithography: Effect of the External Dielectric Medium on the Surface Plasmon Resonance Spectrum of a Periodic Array of Silver Nanoparticles, The Journal of Physical Chemistry B, 103(1999) 9846-53.

[11] G. Mie, Beitr ä ge zur Optik tr ü ber Medien, speziell kolloidaler Metall ö sungen, Annalen der Physik, 330(1908) 377-445.

[12] P.B. Johnson, R.W. Christy, Optical Constants of the Noble Metals, Physical Review B, 6(1972) 4370-9.

[13] L. Hu, A. Pfirman, G. Chumanov, Stabilization of 2D assemblies of silver nanoparticles by spin-coating polymers, Applied Surface Science, 357, Part B(2015) 1587-92.

[14] X. Fan, I.M. White, S.I. Shopova, H. Zhu, J.D. Suter, Y. Sun, Sensitive optical biosensors for unlabeled targets: A review, Analytica Chimica Acta, 620(2008) 8-26.

[15] D. Monz ó n-Hern á ndez, J. Villatoro, High-resolution refractive index sensing by means of a multiple-peak surface plasmon resonance optical fiber sensor, Sensors and Actuators B: Chemical, 115(2006) 227-31.

[16] L.J. Sherry, S.H. Chang, G.C. Schatz, R.P. Van Duyne, B.J. Wiley, Y. Xia, Localized Surface Plasmon Resonance Spectroscopy of Single Silver Nanocubes, Nano Lett, 5(2005) 2034-8.

804 [17] S. Malynych, I. Luzinov, G. Chumanov, Poly(Vinyl Pyridine) as a Universal Surface
805 Modifier for Immobilization of Nanoparticles, The Journal of Physical Chemistry B,
806 106(2002) 1280-5.
807 [18] M. Stadermann, S.H. Baxamusa, C. Aracne-Ruddle, M. Chea, S. Li, K. Youngblood,
808 et al., Fabrication of Large-area Free-standing Ultrathin Polymer Films, Journal of
809 Visualized Experiments : JoVE, (2015) 52832.
810 [19] A. F. Fitzhugh, E. Lavin, G. O. Morrison, The Manufacture, Properties, and Uses of
811 Polyvinyl Formal1953.
812 [20] S. Peiris, J. McMurtrie, H.-Y. Zhu, Metal nanoparticle photocatalysts: emerging
813 processes for green organic synthesis, Catalysis Science & Technology, 6(2016) 320-38.
814
815

CHAPTER THREE

Extrapolating the Concept of Protein Corona for the Understanding of Protein Nanoparticle Interaction

3.1 Introduction

According to the ASTM, nanoparticles are classified as those particles ranging from 1 to 100 nanometers in two or three dimensions. Nanoparticle production has greatly increased due to the rising manufacture of nanoparticle-containing materials as well as new found applications for them.[1] Over the past few decades, nanotechnology has revolutionized the electronics, imaging, sensing, medical and semiconducting landscape due to the unique physical and chemical properties. As a result, it is inevitable that humans, animals, and plants will be exposed to nanoparticles (NP), this is of concern since their high surface area and reactivity may exhibit adverse effects once they go into biological systems. There has been an increase of adverse reactions to medical drugs which is primarily related to long treatment periods that can lead to sensitization and potential hypersensitivity.[2, 3] This may be particularly true for nanomedicine, as the NP may act as an immune adjuvant and potentiate hypersensitivity reactions. The safe usage of NPs is dependent upon their physiochemical parameters such as size, morphology, chemical composition, surface modification, charge, etc. Recent studies [4-6] have revealed that oral, pulmonary, and intradermal administration of silver, single-

walled carbon nanotubes (SWCNTs) and silica NP could induce organ toxicity, inflammatory responses, atopic dermatitis-like skin lesions, etc. The fate of nanoparticles in biological systems can be influenced by the physical interaction with proteins in the host system, at the cellular, tissue and whole organism level. The high surface to volume ratio of nanoparticles will result in high reactivity and catalytic activity, which can be of potential danger both medically and environmentally.[7, 8]

In order to study the fate of NP when they go into biological fluid, NP interaction with proteins in the biosystem must be understood. The actual distribution and transfer mechanism of nanoparticles in cells and tissues has not been clearly illustrated yet. The biological effect of nanoparticles is caused by their chances of passing through cell membranes in organisms. The cytotoxicity of nanoparticles can be attributed to two different processes, NP physical adsorption onto cell membranes/walls and the release of ions in the intracellular space. This subsequently triggers the production of reactive oxygen species (ROS). Silver nanoparticles (AgNP) and gold nanoparticles (AuNP) are the major classes of metal nanoparticles that are of interest. These two possess unique size-dependent optical, electrical properties that are attractive for biological and medical applications.[9, 10] Exposure to AgNP has been associated with “inflammatory, oxidative, genotoxic and cytotoxic consequences”. AgNP primarily accumulate in the liver,[11] but have also shown toxic effects in the brain.[12] AuNP have been used for nanomedicines in imaging, diagnostics and therapy aspects, etc. [13] The toxicity of AuNP is still under debating, as AuNP have been described toxic and non-toxic by

different researchers. [14-16] However, the surface modification as well as sizes differences of AuNP, both have been shown to have effects on AuNP toxicity.[17-19] The success of nanotechnology, particularly in medicine, depends upon the safety of nanomaterials. When NP are exposed to biological fluid, proteins can bind to the surface of the nanoparticle to form a “protein corona”, which affects how nanoparticles are internalized by cells and cleared from the body. Since human plasma contains nearly 2000 proteins, understanding how the corona forms and transports remains a challenge due to the type, size and surface properties of the nanoparticles.[17] The long-lived protein ("hard") corona can be expressed as a durable, stabilizing coating of the bare surface of nanoparticle monomers, or it may be reflected in different subpopulations of particles assemblies, each presenting a durable protein coating.[18] Several kinds of proteins: actin, tubulin, complement component 3, apolipoprotein, albumin and fibrinogen that are different in composition, morphology, and amphiphilicity are utilized as a protein library. These proteins are chosen because of their abundance shown in several proteomic studies that identified corona proteins following NP exposure to blood and serum. [19] AgNP and AuNP are chosen here to serve as a NP library as they are among the top engineered nanomaterials in consumer products. [10, 20]

Here we studied two aspects in the health and safety implications of protein-NP corona to look deeper into their biophysical properties: (1) protein conformational changes and crowding resulting from their interactions with the nanoparticle; (2) evolution of the protein corona over time and how the ions released from NP impact

toxicity. This work is based upon our hypotheses that a) the proteins in the protein-NP corona adopt compromised but predictable conformation changes to accommodate the NP core of given physicochemical properties. There is a rapid exchange between proteins bound with nanoparticles' surface and free proteins.[21, 22] b) membrane receptors target specifically the proteins that are an integral component of the dynamic protein corona, not the NP. By study the biophysical properties of the protein-NP corona, we may predict the transformation and immune reactivity of nanomaterials.

3.2 Background

Nanoparticles can be synthesized using pyrolysis, radiation chemistry, hydrothermal conversion, sol-gel process, etc. Surface coated nanoparticles can increase the polarity, aqueous solubility and prevent the aggregation. In serum or on the cell surface, highly charged coatings promote the non-specific binding. Nanoparticles can be linked to biological molecules which can act as address tags to help direct the nanoparticles to specific organelles within the cell. An inventory of nanotechnology-based consumer products can be found in the references.[19] AgNP and AuNP have been both widely used in consumer products, including cosmetics, food packaging, toothpaste, health supplement, clothing, etc. [23, 24] AgNP and AuNP have been chosen to serve as a NP library, while several protein (actin, tubulin, complement component 3, apolipoprotein, albumin and fibrinogen) in serum or blood serve as a protein library that allows us to study the NP-protein interactions using different NP and different proteins.

Cytoskeleton is the cellular scaffolding or skeleton contained within a cell's cytoplasm. Eukaryotic cells contain three main kinds of cytoskeletal filaments: microfilaments (actin filaments), intermediate filaments, and microtubules. The cytoskeleton provides the cell with structure and shape and also plays important roles in both intracellular transport (the movement of vesicles and organelles, for example) and cellular division. Microfilaments (actin filaments) are composed of linear polymers of actin subunits. Microfilaments induce force by elongation at one end of the filament coupled with shrinkage at the other causing net movement of the intervening strand and also act as tracks for the movement of myosin molecules that attach to the microfilament and walk along them. Microtubules are the polymer form of alpha and beta tubulin that help maintain cell shapes, rigidity, motility and cell signaling.[25]

Complement component 3 (C3) plays a central role in body's complement system that helps kill disease-causing bacterial and virus.[26] Complement system is part of the immune system that can protect people from diseases. C3 can turn on the complement system when foreign invaders (bacterial, virus and NP) present in human body.[27] Researchers have shown that people who are deficiency of C3 are susceptible to bacterial infection due to immune system malfunction. [28, 29]

Apolipoproteins play a key role in lipid metabolism due to their lipid-binding properties. Apolipoproteins can bind to oil-soluble substances like fat and cholesterol to form lipoproteins. Lipoproteins are biochemical assembles contain both lipids and

proteins that allow fat to move through the biogical fluid inside and outside cell. [30] The transportation of apolipoproteins can be finished by lymphatic and circulatory systems. Apolipoproteins serve as enzyme cofactors, receptor ligands and lipid transfer carriers that regulate the metabolism of lipoproteins. [31, 32] Apolipoproteins contains amphipathic groups that allow them to surround the lipids thus making the lipoproteins soluble in blood and lymph.[33, 34]

Albumin constitutes about half of the blood serum protein. It has been used in clinical medicine. [35, 36] Serum albumin is the most prevalent protein in blood plasma, Human serum albumin can be clinically used to treat burns, shock and blood loss. [37] Albumin is soluble and can transport hormones (most fat soluble hormones), fatty acids, and drugs in blood serum,[38] as well as helps maintain the cell osmotic pressure. [39]

Fibrinogen is a plasma glycoprotein that is converted by thrombin into fibrin during blood clot formation. [40] During normal blood coagulation, thrombin will convert the soluble fibrinogen into insoluble fibrin strands then cross-linked to form a blood clot. [41, 42] Deficiency of fibrinogen can lead either bleeding or thromboembolic complications. [43, 44]

3.3 Materials and Instrumentation

3.3.1 Materials

Citrate-coated AgNP (Biopure, 30 nm in diameter, 1 mg/mL; equivalent to 11.1 nM per particle) was purchased from NanoComposix (San Diego, CA) and stored at 4 ℃. Cardiac actin (bovine heart muscle, M.W.: 43 kDa) and tubulin (bovine brain, M.W.: 110 kDa) were purchased from Cytoskeleton.Inc (Denver, CO). The stock actin and tubulin solutions were both stored at -20 ℃.The actin was reconstituted to 46.5 μM (2 mg/mL) with distilled water to form a stock solution in the buffer of 5 mM Tris-HCl, pH 8.0, 0.2 mM $CaCl_2$, supplemented with 0.2 mM ATP, 5% (w/v) sucrose and 1% (w/v) dextran. The tubulin was dissolved to 10 μM (1.1 mg/mL) by adding 227 μL GTB (General Tubulin Buffer: 80 mM PIPES, pH 6.9, 2 mM $MgCl_2$, and 0.5 mM EGTA). Deionized water with a nominal resistivity of 18 MΩ·cm was obtained from a Millipore Milli-Q water purification system. Citrated-coated AgNP stock suspension (Biopure, 20 nm and 110 nm in diameter, 1 mg/mL) was purchased from NanoComposix (San Diego, CA) and stored at 4^{o}C. Complement C3 human protein (1.2 mg/mL in PBS pH 7.2) was purchased from Calbiochem (Billerica, MA), stored at -70^{o}C, and thawed to room temperature before use. Positive coated AuNP stock suspension (1.5 mg/ml) was purchased from Vivenano (Canada), and stored at 4^{o}C. Texa Red congulate-Albumin from bovine serum (5 mg), Alexa Fluor 488 conguate-Fibrinogen from bovine plasma (5 mg) was purchased from Invitrogen (Eugene, OR) and diluted with PBS buffer at pH 7.4 to 0.952 mg/ml and 1.699 mg/ml respectively, then stored at -20^{o}C, and thawed to room temperature before use. Albumin from bovine serum powder, fibrinogen from bovine plasma powder was purchased from Sigma (St Louis, MO) and dilute to 6.7 mg/ml with PBS buffer at pH 7.4 as the stock solutions.

3.3.2 Instrumentation

UV-Vis Spectrophotometry

Surface Plasmon Resonance (SPR) is a physical phenomenon associated with the optical properties of metallic NP and their sensitivity to surrounding environment.[45] The SPR peak is sensitive to the NP size, coating, and the surrounding medium. Any species adsorbed to the nanoparticle surface will be manifested by a color change (shift in the SPR peak position) proportional to the magnitude of the change in the refractive index near the nanoparticle surface. The wavelength and width of the peak absorbance and the effect of secondary resonances yield a unique spectral fingerprint for specific size and shape nanopaticles.[45] Deionized water (18 MΩ cm) was used to dilute stock proteins and AgNP to make mixtures of actin/AgNP (0.1 nM) at molar ratios of 50, 100, 150, 250, 500, 1000 and 1500; tubulin/AgNP at molar ratios of 20,120,200,400,800 and 1500. The cytoskeletal protein-AgNP solutions were incubated for 2 h at 4℃ before centrifugation at 8,669 g for 10 min. The absorbance spectra of the supernatants were then measured using 1 cm path length quartz cuvettes and compared with the surface plasmon resonance spectrum of the AgNP using a UV-Vis spectrophotometer (Cary 300 Bio, Varian). The observed spectral shifts were attributed to the formation of protein corona (which resulted in an increased local dielectric constant) as well as NP aggregation. To compare the binding of complement C3 with AgNP of 20 nm and 110 nm, deionized water was used to dilute the stock complement C3. Complement C3 was then mixed with 20 nm AgNP (2 mg/L) to obtain protein: AgNP molar ratios of 1.38, 6.89, 27.6 and 55.2, and with 110 nm AgNP (0.01 mg/mL) to obtain protein/NP molar

ratios of 183, 458, 2288, and 4577, respectively. The protein-AgNP mixtures were incubated for 30 min prior to their UV-Vis measurements using quartz cuvettes.

Hydrodynamic sizes and zeta potentials

Colloidal particles' sizes are usually measured by light scattering and zeta potentials are determined from electrophoretic mobilities.[46] The average hydrodynamic sizes and surface charges of the actin (200 nM), tubulin (50 nM), AgNP (0.5 nM), complement C3-AgNP mixtures, actin-AgNP (400:1 molar ratio) mixtures, tubulin-AgNP (400:1 molar ratio) mixtures, complement C3 (0.06 mg/mL), 20 nm AgNP (0.01 mg/mL), 110 nm AgNP (0.01 mg/mL) were determined in standard 1 cm polypropylene plastic cuvettes at room temperature using dynamic light scattering (DLS) (Zetasizer Nano ZS, Malvern Instruments). The protein and AgNP were diluted from their stock solutions by adding deionized water to minimize the influence of salts. The protein-AgNP mixtures were incubated for 30 min at room temperature prior to the measurements. [47]

Transmission electron microscopy (TEM) imaging

TEM is a technique where a beam of electrons is transmitted through an ultra-thin specimen at the same time interacting with the specimen as it passes through. The comparison of NP and protein-NP corona TEM images can give visualization of protein-NP interaction and confirm coating of NP by a layer(s) of protein. Direct observations of nanoparticle and protein-NP corona were performed on a Hitachi H7600 transmission

electron microscope, operated at a voltage of 120 KV. Specifically, AgNP (0.1 nM) were incubated with cytoskeletal proteins (40 nM) for 2 h at 4 ℃ before being pipetted onto a copper formvar grid. Samples were negatively stained for 10 min using phosphotungstic acid prior to imaging. 1.5 mg/L 20 nm AgNP was incubated with 5 mg/L complement C3 and 62.5 mg/L 110 nm AgNP was mixed with 75 mg/L complement C3 for 30 min at 4^{o}C before being pipetted onto a copper grid. After overnight embedding on the copper grid at room temperature, phosphotungstic acid was added to stain the complement C3-AgNP grids 10 min prior to imaging. All samples were prepared by directly diluting the stock solutions with deionized water.

Hyperspectral imaging:

Hyperspectral imaging combines high signal-to-noise dark field microscopy with high-resolution scattering spectra for each pixel has been employed recently by CytoViva Company for the detection of NP and their aggregations.[48-50] CytoViva Hyperspectral Imaging System is made of four components: (1) An imaging spectrophotometer that can record high quality spectra (high signal to noise ratio) in the visible and near-infrared (VNIR: 400-1000 nm) range. (2) A hyperspectral imaging spectrograph (fixed on the microscope) which can extract complete spectral information from single and multiple pixels. (3) A motorized stage precisely moves the sample across the hyperspectral imaging detector field of view. (4) An illumination scheme which makes the NP appears brighter, thus alleviating the need for staining or contrast agent to visualize the sample.[48, 51] AgNP (0.1 nM), and cytoskeletal protein-AgNP with 2 h and 48 h

incubation time were imaged using CytoViva Hyperspectral Imaging. Samples of 10 µL each were wet-mounted on glass slides, covered with #1 coverslips, and completely sealed with lacquer to prevent water evaporation. The spectra for every particle or aggregate in the image were obtained and the peak scattering wavelengths for each particle were identified by an automated process. A bin width of 5 nm was used to generate histograms of the peak scattering wavelengths of the samples ranged primarily between 500 to 660 nm. Peak scattering wavelengths less than 500 nm were allocated in the first "500 nm" bin while those larger than 660 nm were grouped in the last "660 nm" bin. The cross correlation between any pair of hyperspectral profiles was computed as the Pearson product-moment correlation coefficient

$$r = \frac{\sum_i (x_i - \bar{x})(y_i - \bar{y})}{\sqrt{\sum_i (x_i - \bar{x})^2} \sqrt{\sum_i (y_i - \bar{y})^2}},$$

where x_i and y_i correspond to the histogram counts of a given wavelength bin. A correlation coefficient of 1 suggests a high similarity between two spectral measurements, while a correlation coefficient close to 0 denotes low to no similarity. [52]

Circular dichroism (CD) spectroscopy:

CD is a spectroscopic technique widely used for the evaluation of the conformation and stability of proteins in vitro and in vivo environments.[53, 54] The optical property of the protein combined with the protein data bank (PDB) can be used to build a protein secondary structure library, which then allows us to use the denatured protein CD

spectrum for predicting the secondary structure changes of the protein.[55] To probe conformational changes in the secondary structure of protein due to its binding with AgNP, circular dichroism (CD) spectroscopy measurement was performed at room temperature on a Jasco J-810 spectropolarimeter (Easton, MD). The spectrum was collected from 190-300 nm. Specifically, cytoskeletal proteins (0.25 mg/mL) and cytoskeletal proteins (0.25 mg/mL) mixed with AgNP (0.05 mg/mL) were loaded into 0.01 cm path length high transparency quartz cuvettes (Starna Cells, Atascadero, CA). The CD spectra of protein-NP were measured after 30 min of incubation but within 1 h of preparation to avoid protein denaturation in the absence of salt. The spectrum of each sample was averaged over three scans taken at 20 nm/min and subtracted by the blank of deionized water. Once the CD signals were acquired, the spectra were then converted to their respective molar ellipticity units to derive information on the protein secondary structure. The ellipticity value (θ, in mdeg) provided by the instrument was converted to standard units of deg cm^2/dmol (designated as [θ]) using the equation $[\theta] = (\theta * M_0)/(10000 * C_{soln} * L)$, where M_0 is the mean residue molecular weight (114 g/mol), C is the protein concentration in solution (g/mL), and L is the path length through the buffer (cm). The CDPro uses a set of protein CD spectra and their secondary structures as a reference library developed from (1) soluble proteins, (2) soluble and denaturated proteins, and (3) soluble and membrane proteins to analyze the ellipticity. CONTIN/LL and CDSSTR methods provided with the CDPro package were used for the comparison. Each of the deconvoluted spectra was then assessed for quality by analyzing the R-fit using non-linear regression. SP43 and SP48 protein are used as reference datasets. The

percentage of secondary structure components were then derived from the average of various comparisons based on the reference library. The complement C3 structure information was measured by dilute the stock complement C3 or AgNP use deionized water to 0.4 mg/mL complement C3, 0.2 mg/mL 110nm AgNP and 6.67mg/L 20 nm AgNP. The final secondary structures represent the averaged structures obtained from all of the reliable outputs (R-fit < 10) resulting from the above described data analysis method.[55, 56]

Inductively coupled plasma mass spectrometry (ICP-MS)

AgNP in solution release silver ions over time, and the rate of this dissolution may be greatly reduced by capping agents or a protein corona on the particle surface. Direct observation of the release rate of silver ions by AgNP was performed using a ICP-MS (X Series 2, Thermo Scientific). Specifically, AgNP (5 mg/L, 0.0555 nM) were incubated with actin (5 mg/L, 116 nM) or tubulin (5 mg/L, 45 nM) after directly diluting the stock solutions with deionized water to the appropriate final concentrations. After incubating for 0 h, 2 h, 4 h, 6 h, 8.5 h, 12 h, 24 h, 48 h and 72 h, the cytoskeletal protein-AgNP mixtures were centrifuged twice at 12,100 g for 30 min and their supernatants were collected. The supernatants were then diluted with 2% HNO_3 and measured by ICP-MS using a standard silver ion solution with ^{45}Sc and ^{69}Ga as internal standards.

3.4 Results and Discussion

3.4.1 Cytoskeletal proteins-actin and tubulin interact with 30 nm citrated acid coated AgNP

As shown in Table 3.1, the zeta potentials of cytoskeletal protein-AgNP are closer to that of cytoskeletal protein than to AgNP. This is due to the coating of cytoskeletal protein on the AgNP as well as free proteins, as reflected by the UV-Vis spectral shifts and TEM images (Fig.3.1 and 3.2). Actin and tubulin both yielded high standard deviations for their zeta potentials (Table 3.1), possibly due to self-aggregation and minor polymerization. In addition, actin-AgNP displayed a smaller standard deviation in zeta potential than tubulin-AgNP (Table 3.1), implying that the actin-AgNP corona was more homogeneous than the tubulin-AgNP corona.[47]

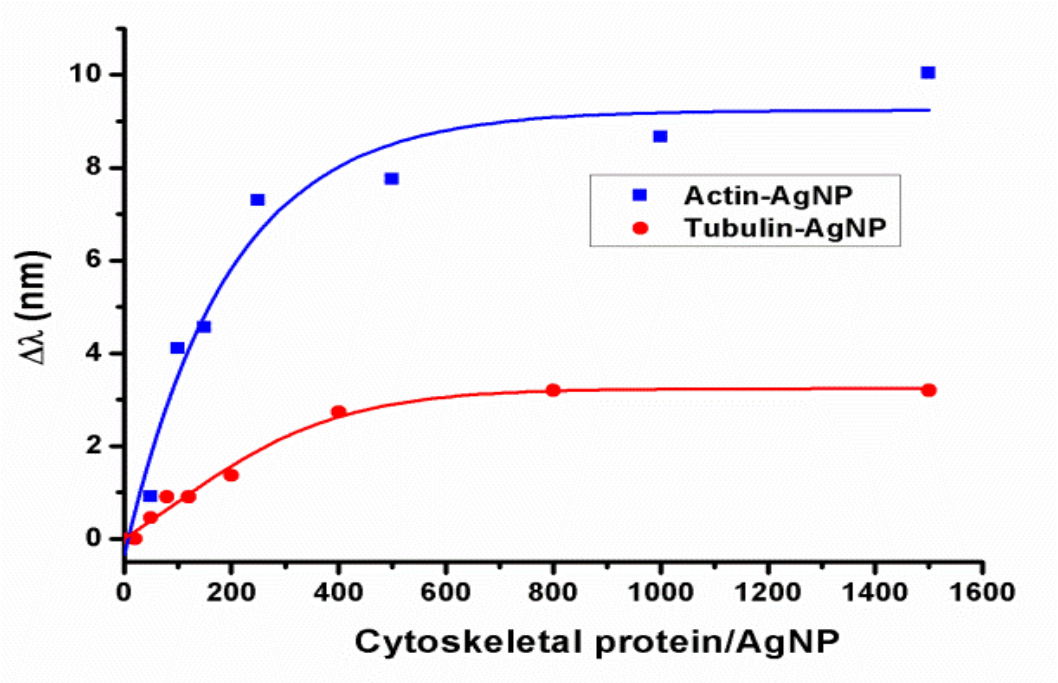

Figure 3. 1 Red-shifts of UV-Vis absorbance peak wavelengths induced by the formation of cytoskeletal protein-AgNP coronas, in reference to that for AgNP alone at $\lambda_0 = 406$ nm. The horizontal axis shows the molar ratios of cytoskeletal protein to AgNP.

	Hydrodynamic size (nm)	Zeta potential (mV)
AgNP	~35.7 ±0.2	-42.5 ±0.1
Actin	~2.0	~28.0 ±5.6
Actin-AgNP	~39.4 ±0.7	-31.6 ±0.8
Tubulin	~9.0 (aggregaation)	-27.1 ±3.3
Tubulin-AgNP	~44.7 ±0.6	-27.0 ±2.6

Table 3. 1 Hydrodynamic sizes and zeta potentials of AgNP and cytoskeletal protein-AgNP

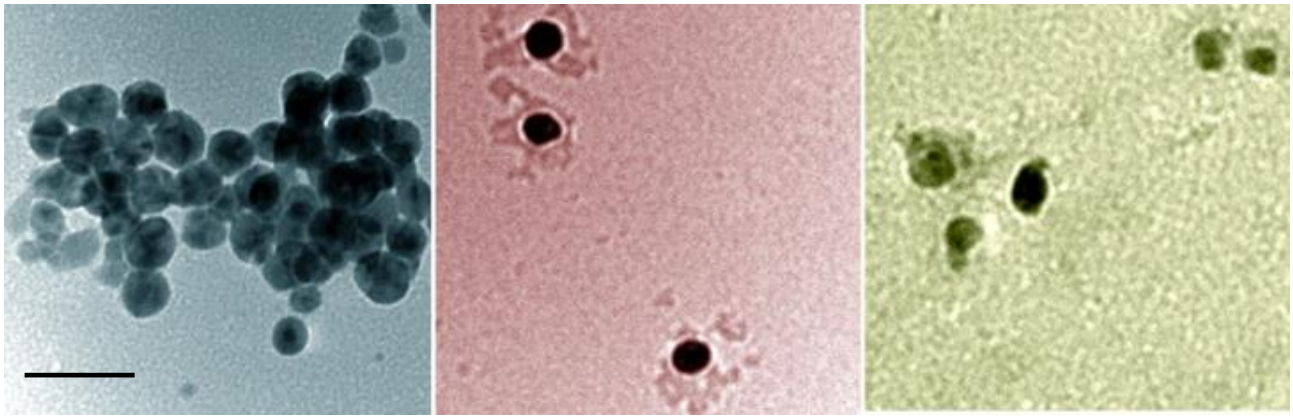

Figure 3. 2 TEM imaging of (left) citrate-coated AgNP, (middle) actin-AgNP, and (right) tubulin-AgNP coronas. Scale bar: 100 nm.

Actin (polydispersity index or PDI: 0.659) and tubulin (PDI: 0.662) displayed broad size distributions in their buffers because they tend to aggregate. However, the cytoskeletal protein-AgNP were more uniform in size (PDI: 0.286 for actin-AgNP and 0.290 for tubulin-AgNP), evidently due to the breakage of protein aggregates by the AgNP. The hydrodynamic size of actin-AgNP increased by 3.7 nm than AgNP (twice the hydrodynamic size of actin), indicating coating of a single actin layer on the AgNP. In comparison, the hydrodynamic size of tubulin-AgNP increased by 9.1 nm (~the hydrodynamic size of tubulin) than AgNP, suggesting that the AgNP were partially coated by a single layer of tubulin. These results agree qualitatively with the UV-Vis absorbance and TEM data (Fig. 3.1 and 3.2). The UV-Vis spectra were measured within

two hours of sample preparing to minimize the influence of potential protein denaturation. By comparing the UV protein absorbance intensities (280 nm for tubulin, 260 nm for actin) after 2 h incubation of proteins with AgNP (1500: 1 molar ratio) and removing all AgNP and strongly bound cytoskeletal proteins by centrifugation and comparing to control protein UV-Vis spectra, we concluded that AgNP have a strong binding capacity for 150 and 300 tubulin and actin molecules per particle, respectively. This further suggests that monolayers being formed on the nanoparticle surfaces. The smaller size and greater flexibility of actin (~2 nm) compared to tubulin (~9 nm) as well as the hydrodynamic size data suggest that actin results in more complete surface coverage of the AgNP. This explains the greater SPR red shift seen in Fig.3.1, as a larger degree of surface coverage by protein will result in a more significant change in the local dielectric constant, resulting in a more significant red-shift of the AgNP SPR.

Since protein coating induced red-shifts in the SPR spectra of the AgNP, red-shifts also occurred in the peak scattering wavelengths for protein-coated AgNP than AgNP alone. Our hyperspectral imaging showed a maximum spectral peak at 550 nm for the AgNP (Fig. 3.3, orange bars in B & D), as a result of AgNP self-aggregation. In comparison, a slight blue-shift was observed for actin-AgNP with 2 h incubation and a further enhanced blue-shift was observed for actin-AgNP with 48 h incubation, likely through continued breakage of AgNP aggregates over time as seen more NP showed SPR peak blue shifted. (Fig. 3.3, B & D). Indeed, the cross-correlations of the hyperspectral histograms for actin-AgNP at 2 h and 48 h with AgNP at 2 h are 0.97 and 0.24,

respectively. In contrast, the spectra of tubulin-AgNP after 2 h incubation yielded a broader distribution compared with AgNP alone (Fig.3.3 D, orange vs. green bars), likely caused by self-aggregation and polymerization of the tubulin. Like actin, tubulin also facilitated the breakdown of AgNP aggregates, though less effectively (Fig. 3.3, B vs D, see counts for wavelengths below 550 nm) and displaying no apparent time dependence (cross correlations with AgNP at 0.63 vs. 0.60, Fig. 3.3 E). The double-shoulder spectra in Fig. 3.3 C for tubulin-AgNP indicate an aggregation-induced quadrupole resonance that is different from the primary resonance in electron oscillation.

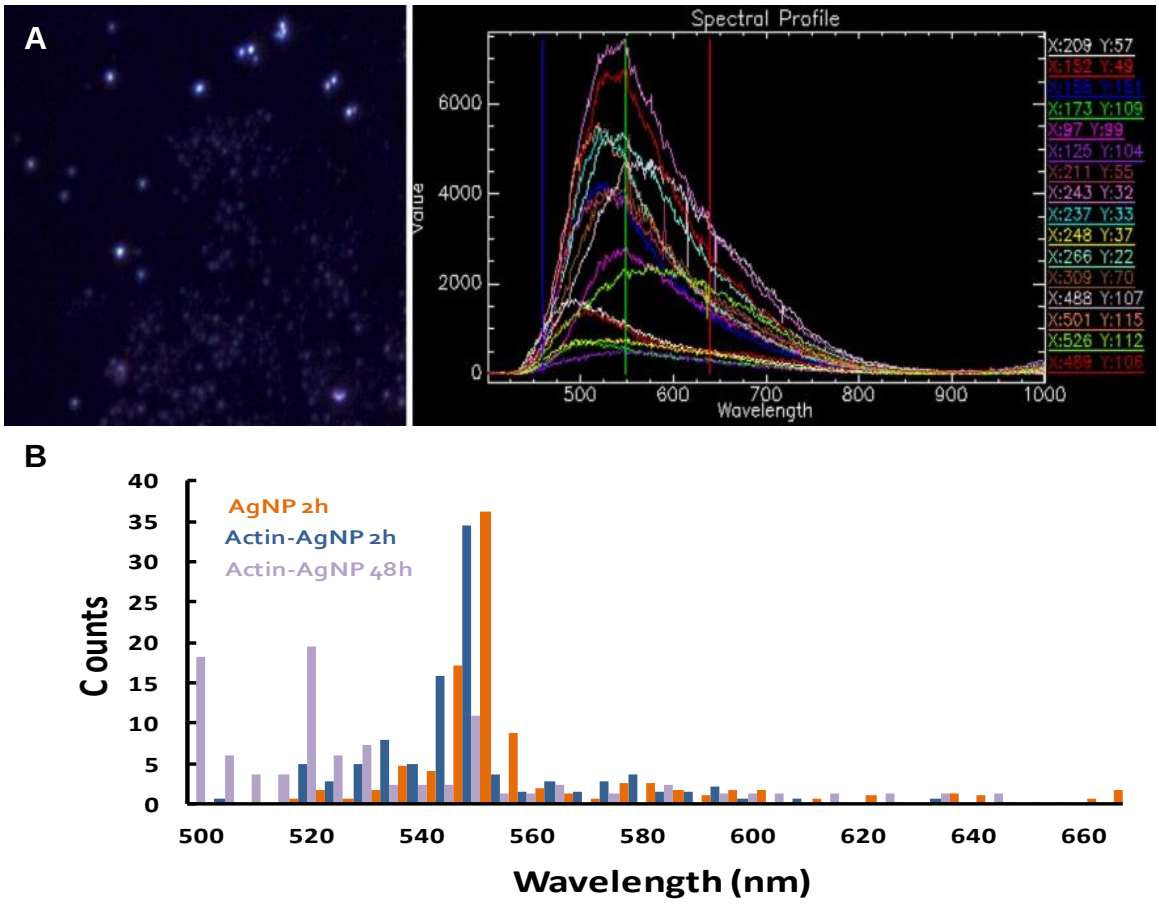

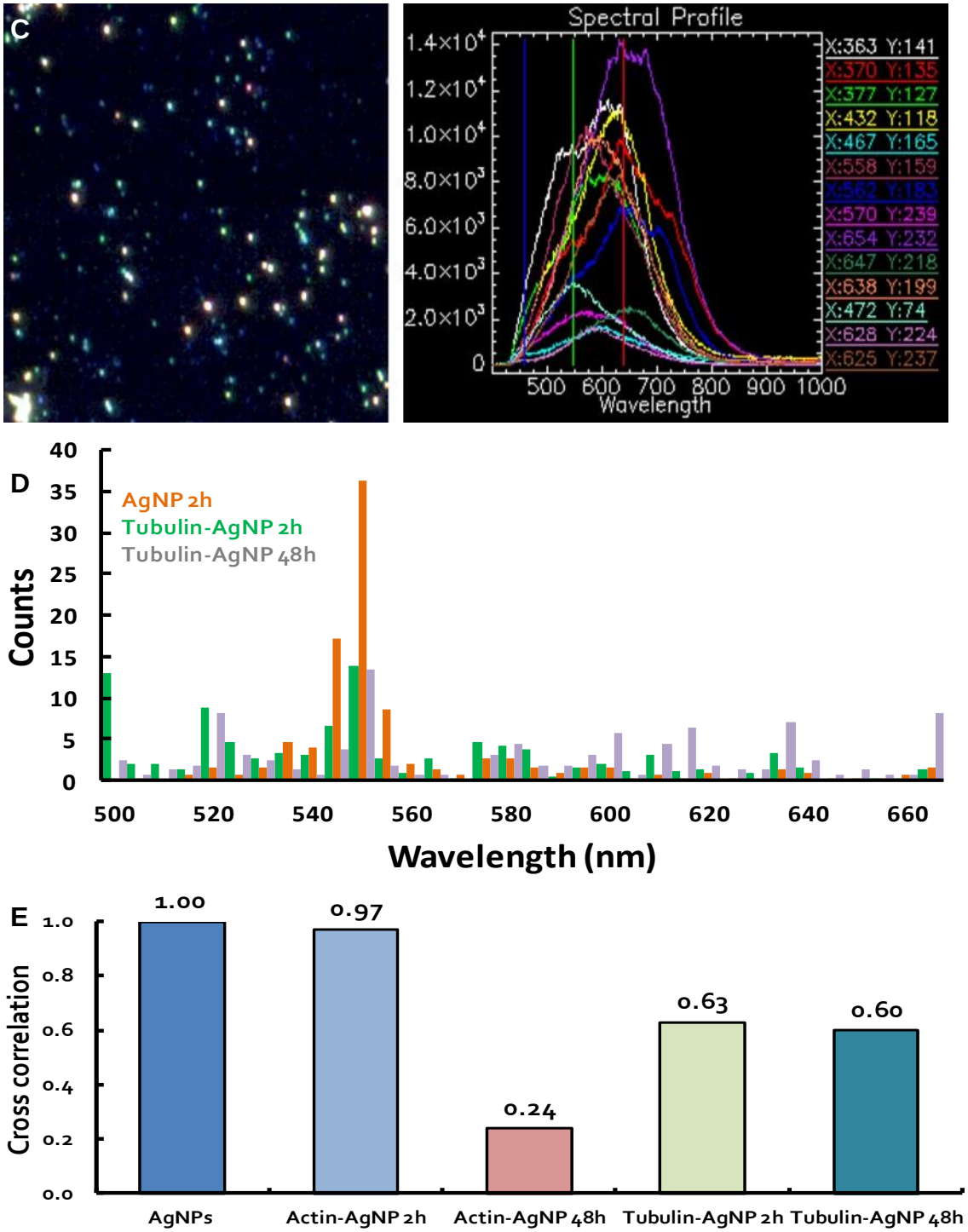

Figure 3. 3 Examplary CytoViva images and their corresponding hyperspectra for actin-AgNP **(A)** and tubulin-AgNP **(B)** at 2 h, respectively. Histogram of the hyperspectra of AgNP & actin-AgNP **(C)** and AgNP & tubulin-AgNP **(D)** respectively. Bin width: 5 nm. A total number of 82 to 359 particles were screened in each case to derive the histograms. **(E)** Cross correlations of the hyperspectra of cytoskeletal protein-AgNP with that of AgNP.

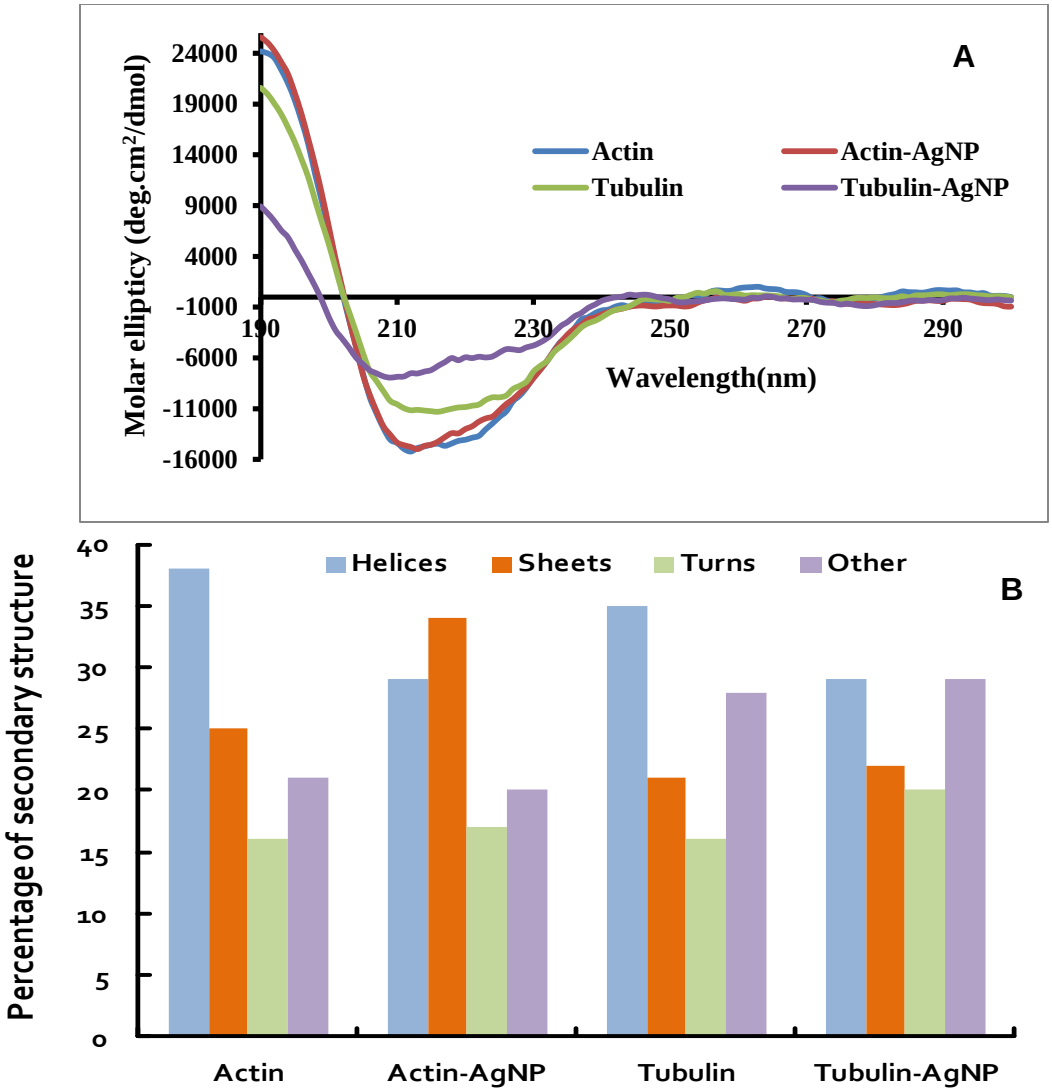

Figure 3. 4 (A) CD spectra of actin, tubulin, actin-AgNP corona and tubulin-AgNP corona **(B)** Changes in the secondary structures of actin and tubulin upon their binding with AgNP. Note the consistent decreases in alpha helices and increases in the beta sheets for both types of proteins when bound to 30 nm AgNP.

The secondary structures of actin and tubulin were altered resulting from their interactions with the AgNP as shown in circular dichoric result (Fig. 3.4). Specifically, the alpha helices of actin showed a 24% relative decrease (from 38% to 29%) and beta sheets a 36% relative increase (from 25% to 34%) upon their binding with the AgNP. In comparison, the alpha helices of tubulin displayed a 17% relative decrease (from 35% to

29%) and beta sheets a 5% relative increase (from 21% to 22%) once bound to the AgNP. In other words, both actin and tubulin showed a decrease in alpha helices and an increase in beta sheets upon corona formation, similarly to that observed for tubulin exposed to hydroxylated fullerene.[57] In addition, the conformational changes were greater for actin than tubulin, consistent with our UV-Vis absorbance measurement and hyperspectral imaging (Fig. 3.1 and 3.3).

The differential binding of actin and tubulin for AgNP, as reflected by the absorbance, hyperspectral imaging, and CD measurements, can be derived from the discrepancies in the physicochemical and structural properties of the two types of cytoskeletal proteins. Since both actin and tubulin are rich in alpha helices (both at 35%) and turns and their zeta potentials were nearly identical, at approximately -27 to -28 mV (Table 3.1), we attribute the observed differential binding to the differences in the rigidity and size of the two types of proteins. Structurally, actin is a globular protein of 43 kDa while tubulin is an alpha-beta dimer of 110 kDa. Both actin and tubulin can be polymerized into microfilaments and microtubules respectively under favourable conditions, with microtubules possessing a higher rigidity and a much longer persistence length than actin filaments. In the cell, actin carries out more interactions than most other proteins and it is conceivable that actin bound more efficiently to citrate-coated AgNP than tubulin. Such binding is likely realised via hydrogen bonding between the citrate coating of the AgNP and the abundant peripheral alpha helices and turns of the proteins, in addition to electrostatic, van der Waals, and hydrophobic interactions between the two

species. The hydrogen bonding with citrate-coated AgNP perturbed the structural integrity of the alpha helices and turns that populated the protein surfaces, as reflected by our CD measurements for both actin and tubulin (Fig.3.4). Due to the highly localized nature of hydrogen bonding (typically 2-3 angstroms in bond length), the larger sized tubulin should be less efficient than actin for their binding to the AgNP that possessed a significant curvature. Furthermore, as a non-covalent capping agent, citrate could undergo rapid and stochastic exchanges with the cytoskeletal proteins in aqueous for adsorbing onto the AgNP. Sterically, the smaller actin should be more flexible than tubulin in occupying the AgNP surface areas transiently free from citrate coating, through electrostatic and hydrophobic interactions.

As shown from ICP-MS result (Fig.3.5), without the presence of cytoskeletal proteins (black curve) AgNP rapidly released silver ions, from 0.13 to 0.20 mg/L within the first 4 h, while the rate of release levelled off subsequently for the total observation period of 72 h. The released silver ions reached a concentration of ~0.27 mg/L at 72 h for an original AgNP concentration of 5 mg/L, implying a ~5% dissolution of the NP. In the presence of actin and tubulin (blue and red curves), in contrast, the release of silver ions progressed at a slower pace, from ~0.06 to 0.08 mg/L during the first few hours. Such ion release was then briefly saturated, reduced, and levelled off to a final concentration of ~0.05 mg/L, or ~20% of that released by AgNP over 72 h without the presence of proteins. This measurement implies that the coating of cytoskeletal proteins on the AgNP physically hindered the release of silver ions. This hindered ion release process competed

with the dynamic process of forming protein corona, and eventually dominated silver ion release to stabilize the AgNP. This time-dependent result further suggests that the conformation and physicochemical properties of AgNP are better preserved by hardened cytoskeletal proteins. However, it also implies that the formation of protein corona alone is insufficient to fully scavenge silver ions that are a major cause of triggering ROS production and cytotoxicity.

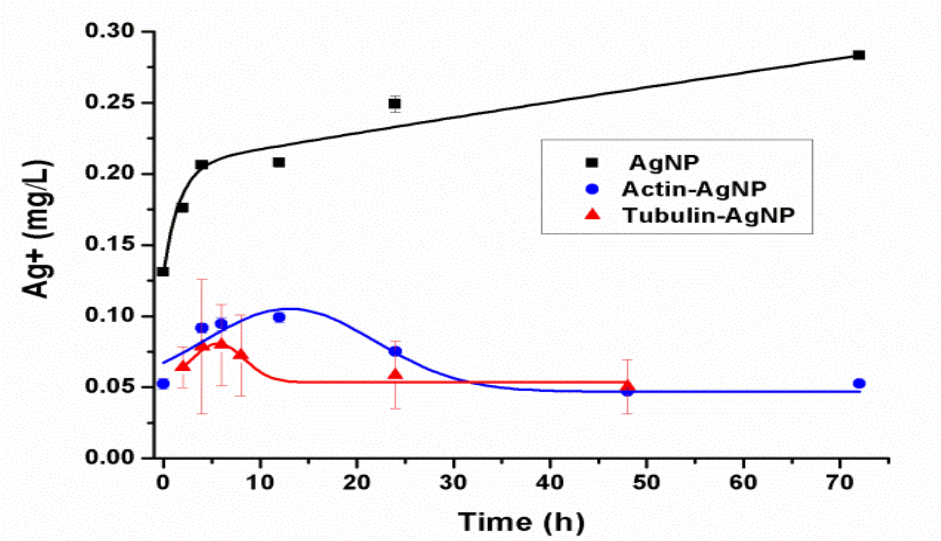

Figure 3. 5 Release of silver ions with and without the presence of cytoskeletal proteins, measured using ICP-MS. Original AgNP concentration: 5 mg/L. Actin and tubulin concentrations: 5 mg/L.

In summary, we have characterised the binding of cytoskeletal proteins, namely, actin and tubulin, with 30 nm citrated coated AgNP using the techniques of dynamic light scattering, UV-Vis spectrophotometry, circular dichroism spectroscopy, hyperspectral imaging, and transmission electron microscopy. Data have shown that cytoskeletal proteins can interact readily with citrate-coated AgNP. Overall, actin displayed a higher propensity than tubulin for the silver nanoparticle while both proteins experienced

conformational changes upon the binding, likely originated from their smaller size and less rigidity. Binding with the AgNP on one hand induced changes in the secondary structures for both types of proteins, while on the other hand compromised silver ion release from the AgNP as a result of protein corona formation and hardening. The ion release from the silver nanoparticle was significantly compromised upon the formation of protein coronas. The implications of cytoskeletal protein corona on the transformation and cytotoxicity of silver nanoparticle have been discussed. The knowledge derived from this study may facilitate our understanding of the dynamics, transformation, and distribution of nanomaterial in mammalian and plant cells, and may have relevance to the field studies of biomolecular-NP interactions, toxicology, biosensing, and medicine involving metallic NP.

3.4.2 Immune protein-complement component 3 (Complement C3) interacts with AgNP

As shown in Table 3.2, the zeta potentials of complement C3-AgNP are higher than -30 mV, which implies complement C3-AgNP corona is less stable than AgNP alone and complement C3 alone. This might be due to the coating of immune protein on the AgNP as complement C3 has a 180kDa molecular weight, implying a bigger size protein surrounding the surface of nanoparticle. The size of the complement C3-20 nm AgNP corona increased by 35.6 nm (from 27.0 nm to 62.6 nm), approximately doubling the size of complement C3 and suggesting a single layer coverage of the protein on the surfaces of the 20 nm AgNP. In contrast, the size of the complement C3-110 nm AgNP corona

increased by 56.6 nm (from 113.0 nm to 169.6 nm), implying a coverage of 1~2 layers of complement C3 on the surfaces of the 110 nm AgNP.

	Hydrodynamic size (nm)	Zeta potenmtial (mV)
Com3	~16.8 ±2.0	~-40.97 ±1.42
20nm AgNP	~27.0 ±0.2	~-34.90 ±0.57
110nm AgNP	~113.0 ±0.2	~-41.30 ±0.99
20AgNP-Com 3	~62.6 ±0.6	~-17.80 ±0.49
110AgNP-Com3	~169.6 ±2.8	~-16.53 ±0.17

Table 3. 2 Hydrodynamic sizes and zeta potentials of AgNP and Com3-AgNP corona.

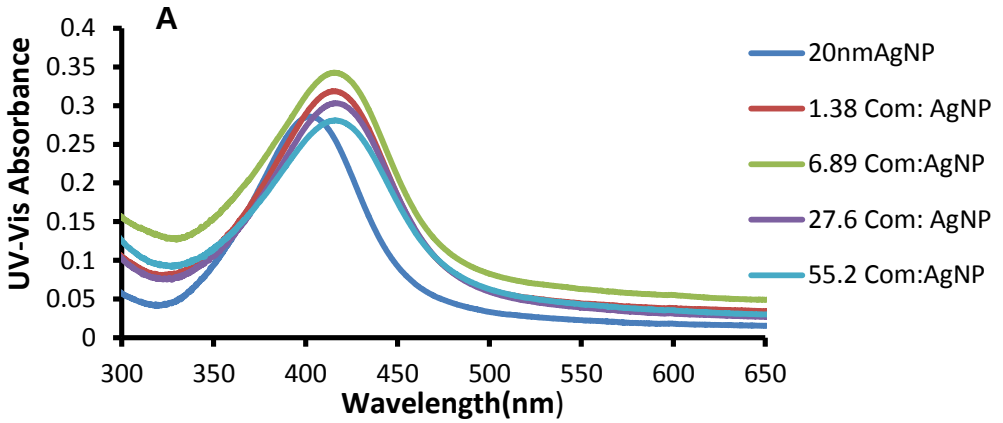

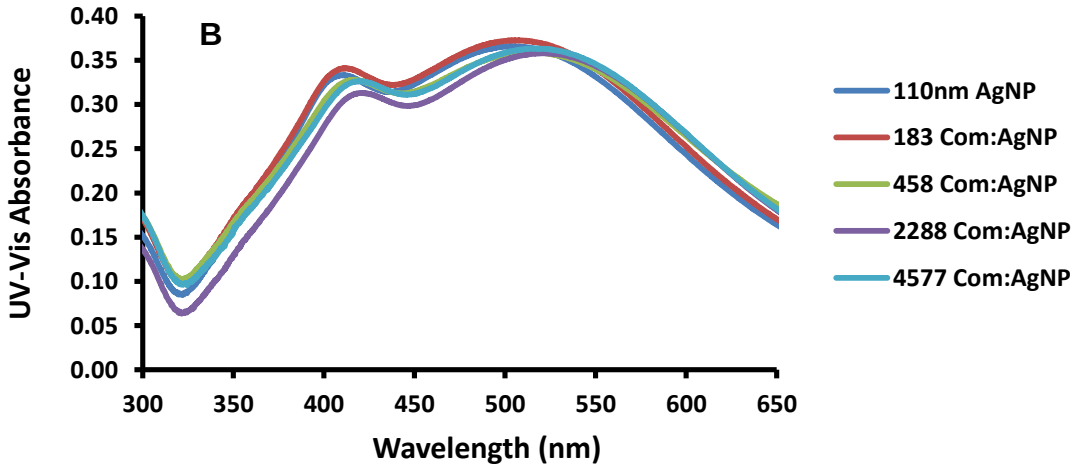

Figure 3. 6 Complement component 3 (C3) interacts with 20nm AgNP **(A)** and 110nm AgNP **(B)** at different protein nanoparticle ratios. Red-shifts of UV-Vis absorbance peak wavelengths induced by the formation of protein-AgNP coronas, in reference to that for AgNP alone. UV-Vis absorbance of 20 nm AgNP shift from 402.4 nm to 415.4 nm, 110 nm AgNP shift from 505.4 to 514.4 nm.

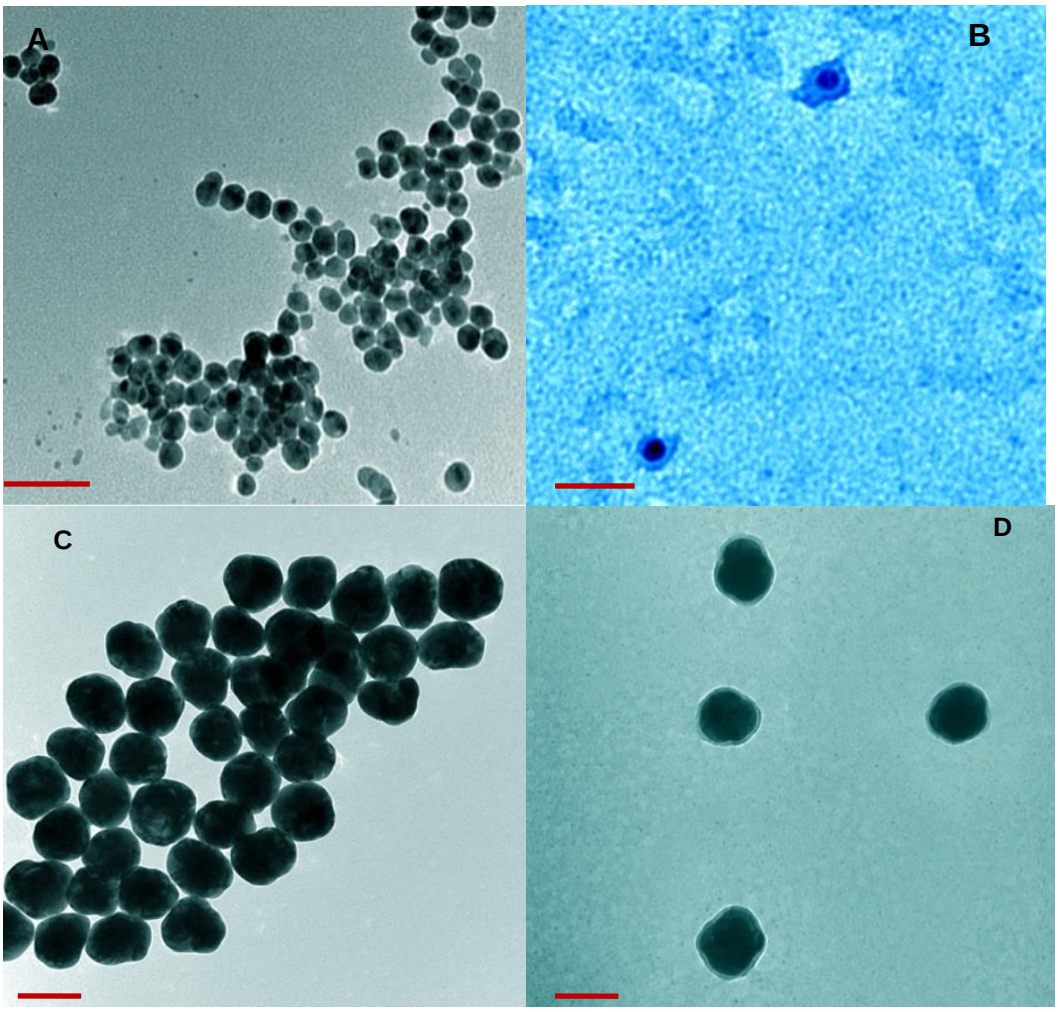

Figure 3. 7 (A)TEM images of 20 nmAgNP and **(B)**20nm AgNP coated with complement C3. Scale bars for both images are 100 nm. **(C)** TEM images of 110 nmAgNP and **(D)** 110nm AgNP coated with complement C3. Scale bars for all images are 100 nm.

As shown in Fig. 3.6, the UV-Vis spectra of complement C3-AgNP red-shifted gradually compared with that of the AgNP alone. This was mainly due to the increased dielectric constants of the protein-AgNP coronas and consequently red-shifts in the surface plasmon resonance (SPR) of the AgNP. Specifically, complement C3 caused a 13 nm redshift for AgNP of 20 nm (Fig. 3.6 A from 420.4 nm to 415.4 nm) and a 9 nm

redshift for AgNP of 110 nm in size (Fig. 3.6 B from 505.4 nm to 514.4 nm). As the protein/AgNP molar ratio increased, the redshifts of the AgNP SPR peak were also enhanced until saturated. The redshift for AgNP of 20 nm reached saturation readily when compared with AgNP of 110 nm, likely due to the smaller size and thus less protein to render the corona which can be calculated by equation

$$< n = [4\pi(R_{AgNP} + r_{protein})^2] / \pi r_{protein}^2 >$$

TEM images of AgNP and complement C3-AgNP corona were shown in Fig 3.7. The complementary C3 bind onto the surface of AgNP, with thickness matching with the hydrodynamic sizes in Table 3.2. To probe the conformational variation in the complement C3 secondary structures change due to the bound of 20 nm and 110 nm citrate-coated AgNP, circular dichroism spectroscopy measurements were performed at room temperature. As seen in the CD results (Fig. 3.8) the size of nanoparticles has an influence on the protein's secondary structure. This finding was similar to that of Shannahan et al, who found that 20 nm AgNP bound more strongly to hydrophobic proteins than did 110 nm AgNP.[58, 59] These phenomena may also be caused by the size of complement C3 which is close to 20 nm in radius. This would spatially hinder its binding to the 20 nm AgNP and freely bind to the 110 nm AgNP. Thus 20 nm AgNP will have a stronger effect on the structure change of complement C3 protein as shown in Fig. 3.8 B. The 20 nm C3-AgNP protein corona is giving a higher degree of σ helixes and β sheets changes compared with 110 nm C3-AgNP corona. The relative bigger size of complement C3 protein may also explain why the decrease of stability upon its binding

with AgNP decreases (Table 2.2). The larger secondary structure changes generated by binding with 20 nm AgNP matches with the SPR peak shift in Fig 3.6, as 110 nm AgNP get less influenced by complement C3 protein.

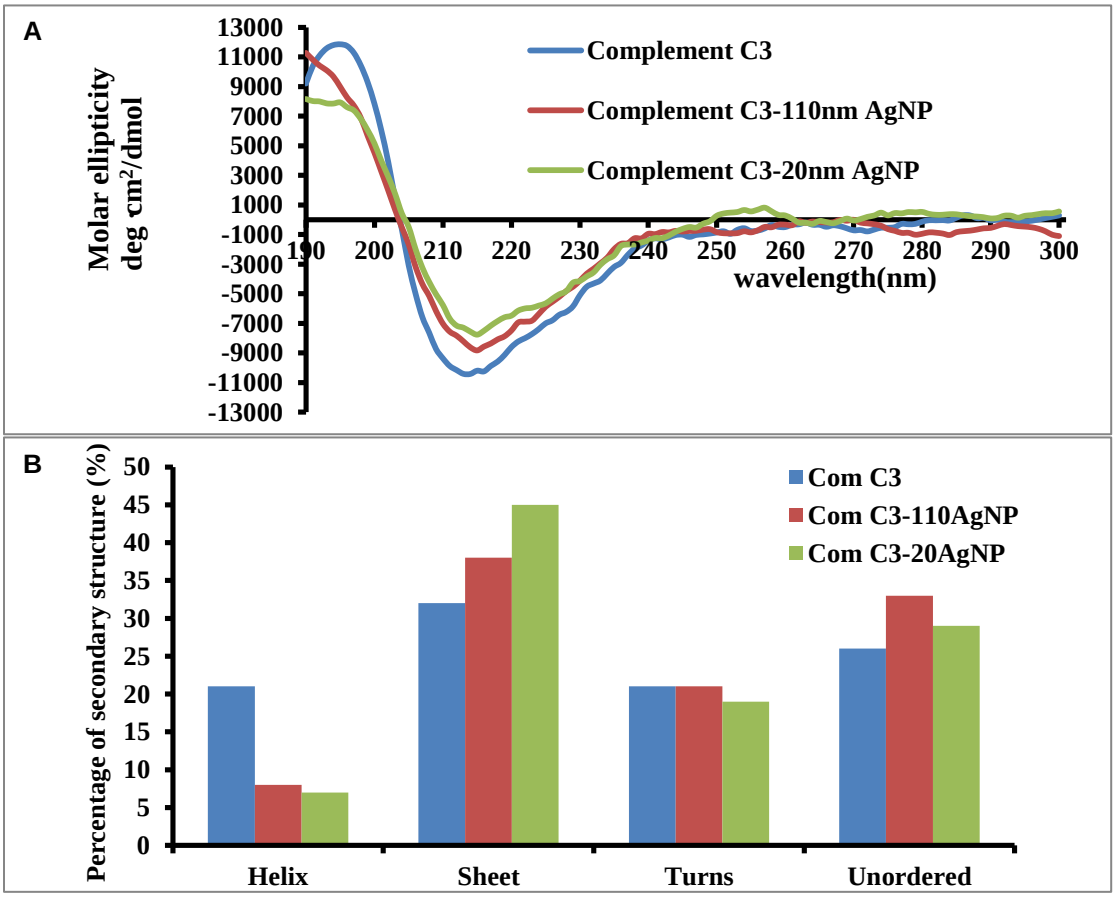

Figure 3. 8 (A) CD spectra of complement C3, complement C3-20 nm AgNP corona, complement C3-110 nm AgNP corona. **(B)** Changes in the secondary structures of C3 upon its binding with AgNP. Note the consistent decreases in alpha helices and increases in the beta sheets with decreasing AgNP size when bound to the AgNP.

In summary, we have characterized the binding of complement C3 protein, with 20 nm and 110 nm citrated coated AgNP using the techniques of dynamic light scattering, UV-Vis spectrophotometry, circular dichroism spectroscopy, and transmission electron

microscopy. Data have shown that compared with 110 nm AgNP, 20 nm AgNP will have a bigger influence on complement C3 secondary structure changes.

3.4.3 Lipid protein- apoliporotein interacts with AgNP

In the study of apolipoproteins (Apo), stock apolipoprotein (Sigma, USA) with diluted with deionized water to 0.5 nM, then incubated with AgNP at Apo/AgNP molar ratios of 300 and 600. The DLS and Zeta potential results show that the hydrodynamic size of Apo-AgNP corona is increased with increasing Apo/AgNP ratios and the higher ratio also resulted in better stability as indicated by the increased absolute value of the zeta potential.[60] The hydrodynamic size of the AgNP was measured by DLS as 35.71 nm, while the hydrodynamic sizes of Apo-AgNP corona were 38.5 and 39.4 nm for the NP/protein molar ratios of 1:300 and 1:600 respectively. In contrast, the hydrodynamic size of the apolipoprotein (molecular weight ~9 kDa) was ~1.39 nm. Accordingly, the zeta potentials of the AgNP and apolipoprotein were determined to be -42.5 and -33.7 mV, while the zeta potentials of the apo-AgNP corona were -37.4 and -38.6 mV for the NP/protein molar ratios of 1:300 and 1:600, respectively. (Table 3.3).[60] Size difference between Apo-AgNP 300 and AgNP is around 2.78 nm, which imply a layer of Apo surrounding AgNP. Size difference between Apo-AgNP 600 and AgNP is around 3.64 nm, which imply thicker layer of Apo will be on the surface of AgNP. The size and zeta potentials differences between 300 and 600 apo to AgNP are relative small may imply the fact that 300 Apo to AgNP ratio is sufficient to cover the surface of AgNP.

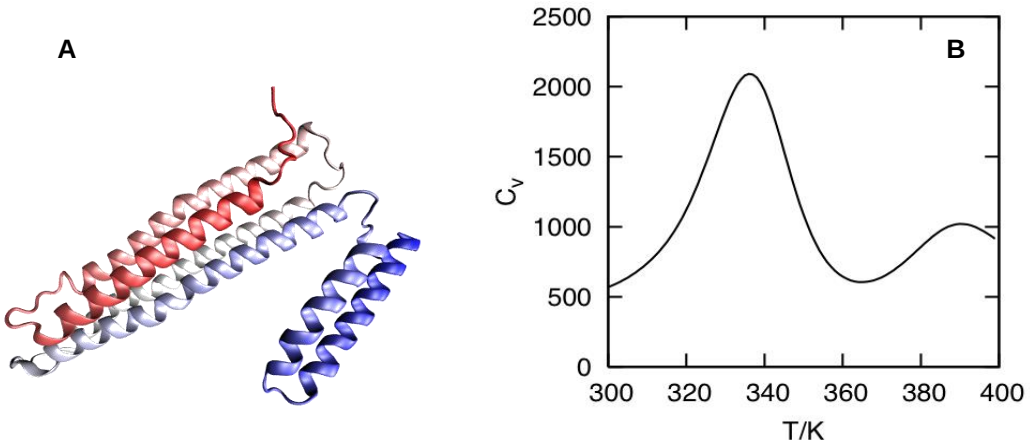

Figure 3. 9 Folding of apolipoprotein. (A) A ribbon diagram of a single apolipoprotein colored from the N-terminal (red) to C-terminal (blue) in a spectrum along its sequence. (B) Specific heat profile with respect to temperature from coarse-grained Go-model folding simulations of a single apolipoprotein.

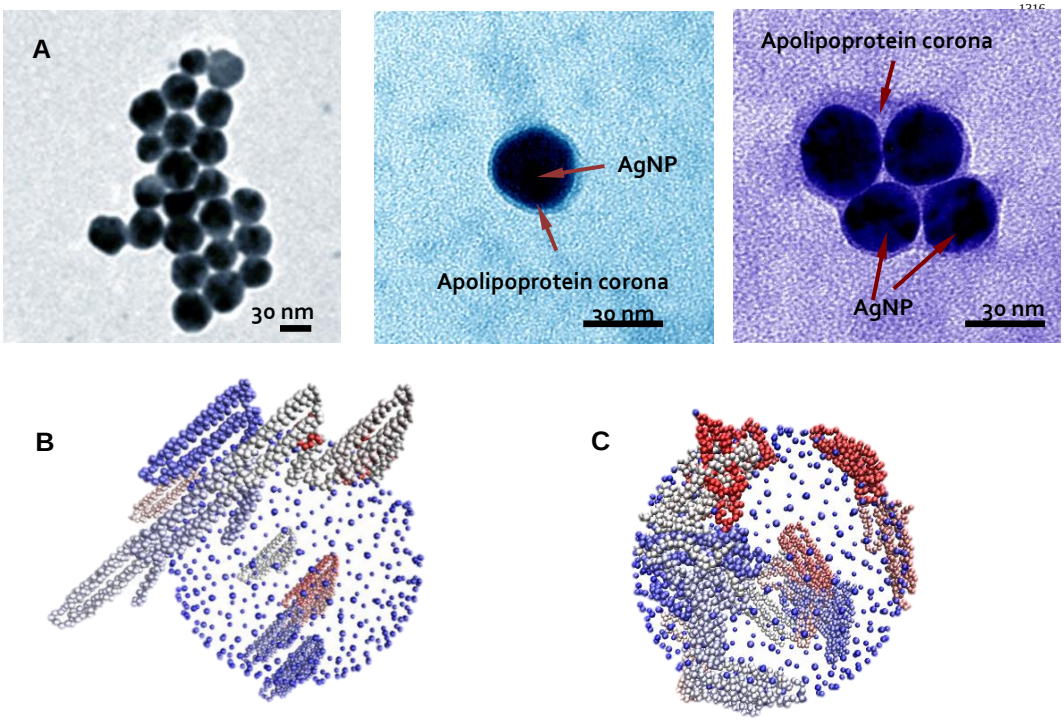

Figure 3. 10 Biocorona formation from interactions of AgNP with apolipoprotein. (A) TEM images of (left) dehydrated citrate-coated AgNP of 30 nm and (middle-right) apolipoprotein-AgNP coronas. **(B)** The initial setup of a coarse-grained MD simulation of 15 apolipoproteins (colored red, gray and blue) near a positively charged spherical model of AgNP (blue) that is 10 nm in diameter. **(C)** A snapshot of an Apolipoprotein-AgNP biocorona from our GPU-optimized coarse-grained MD simulations at low ion concentration.

	Hydrodynamic size(nm)	Zeta potential(mV)
Apo	~1.39 ± 0.39	-42.5 ± 0.1
AgNP	~35.71 ± 0.25	-33.7 ± 1.3
Apo-AgNP 300	~38.49 ± 0.53	-37.4 ± 0.4
Apo-AgNP 600	~39.35 ± 0.43	-38.6 ± 0.6

Table 3. 3 Hydrodynamic sizes and zeta potentials of AgNP and apolipoprotein-AgNP corona.

To characterize the biocorona formation of an AgNP interacting with apolipoprotein, we collaborated with Dr Rongzhong Li and Dr Samuel S. Cho. Apolipoprotein is a α-helical protein that consists of three helices. The specific heat profile with respect to temperature (Fig 3.9) shows that the folding mechanism consists of two distinct peaks that correspond to two melting temperatures (Fig 3.9 B). The sizes of the AgNP and Apo-AgNP corona shown in TEM images (Fig 3.10A) are in agreement with the DLS size measurement (Table 3.3). Since the protein layer is ~2 nm from the TEM imaging (Fig. 3.10 A) and ~3 nm from the DLS measurement (Table3.3), while the width of an α helix is ~0.4 nm, multilayer protein coating on the AgNP was deemed plausible. A coarse-grained MD simulation Hamiltonian for the biocorona formed from dehydrated citrate-coated AgNP interacting with apolipoprotein was developed by Dr Rongzhong Li and Dr Samuel S. Cho based on the TEM observation (Fig. 3.10 A) and our knowledge about the chemical structure of the citrate coated AgNP. The major contributors to the protein-nanoparticle interactions would be expected to be excluded volume interactions and electrostatic interactions between the negatively charged citrate and the positively charged residues in apolipoprotein. As such, a charged spherical AgNP that consisted of 500 individual charged spheres (charged spheres represent citrated acid coating) with excluded volume was added with 15 apolipoproteins in random positions

proximal to the AgNP surface (Fig. 3.10 B). Once the Apolipoprotein-AgNP system was set up, MD simulations of the system was performed over a range of ion concentrations. In a relatively short period of time, the apolipoprotein became attracted to the AgNP and adhered to its surface (Fig. 3.10 C). Compared with CD spectra of apolipoprotein, in the presence of AgNP at 300:1 and 600:1 concentration ratios, the α-helix of the apolipoprotein decreased in both cases (Fig.3.11 A). To make a direct quantitative comparison with this observation, the secondary structure content was monitored in the MD simulation by measuring the backbone torsional angle of the apolipoprotein, and we observed a reduction in the α-helical content from about 65% to 45% in simulation which matched the experimental results shown in Fig. 3.11.

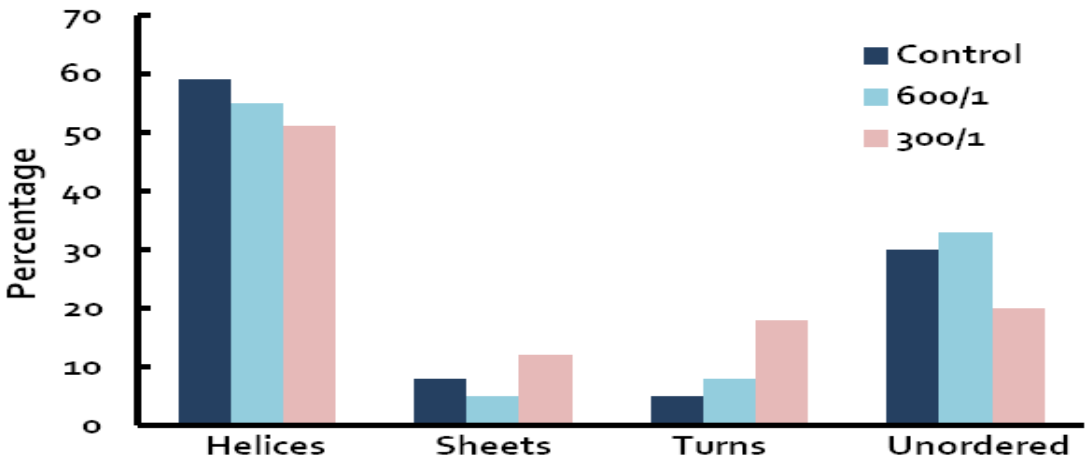

Figure 3. 11 Reduction of alpha-helical content upon biocorona formation.Secondary structure contents are shown for apolipoproteins in the presence of AgNP of ratios 300:1 and 600:1 as measured by CD. The alpha-helical content is reduced with greater apolipoprotein concentration while the beta sheet content is increased at 300 ratio but decreased at 600 ratio.

3.4.4 Plasma protein - albumin and fibrinogen (FBI) interact with AuNP.

Fibrinogen is a key component in the blood clotting process and can support both platelet-platelet and platelet-surface interactions by binding to the glycoprotein IIb-IIIa (GPIIb-IIIa) receptor.[61] Albumin is soluble, monomeric and can transport most fat soluble hormones, fatty acids, and drugs in blood serum. To compare the different interactions between fibrinogen and albumin with AuNP, UV-Vis spectra of albumin-AuNP corona and fibrinogen-AuNP corona were compared with albumin and fibrinogen respectively (Fig. 3.12). It is seen that higher concentration of fibrinogen is needed to saturate coating AuNP. Albumin causes the SPR peak of AuNP to shift from 525.8 nm to 529.8 nm while fibrinogen causes the SPR peak of AuNP to shift from 525.8 nm to 526.4 nm at 0.02 mg/ml. For 0.82 mg/ml AuNP, 0.01 mg/ml BSA is generating a maximum SPR peak shift (4 nm) while 0.16 mg/ml fibrinogen was needed to cause the maximum SPR peak shift (3 nm). More FBI was needed to interact with AuNP to get to a saturate state while BSA-AuNP corona reaches saturation at a much lower BSA concentration.

The interaction of BSA and FBI with AuNP was also studied using Fluorescence Spectroscopy as shown in Fig. 3.13 and Fig. 3.14. All AuNP concentrations are the same at 0.15 mg/ml, Alexa Fluor 488 conjugate FBI 0.15 mg/ml was excited at 490nm (Fig. 3.14 A), Texa Red coagulate-Albumin 0.15 mg/ml was excited at 590 nm (Fig. 3.14 B), while fluorescence labeled FBI and BSA were excited at 545 nm (Fig. 3.14 C). Fluorescence spectra were collected on Texa Red coagulate-Albumin (F-BSA), Alexa

Fluor 488 conjugate FBI (F-FBI). F-BSA was incubated with AuNP, F-FBI with AuNP, F-BSA with AuNP then F-FBI was added. Incubated F-FBI with AuNP was then treated with F-BSA. The F-BSA and F-FBI mixture was incubated with AuNP for comparison. As it's shown in Fig.3.14 A &B, upon 1:1 incubation ratio between F-BSA and AuNP, F-FBI and AuNP, fluorescence signal was quenched partially when AuNP is causing protein deformation. Even after the formation of F-FBI-AuNP corona, introducing F-BSA into the solution can introduce further fluorescence intensity decreases (from 32.28% to 18%) while after the formation of F-BSA-AuNP corona, introducing F-FBI into the solution has no influence on fluorescence intensity. This feature confirms that AuNP have less influence on the albumin structure compared with the influence on fibrinogen.

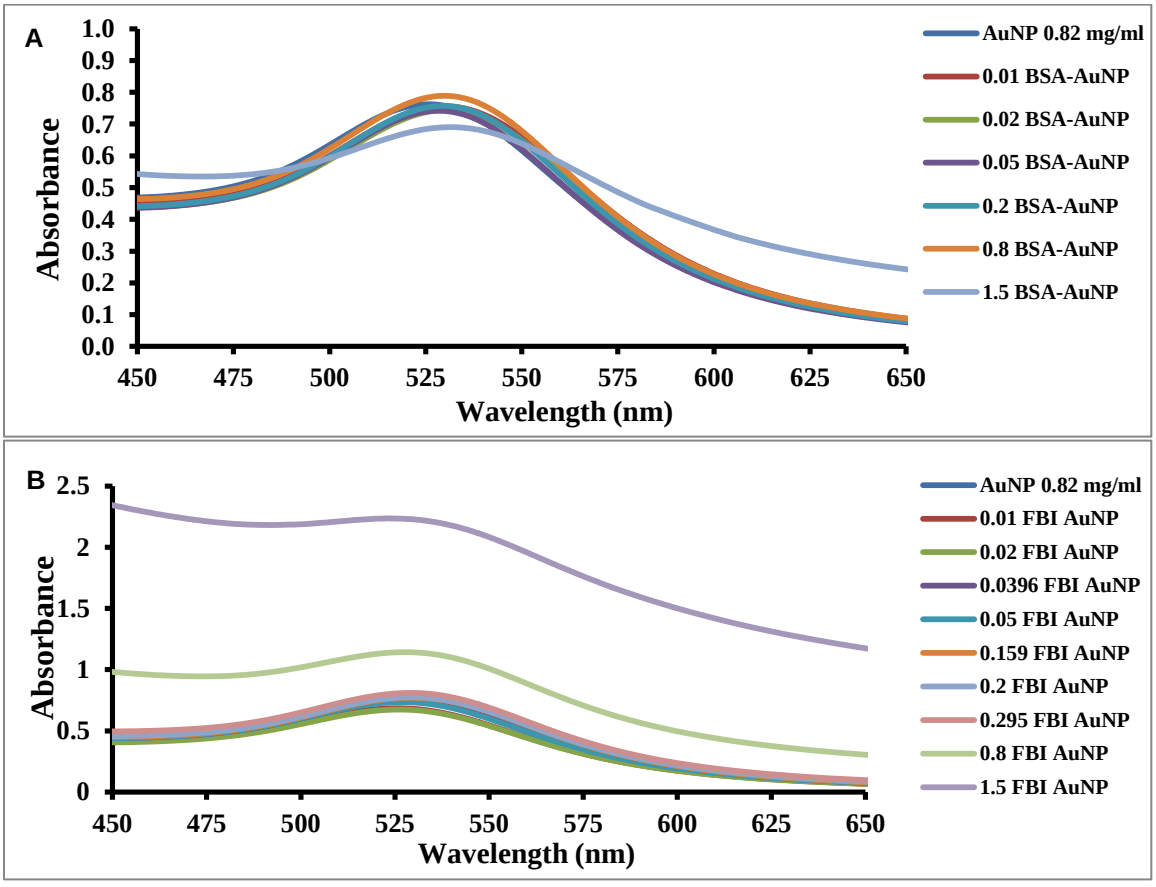

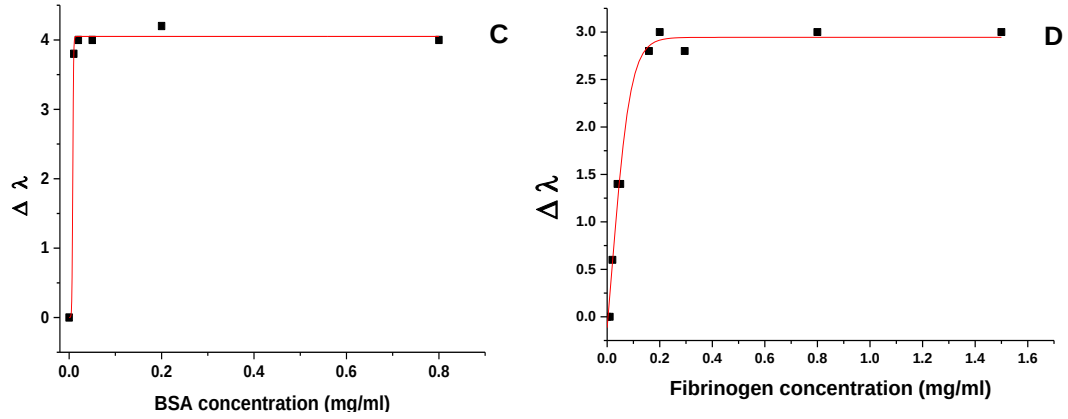

Figure 3. 12 UV-Vis Spectra of BSA interacts with positive coated AuNP **(A).** FBI interacts with positive coated AuNP **(B).** Red-shifts of UV-Vis absorbance peak wavelengths induced by the formation of BSA-AuNPs corona **(C)**, FBI-AuNP corona **(D)**, the horizontal axis shows the molar ratios of protein to AuNP.

1383

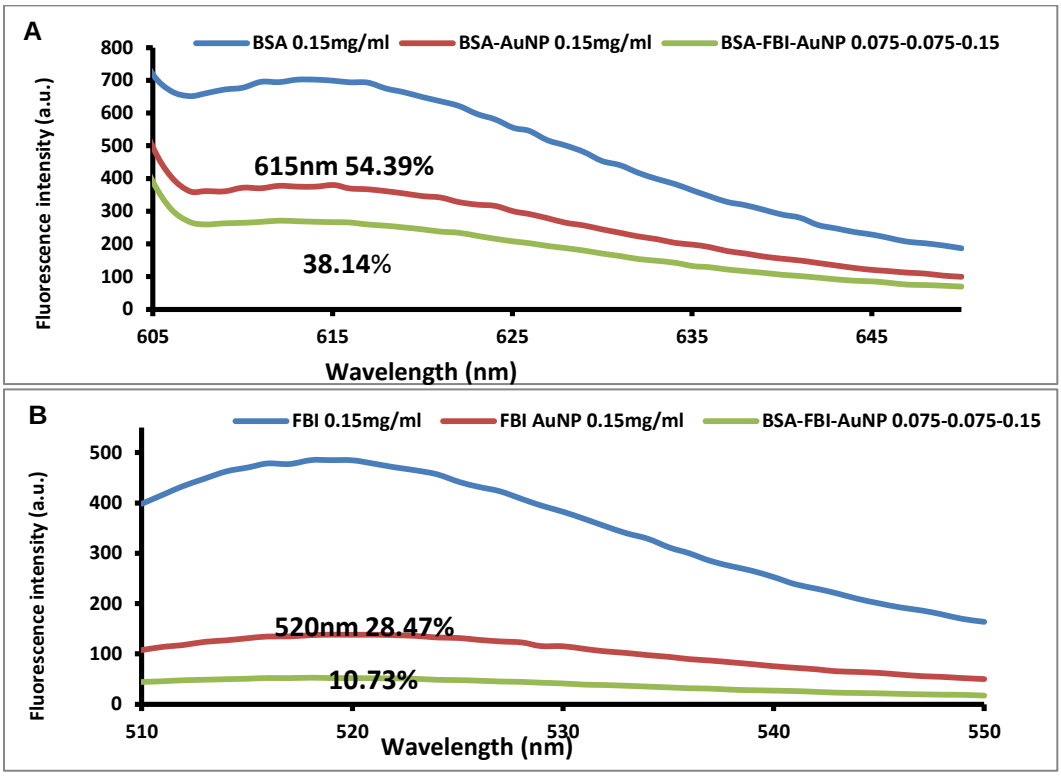

1384

1385

Figure 3. 13 (A). Fluorescence spectra of F-BSA, F-BSA and AuNP mixture, F-BSA and F-FBI mix with AuNP. (excited at 590 nm). **(B).** Fluorescence spectra of F-FBI, F-FBI- and AuNP mixture, F-FBI and F-BSAmix with AuNP. (excited at 490 nm).

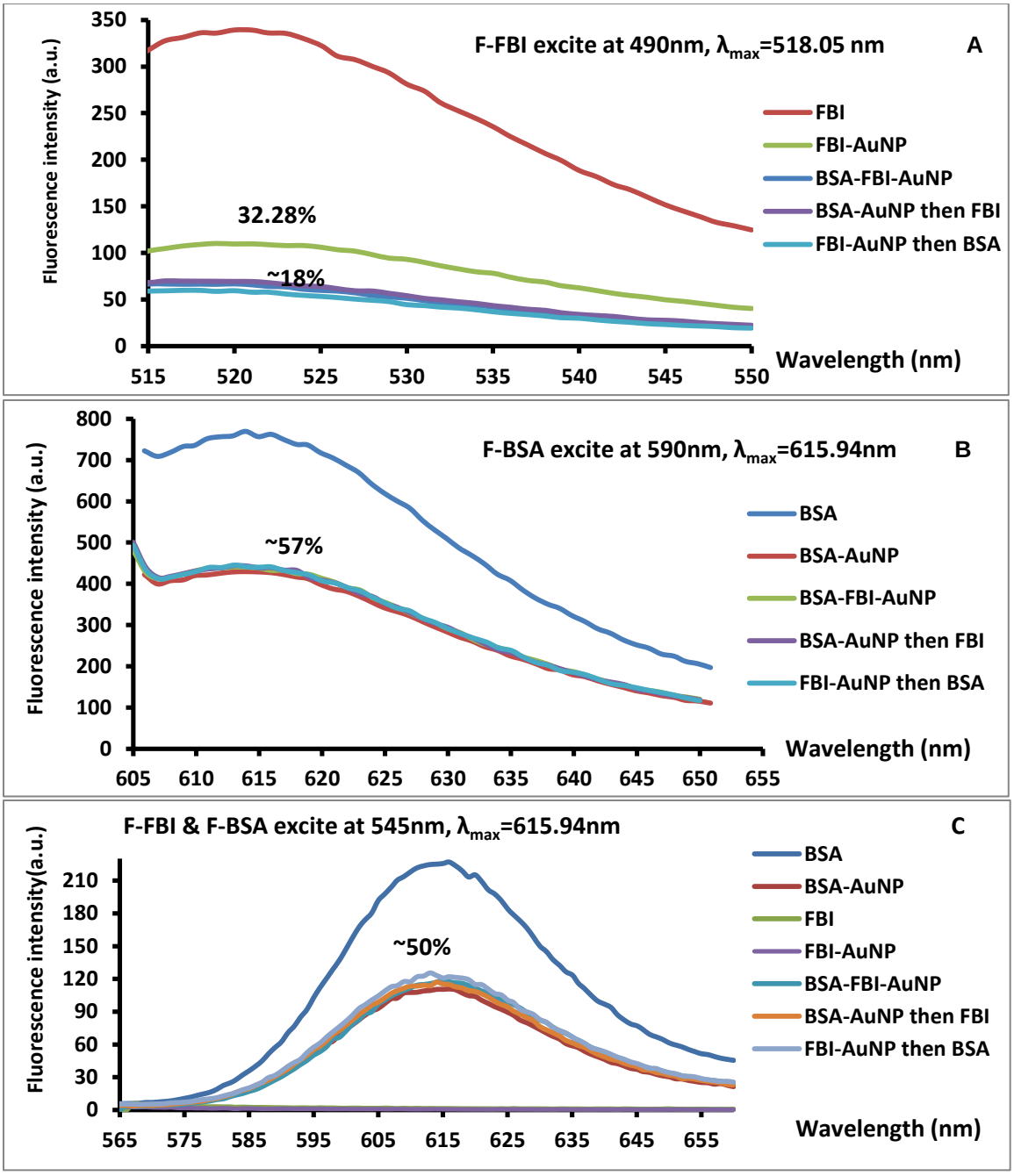

Figure 3. 14 (A) Fluorescence spectra of F-FBI; F-FBI add AuNP; F-BSA and F-FBI mixture then add AuNP; F-BSA and AuNP mixture then add F-FBI; F-FBI and AuNP mixture then add F-BSA excited at 490 nm. **(B)** Fluorescence spectra of F-BSA;F-BSA add AuNP; F-BSA and F-FBI mixture then add AuNP; F-BSA and AuNP mixture then add F-FBI; F-FBI and AuNP mixture then add F-BSA excited at 590 nm. **(C)** Fluorescence spectra of F-BSA; F-BSA add AuNP; F-FBI; F-FBI add AuNP; F-BSA and F-FBI mixture then add AuNP; F-BSA and AuNP mixture then add F-FBI; F-FBI and AuNP mixture then add F-BSA excited at 545 nm.

3.5 Conclusion

AgNP are considered for potential application in noninvasive cancer detection[62], AuNP have been reported to improve anticancer drug delivery[63] and can be used in the photodynamic therapy of breast cancer.[64] In order to understand the protein-NP interactions, AgNP and AuNP are taken as NP examples to study their interactions with different proteins. The results and discussion are showed above. UV-Vis spectroscopy, fluorescence spectroscopy, circular dichroism spectroscopy, dynamic light scattering, zeta potential measurements, transmission electron microscopy, CytoViva Hyperspectral Imaging and inductively-coupled plasma mass spectrometry have been used to compare the interactions between different NP and proteins.

In summary, actin and tubulin tend to self-polymerize and their interaction with AgNP will reduce the AgNP aggregation degree. Also, the formations of cytoskeletal protein-AgNP corona will inhibit cytoskeleton protein aggregation. The size differences between proteins and NP can have an impact on the formation of protein-NP corona as shown by the complement C3 protein interact with 20 nm and 110 nm AgNP. As the hydrodynamic size of complement C3 is very close to 20 nm, it is relatively easier to form protein-NP corona with 110 nm AgNP with fewer changes on the secondary structure of the protein. Simulation approach plays an important role in predicting protein-NP interaction. By modifying simulation parameters based on experimental results, reasonable predictions can be made on protein-NP corona behavior. Fluorescence

spectroscopy utilizing fluorophore modified proteins was used to determine protein-NP interactions beyond UV-Vis spectrometry. The fluorescence intensity changes in fluorophore labeled protein imply that there is a stronger interaction between BSA with AuNP than FBI with AuNP. The protein conformational changes and crowding resulting from their interactions with the nanoparticle were studied by TEM. The ions released from NP and the evolution of the protein corona over time was explored using ICP-MS.

The interaction between NP and protein can be attributed to hydrogen bonding, hydrophobic and electrostatic interactions, Van der Waals forces, solvation forces, etc. as summarized by several review articles and books. [16, 47, 60] There are a series of dynamic interactions between the interface of NP surface and proteins. All of these forces contribute to the absorption of protein onto NP. [65-67] The protein α-helices are stabilized by hydrogen bonds alone while β-sheets are stabilized by hydrogen bonds combined with hydrophobic interactions.[68] The circular dichroism data above for cytoskeleton proteins, complement component C3 and apolipoprotein all showed decrease of α-helices and increase of β-sheets when interact with NP, which indicates hydrogen bonds of the protein were broken and more hydrophobic interactions build up. Since the AgNP used in this study are modified by citrate acid, more hydrophilic motif of the proteins might like to present close to the surface of AgNP when interact with NP. The degree of protein structure disruption partially depends on the balance between the hydrogen bond breakage and formation. Due to the highly localized nature of hydrogen bonding (typically 2–3 angstroms in bond length), the larger sized protein (relative to the

NP) probably experienced higher degree of changes when binding to the AgNP. [47] As the complement component 3 size is very close to 20 nm, its interaction with 20 nm AgNP generated a higher degree of protein deformation compared to interaction with 110 nm AgNP. Indexes characterize the contribution of Coulomb force (charged particles), London dispersion (hydrophobic interactions), effective solute hydrogen-bond acidity/basicity (hydrogen bonding), molecular forces of lone-pair electrons, and effective solute dipolarity and polarizability have been suggested by Jim E. Riviere to count the contribution when study the NP-protein interactions. [69, 70] Our results supported the hydrogen bonding interactions between surface charged NP and proteins, but it is not possible to rule out the contribution from electrostatic interactions, Van der Waals interactions, solvation interactions, etc. [68]

3.6 Acknowledgments

The CD facilities used were supported by NIH Grants 5P20RR021949-04 and 8P20GM103444-04. I would like to take this opportunity to thank Professor Puchun Ke, for his guidance, encouragement, and mentoring during the course of this work. I am indebted to the Dr Ke's group, particularly Dr. Pengyu Chen, Dr. Ran Chen, Dr. Nick Geitner, for their suggestions and advice over the past years. The simulation work in apolipoprotein work was done by Rongzhong Li in Dr Samuel S. Cho's group as a collaboration work.

3.7 References

[1] N. Lewinski., V. Colvin., R. Drezek., Cytotoxicity of nanoparticles, Small, 4(2008) 26-49.

[2] M. Ferrari, Cancer nanotechnology: opportunities and challenges, Nature Reviews Cancer 5(2005) 161-71.

[3] E. Ruoslahti, S.N. Bhatia, M.J. Sailor, Targeting of drugs and nanoparticles to tumors, The Journal of Cell Biology, 188(2010) 759-68.

[4] H.-R. Paur, F.R. Cassee, J. Teeguarden, H. Fissan, S. Diabate, M. Aufderheide, et al., In-vitro cell exposure studies for the assessment of nanoparticle toxicity in the lung-A dialog between aerosol science and biology, J Aerosol Sci, 42(2011) 668-92.

[5] E. Bergamaschi, O. Bussolati, A. Magrini, M. Bottini, L. Migliore, S. Bellucci, et al., Nanomaterials and lung toxicity: interactions with airways cells and relevance for occupational health risk assessment, Int J Immunopathol Pharmacol, 19(2006) 3-10.

[6] I. Iavicoli., P.A. Schulte., S. Iavicoli., Nanomaterial Interactions with Biological Systems: Implications for Occupational Health, Journal of Nanomaterials, (2012) 2.

[7] J.Y. Ying, Nanostructures Materials, New York: Academic Press; 2001.

[8] M. Anisa, S.D. Abdallah, A.S. Peter, 'Mind the gap': science and ethics in nanotechnology, Nanotechnology, 14(2003) R9.

[9] S. Kittler, C. Greulich, J. Diendorf, M. Köller, M. Epple, Toxicity of Silver Nanoparticles Increases during Storage Because of Slow Dissolution under Release of Silver Ions, Chemistry of Materials, 22(2010) 4548-54.

[10] The Project on Emerging Nanotechnologies, Consumer Products Inventory, http://www.nanotechproject.org/cpi/products/ (accessed Dec/6/2017).

[11] H.J. Johnston, G. Hutchison, F.M. Christensen, S. Peters, S. Hankin, V. Stone, A review of the in vivo and in vitro toxicity of silver and gold particulates: Particle attributes and biological mechanisms responsible for the observed toxicity, Crit Rev Toxicol, 40(2010) 328-46.

[12] M. Ahamed, M.S. AlSalhi, M.K.J. Siddiqui, Silver nanoparticle applications and human health, Clin Chim Acta, 411(2010) 1841-8.

[13] E. Boisselier, D. Astruc, Gold nanoparticles in nanomedicine: preparations, imaging, diagnostics, therapies and toxicity, Chemical Society Reviews, 38(2009) 1759-82.

[14] E.E. Connor, J. Mwamuka, A. Gole, C.J. Murphy, M.D. Wyatt, Gold Nanoparticles Are Taken Up by Human Cells but Do Not Cause Acute Cytotoxicity, Small, 1(2005) 325-7.

[15] R. Shukla, V. Bansal, M. Chaudhary, A. Basu, R.R. Bhonde, M. Sastry, Biocompatibility of Gold Nanoparticles and Their Endocytotic Fate Inside the Cellular Compartment: A Microscopic Overview, Langmuir, 21(2005) 10644-54.

[16] A.M. Alkilany, C.J. Murphy, Toxicity and cellular uptake of gold nanoparticles: what we have learned so far?, J Nanopart Res, 12(2010) 2313-33.

[17] N. Pernodet, X. Fang, Y. Sun, A. Bakhtina, A. Ramakrishnan, J. Sokolov, et al., Adverse Effects of Citrate/Gold Nanoparticles on Human Dermal Fibroblasts, Small, 2(2006) 766-73.

[18] Y. Pan, S. Neuss, A. Leifert, M. Fischler, F. Wen, U. Simon, et al., Size-Dependent Cytotoxicity of Gold Nanoparticles, Small, 3(2007) 1941-9.

[19] C.M. Goodman, C.D. McCusker, T. Yilmaz, V.M. Rotello, Toxicity of Gold Nanoparticles Functionalized with Cationic and Anionic Side Chains, Bioconjugate Chemistry, 15(2004) 897-900.

[20] W. Cai, T. Gao, H. Hong, J. Sun, Applications of gold nanoparticles in cancer nanotechnology, Nanotechnology, science and applications, 2008(2008) 10.2147/NSA.S3788.

[21] T. Cedervall, I. Lynch, S. Lindman, T. Berggård, E. Thulin, H. Nilsson, et al., Understanding the nanoparticle–protein corona using methods to quantify exchange rates and affinities of proteins for nanoparticles, Proceedings of the National Academy of Sciences, 104(2007) 2050-5.

[22] L.M. Andre E. Nel, Darrell Velegol, Tian Xia, Eric M. V. Hoek, Ponisseril Somasundaran, Fred Klaessig, Vince Castranova,Mike Thompson, Understanding biophysicochemical interactions at the nano–bio interface, Nature Materials, 8(2009) 543-57.

[23] J.H. Sung, J.H. Ji, J.D. Park, M.Y. Song, K.S. Song, H.R. Ryu, et al., Subchronic inhalation toxicity of gold nanoparticles, Particle and Fibre Toxicology, 8(2011) 16.

[24] R. Kessler, Engineered Nanoparticles in Consumer Products: Understanding a New Ingredient, Environmental Health Perspectives, 119(2011) A120-A5.

[25] T.A. Ratnikova, P.N. Govindan, E. Salonen, P.C. Ke, In Vitro Polymerization of Microtubules with a Fullerene Derivative, ACS Nano, 5(2011) 6306-14.

[26] R. Martínez-Barricarte, M. Heurich, F. Valdes-Cañedo, E. Vazquez-Martul, E. Torreira, T. Montes, et al., Human C3 mutation reveals a mechanism of dense deposit disease pathogenesis and provides insights into complement activation and regulation, The Journal of Clinical Investigation, 120(2010) 3702-12.

[27] Complement Component 3, Wikipedia https://en.wikipedia.org/wiki/Complement_component_3 (accessed Dec/6/2017).

[28] P. Lachmann, Genetics of the complement system, J Med Genet, 12(1975) 372-7.

[29] D.T. Bradley, P.F. Zipfel, A.E. Hughes, Complement in age-related macular degeneration: a focus on function, Eye, 25(2011) 683-93.

[30] B.E. Cham, Importance of apolipoproteins in lipid metabolism, Chemico-Biological Interactions, 20(1978) 263-77.

[31] Apolipoprotein, Wikipedia, https://en.wikipedia.org/wiki/Apolipoprotein (accessed Dec/6/2017).

[32] K.R. Feingold., C. Grunfeld., Introduction to Lipids and Lipoproteins, In: De Groot LJ, Chrousos G, Dungan K, et al., editors. Endotext. South Dartmouth (MA): MDText.com, Inc.; 2000-2017.

[33] R. Li, R. Chen, P. Chen, Y. Wen, P.C. Ke, S.S. Cho, Computational and Experimental Characterizations of Silver Nanoparticle–Apolipoprotein Biocorona, The Journal of Physical Chemistry B, 117(2013) 13451-6.

[34] R.W. Mahley, T.L. Innerarity, S.C. Rall, K.H. Weisgraber, Plasma lipoproteins: apolipoprotein structure and function, Journal of Lipid Research, 25(1984) 1277-94.

[35] A. Farrugia, Albumin Usage in Clinical Medicine: Tradition or Therapeutic?, Transfusion Medicine Reviews, 24(2010) 53-63.

[36] I. Roberts, K. Blackhall, P. Alderson, F. Bunn, G. Schierhout, Human albumin solution for resuscitation and volume expansion in critically ill patients, Cochrane Database of Systematic Reviews, (2011).

[37] U. Kragh-Hansen, Clinical Use of Albumin, http://albumin.org/clinical-use-of-albumin/ (accessed Dec/6/2017).

[38] P. Lee, X. Wu, Review: Modifications of Human Serum Albumin and Their Binding Effect, Current pharmaceutical design, 21(2015) 1862-5.

[39] J.-L. Vincent, J.A. Russell, M. Jacob, G. Martin, B. Guidet, J. Wernerman, et al., Albumin administration in the acutely ill: what is new and where next?, Critical Care, 18(2014) 231.

[40] Fibrinogen, Wikipedia, https://en.wikipedia.org/wiki/Fibrinogen (accessed Dec/6/2017).

[41] O.V. Gorkun, Y.I. Veklich, J.W. Weisel, S.T. Lord, The Conversion of Fibrinogen to Fibrin: Recombinant Fibrinogen Typifies Plasma Fibrinogen, Blood, 89(1997) 4407.

[42] R.F. Doolittle, Fibrinogen and Fibrin, Annual Review of Biochemistry, 53(1984) 195-229.

[43] P. Petersen, Thromboembolic complications in atrial fibrillation, Stroke, 21(1990) 4.

[44] M. Hayakawa, Dynamics of fibrinogen in acute phases of trauma, Journal of Intensive Care, 5(2017) 3.

[45] D.B.P.a.E.J.S. Duncan, Surface Plasmon Resonance spectroscopy of Gold Nanoparticle-Coated Substrates Use as an Indicator of Exposure to Chemical Warfare Simulants, Defence R&D Canada (2005).

[46] M.R. Gittings, D.A. Saville, The determination of hydrodynamic size and zeta potential from electrophoretic mobility and light scattering measurements, Colloids and Surfaces A: Physicochemical and Engineering Aspects, 141(1998) 111-7.

[47] Y. Wen, N.K. Geitner, R. Chen, F. Ding, P. Chen, R.E. Andorfer, et al., Binding of cytoskeletal proteins with silver nanoparticles, RSC Advances, 3(2013) 22002-7.

[48] A.R. Badireddy, M.R. Wiesner, J. Liu, Detection, Characterization, and Abundance of Engineered Nanoparticles in Complex Waters by Hyperspectral Imagery with Enhanced Darkfield Microscopy, Environmental Science & Technology, 46(2012) 10081-8.

[49] M. Hu, C. Novo, A. Funston, H. Wang, H. Staleva, S. Zou, et al., Dark-field microscopy studies of single metal nanoparticles: understanding the factors that influence the linewidth of the localized surface plasmon resonance, J Mater Chem, 18(2008) 1949-60.

[50] K. Seekell, M.J. Crow, S. Marinakos, J. Ostrander, A. Chilkoti, A. Wax, Hyperspectral molecular imaging of multiple receptors using immunolabeled plasmonic nanoparticles, J Biomed Opt, 16(2011) 116003/1-/12.

[51] CytoViva, Enhanced Darkfield Illumination System, https://cytoviva.com/products/microscopy-2/high-resolution-illuminator/ (accessed Dec/6/2017).

[52] M. Mortimer, A. Gogos, N. Bartolomé, A. Kahru, T.D. Bucheli, V.I. Slaveykova, Potential of Hyperspectral Imaging Microscopy for Semi-quantitative Analysis of Nanoparticle Uptake by Protozoa, Environmental Science & Technology, 48(2014) 8760-7.

[53] D. Corrêa, C.H.I. Ramos, The use of circular dichroism spectroscopy to study protein folding, form and function, African Journal of Biochemistry Research, 3(2009).

[54] T.J.J. Sharon M Kelly, Nicholas C.Price, How to study proteins by circular dichroism, Biochim Biophys Acta, 1751(2005).

[55] N. Sreerama, R.W. Woody, Estimation of protein secondary structure from circular dichroism spectra: Comparison of CONTIN, SELCON, and CDSSTR methods with an expanded reference set, Anal Biochem, 287(2000) 252-60.

[56] N. Sreerama, R.W. Woody, Computation and analysis of protein circular dichroism spectra, Methods Enzymol, 383(2004) 318-51.

[57] K. Juganson, M. Mortimer, A. Ivask, K. Kasemets, A. Kahru, Extracellular conversion of silver ions into silver nanoparticles by protozoan Tetrahymena thermophila, Environmental Science: Processes & Impacts, 15(2013) 244-50.

[58] J.H. Shannahan, X. Lai, P.C. Ke, R. Podila, J.M. Brown, F.A. Witzmann, Silver Nanoparticle Protein Corona Composition in Cell Culture Media, PLOS ONE, 8(2013) e74001.

[59] N. Durán, C.P. Silveira, M. Durán, D.S.T. Martinez, Silver nanoparticle protein corona and toxicity: a mini-review, Journal of Nanobiotechnology, 13(2015) 55.

[60] R. Li., R. Chen., P. Chen., Y. Wen., P. Ke., S.S. Cho., Computational and Experimental Characterization of Silver Nanoparticle-Apolipoprotein Biocorona, Journal of Pyhsical Chemistry, (2013).

[61] B. Savage, E. Bottini, Z.M. Ruggeri, Interaction of Integrin αIIbβ3 with Multiple Fibrinogen Domains during Platelet Adhesion, Journal of Biological Chemistry, 270(1995) 28812-7.

[62] J. Lin, R. Chen, S. Feng, J. Pan, Y. Li, G. Chen, et al., A novel blood plasma analysis technique combining membrane electrophoresis with silver nanoparticle-based SERS spectroscopy for potential applications in noninvasive cancer detection, Nanomedicine : nanotechnology, biology, and medicine, 7(2011) 655-63.

[63] S.D. Brown, P. Nativo, J.A. Smith, D. Stirling, P.R. Edwards, B. Venugopal, et al., Gold nanoparticles for the improved anticancer drug delivery of the active component of oxaliplatin, J Am Chem Soc, 132(2010) 4678-84.

[64] T. Stuchinskaya, M. Moreno, M.J. Cook, D.R. Edwards, D.A. Russell, Targeted photodynamic therapy of breast cancer cells using antibody-phthalocyanine-gold nanoparticle conjugates, Photochem Photobiol Sci, 10(2011) 822-31.

[65] A.E. Nel, L. Mädler, D. Velegol, T. Xia, E.M.V. Hoek, P. Somasundaran, et al., Understanding biophysicochemical interactions at the nano–bio interface, Nature Materials, 8(2009) 543.

[66] S.R. Saptarshi, A. Duschl, A.L. Lopata, Interaction of nanoparticles with proteins: relation to bio-reactivity of the nanoparticle, Journal of Nanobiotechnology, 11(2013) 26-.

[67] M.A. Dobrovolskaia, S.E. McNeil, Immunological Properties of Engineered Nanomaterials: An Introduction, Handbook of Immunological Properties of Engineered Nanomaterials, WORLD SCIENTIFIC2012, pp. 1-23.

[68] A.A. Shemetov, I. Nabiev, A. Sukhanova, Molecular Interaction of Proteins and Peptides with Nanoparticles, ACS Nano, 6(2012) 4585-602.

[69] X.-R. Xia, N.A. Monteiro-Riviere, J.E. Riviere, An index for characterization of nanomaterials in biological systems, Nature Nanotechnology, 5(2010) 671.

[70] X.R. Xia, N.A. Monteiro-Riviere, S. Mathur, X. Song, L. Xiao, S.J. Oldenberg, et al., Mapping the Surface Adsorption Forces of Nanomaterials in Biological Systems, ACS Nano, 5(2011) 9074-81.

CHAPTER FOUR

Conclusion and Future Work

The aim of this dissertation is to study nanoscience and nanotechnology from their synthesis and application aspects, understanding their fate when interact with biological fluids. The concepts and ideas behind nanoscience and nanotechnology started with a talk by Dr. Richard Feynman in 1959, with the talk titled "There's Plenty of Room at the Bottom". The understanding and controlled manipulation of nanoscale structures will have a big influence on nanoscience and nanotechnology applications across chemistry, biology, physics, materials science, and engineering fields. [1] Hence, I studied the synthesis of carbon nanofibers, utilized AgNP for sensing purpose and explored the AgNP and AuNP interactions with proteins in biological fluids.

In summary, chapter 1 outlines the synthesis of CNF from CNC under hydrothermal conversion at 240 ℃ without catalysts. In recent years, the carbon nanofibers industry has been steadily growing to meet the rising market demands. The wide applications of carbon nanofibers in polymer additives, gas storage materials, catalyst supports, electronic hardware, etc. have attracted scientists' attention. [2] Compared to traditional vapor deposition/ vapor growth method, hydrothermal

conversion is environmentally friendly, does not require toxic chemicals and has commercial potential for inexpensive production of carbon nanofibers.[3] [4] Future study will include testing the mechanical property of our CNF and the scale up production of CNF from CNC.

Chapter 2 is a detailed study of using PMMA stabilized 2D AgNP array as a sensing scaffold. This novel method of stabilizing 2D AgNP was tested on our differential optical transmission instrument to detect the bulk refractive index changes in solution. PMMA stabilized 2D AgNP array gives linear response to bulk refractive index changes and can be re-used after simple cleaning with DI water. This is a proof of concept to use 2D AgNP array for sensing. Polymer 2DSNPF taking advantage of both the sharper LSPR peak and polymer shrinkage or swelling upon exposing to VOC vapors was designed to distinguish between different VOCs. By exploring the differential optical transmission method developed in our lab, polymer 2DSNPF LSPR peak changes upon exposing to VOC vapors can be monitored by both diffusion time and PMT differential signal intensity. Compared to traditional UV-Vis spectroscopy, real time sensing and better signal to noise ratio can be achieved. Different responsive polymer (co-polymer, block polymer, polymer mixture, etc.) can be used to give distinguishable signals.

The PMMA stabilized 2D AgNP array system can be further used for quantifying VOC concentration if adding a sealed system to monitor the vapor concentration. Future studies will continue to optimize the application of PMMA stabilized 2D AgNP array for

sensing. The surface of PMMA stabilized 2D AgNP array can be modified with streptavidin, allowing us utilizes the biotinylated protein-streptavidin interactions. This will allow us to detect the biotinylated protein concentration based on the protein binding induced LSPR peak shift.

The use of nanomaterials in biomedical and biotechnological applications is growing. Some nanomaterials have been released into the environment as consumer products. [5] Owing to their high surface free energy, biomolecules in biological fluids absorb on nanomaterials when in contact with nanomaterials. In particular, proteins bind to the surface of nanoparticles to form a biological coating around the nanoparticles, known as the NP-protein corona. The NP-protein corona affects the biological identity of the nanoparticles, therefore it is essential to understand the formation and kinetic evolution of the NP-protein corona. In Chapter 3, the fate of NP in biological fluids was studied by exploring several kinds of proteins' interaction with AgNP and AuNP. Cytoskeletal protein, immune protein, lipid protein, and plasma protein were involved. The idea of comparison between proteins binding with NP is to illustrate the roles of protein corona on biological responses to engineered nanomaterials for safe nanotechnology and nanomedicine. [6, 7] In summary, actin and tubulin tend to self-polymerize and their interaction with AgNP will reduce the nanoparticle aggregation degree. The formations of AgNP-cytoskeletal protein corona inhibit cytoskeleton protein self-polymerization. Overall, actin displayed a higher propensity than tubulin for AgNP while both proteins experienced conformational changes upon the binding, likely

originated from their smaller size and less rigidity. The formation of AgNP-protein corona will slow down Ag^+ ion release as examined by ICP-MS. The size differences between protein and NP can have an impact on the formation of NP-protein corona. As the hydrodynamic size of complement C3 is very close to 20 nm, it is relatively easier to form NP-protein corona with 110 nm AgNP with fewer changes on the secondary structure of the protein. Fluorescence spectroscopy utilizing fluorophore labeled proteins was used to determine NP protein interactions beyond UV-Vis spectrometry. The fluorescence intensity changes in fluorophore labeled protein imply that there is a stronger interaction between BSA with AuNP than FBI with AuNP. The knowledge derived from this study may facilitate our understanding of the dynamics, transformation, and distribution of nanomaterials in mammalian and plant cells, and may have relevance to the field studies of NP-biomolecular interactions, toxicology, biosensing, and medicine involving metallic NP.

The research presented here has established the basic knowledge necessary to continue the work on synthesizing nanomaterials and exploring new applications for nanomaterials. Groundwork has been laid to apply the PMMA stabilized 2D AgNP array for sensing using the differential optical transmission method developed in our lab. As discussed above, nanotechnology will have a dramatic effect on future advances in sensing, materials science, as well as medicine applications. Besides the work mentioned above, I had also collaborated with other groups on atomic force microscopy imaging[8,

9], Raman Spectroscopy[10], single crystal Raman spectroscopy [11-13] that turned into several publications and some are still in preparation.

Acknowledgments

I would like to acknowledge Dr. Colin McMillen for his assistance in work with the single crystal Raman studies along with the Kolis group for preparation of the samples and resolve XRD pattern. Dr. Marcus for giving suggestions on edits my dissertation.

References

[1] National Nanotechnology Initiative, What is Nanotechnology? , https://www.nano.gov/nanotech-101/what/definition (accessed Dec/6/2017).

[2] E. Hammel, X. Tang, M. Trampert, T. Schmitt, K. Mauthner, A. Eder, et al., Carbon nanofibers for composite applications, Carbon, 42(2004) 1153-8.

[3] B. Hu, S.-H. Yu, K. Wang, L. Liu, X.-W. Xu, Functional carbonaceous materials from hydrothermal carbonization of biomass: an effective chemical process, Dalton Transactions, (2008) 5414-23.

[4] Y. Wen, M. Jiang, C.L. Kitchens, G. Chumanov, Synthesis of carbon nanofibers via hydrothermal conversion of cellulose nanocrystals, Cellulose, (2017).

[5] M.E. Vance, T. Kuiken, E.P. Vejerano, S.P. McGinnis, M.F. Hochella, Jr., D. Rejeski, et al., Nanotechnology in the real world: Redeveloping the nanomaterial consumer products inventory, Beilstein Journal of Nanotechnology, 6(2015) 1769-80.

[6] Y. Wen, N.K. Geitner, R. Chen, F. Ding, P. Chen, R.E. Andorfer, et al., Binding of cytoskeletal proteins with silver nanoparticles, RSC Advances, 3(2013) 22002-7.

[7] R. Li., R. Chen., P. Chen., Y. Wen., P. Ke., S.S. Cho., Computational and Experimental Characterization of Silver Nanoparticle-Apolipoprotein Biocorona, Journal of Pyhsical Chemistry, (2013).

[8] X. Yang, Y. Wen, G. Chumanov, R.C. Smith, A new route to phosphonium polymer network solids via cyclotrimerization, Journal of Polymer Science Part A: Polymer Chemistry, 55(2017) 1620-5.

[9] F.S. Ameer, S. Varahagiri, D.W. Benza, D.R. Willett, Y. Wen, F. Wang, et al., Tuning Localized Surface Plasmon Resonance Wavelengths of Silver Nanoparticles by Mechanical Deformation, The Journal of Physical Chemistry C, 120(2016) 20886-95.

[10] M.B. Savchak, Nikolay; Burtovyy, Ruslan; Anayee, Mark ; Hu, Kesong ; Ma, Ruilong; Grant, Anise; Li, Hongmei ; Cutshall, Daniel; Wen, Yi-Mei; Koley, Goutam; Harrell, William; Chumanov, George; Tsukruk, Vladimir; Luzinov, Igor, Highly conductive and transparent reduced graphene oxide nanoscale films via thermal conversion of polymer-encapsulated graphene oxide sheets, ACS Applied Materials & Interfaces, (2017).

[11] T.M. Smith Pellizzeri, C.D. McMillen, Y. Wen, G. Chumanov, J.W. Kolis, Three Unique Barium Manganese Vanadates from High-Temperature Hydrothermal Brines, Inorganic Chemistry, (2017).

[12] K. Fulle, L.D. Sanjeewa, C.D. McMillen, Y. Wen, A.C. Rajamanthrilage, J.N. Anker, et al., One-Pot Hydrothermal Synthesis of TbIII13(GeO4)6O7(OH) and K2TbIVGe2O7: Preparation of a Stable Terbium(4+) Complex, Inorganic Chemistry, (2017).

[13] T.M. Smith Pellizzeri, C.D. McMillen, S. Pellizzeri, Y. Wen, R.B. Getman, G. Chumanov, et al., Strontium manganese vanadates from hydrothermal brines: Synthesis and structure of Sr2Mn2(V3O10)(VO4), Sr3Mn(V2O7)2, and Sr2Mn(VO4)2(OH), Journal of Solid State Chemistry, 255(2017) 225-33.